Ph.D. DISSERTATION

Applicability of No-insulation High-temperature Superconductor Field Winding to Superconducting Synchronous Motor

무절연 고온초전도 계자 권선의
초전도 동기 모터 적용성 연구

BY

UIJONG BONG

AUGUST 2022

DEPARTMENT OF ELECTRICAL AND COMPUTER ENGINEERING
COLLEGE OF ENGINEERING
SEOUL NATIONAL UNIVERSITY

Ph.D. DISSERTATION

Applicability of No-insulation High-temperature Superconductor Field Winding to Superconducting Synchronous Motor

무절연 고온초전도 계자 권선의
초전도 동기 모터 적용성 연구

BY

UIJONG BONG

AUGUST 2022

DEPARTMENT OF ELECTRICAL AND COMPUTER ENGINEERING
COLLEGE OF ENGINEERING
SEOUL NATIONAL UNIVERSITY

Applicability of No-insulation High-temperature Superconductor Field Winding to Superconducting Synchronous Motor

무절연 고온초전도 계자 권선의
초전도 동기 모터 적용성 연구

지도교수 한 승 용
이 논문을 공학박사 학위논문으로 제출함

2022년 8월

서울대학교 대학원

전기 정보 공학부

봉 의 종

봉의종의 공학박사 학위 논문을 인준함

2022년 8월

위 원 장: _____ (인)
부위원장: _____ (인)
위 원: _____ (인)
위 원: _____ (인)
위 원: _____ (인)

Abstract

As global warming becomes a significant issue in recent years, major countries around the world are actively developing technical solutions to reduce greenhouse gas emissions in all areas of society to achieve carbon neutrality. Major fields requiring greenhouse gas reduction can be broadly classified into power systems, buildings, transportation, and industry. In particular, in the transportation field, which includes the operation of large cargo trucks, ships, and aircraft, the development of a new high-performance propulsion system based on alternative fuels like hydrogen or electricity is necessary to replace the conventional fossil fuel-based propulsion system. One of the important aspects in the development of an alternative fuel-based propulsion system is the improvement of the power density and energy density to achieve lightweight and small sizes. An electric propulsion system adopting a superconducting motor is expected to achieve high power density based on the high current density of a superconductor coil compared to a non-superconducting counterpart. Hence, for the development of eco-friendly propulsion systems in the next generation, various superconducting propulsion system development projects have been launched and conducted.

The operation reliability and protection problem of high-temperature superconductor (HTS) winding have been one of the key challenges for conventional HTS motors. A new concept of a no-insulation (NI) HTS motor adopting an NI HTS coil as a field winding was proposed to improve the operation reliability and protection of the HTS motor. NI HTS winding technology, which intentionally removes insulation between turns of the HTS coil, has been used to construct ultra-high field superconductor magnets, and its improved protection performance has been experimentally verified several times. However, in the case of a field winding in a superconducting motor, NI HTS field winding might affect the operating characteristics of the motor and could operate differently from those of the conventional insulated field winding, due to the leak-

age current between turns. Due to the unknown operation characteristics that might be derived from unique NI behaviors, it is necessary to discuss whether NI HTS field winding can be a potential option applicable to actual motors. Therefore, derivation of the analysis model and experimental verification are necessary to understand the operating characteristics of an NI HTS motor.

In this study, the applicability of NI HTS field winding to superconducting motors was discussed. First, based on the previously presented analysis techniques for insulated HTS coils and NI HTS coils, the first analysis model of a NI HTS motor considering NI characteristics was presented, and an analysis of operation characteristics was performed based on the suggested model. In addition, for the experimental investigations, the design and construction of a test machine with NI HTS field winding and an experiment system were conducted. The liquid nitrogen-based cooling system and dynamo test facility were constructed and major electrical, structural, and thermal characteristics that should be considered in the design were analyzed and applied to the system. The test motor with NI HTS field winding was operated under various conditions, and the nonlinear responses of NI HTS field winding were observed for the first time. The mechanism of the observed nonlinear responses of the NI HTS field winding was analyzed through the proposed analysis model considering the conditions of the test system, and how these responses of the NI HTS field winding could affect the operating characteristics of the motor was discussed. Finally, additional required studies and improvements for applying NI HTS field winding to actual motors were discussed.

Keywords: Superconductor Motor, High-temperature Superconductor, No-insulation, Electric Propulsion, Operation Characteristics

Student Number: 2017-27856

Contents

List of Tables

List of Figures

Nomenclature

Superconductor Properties

T_c	Critical temperature [K]
B_c	Critical magnetic field [T]
J_c	Critical current density [A/mm^2]
B_{c1}, B_{c2}	Lower and upper critical field in type-2 superconductor [T]
I_c	Critical current [A]
R_{sc}	Resistance of superconductor [$\mu\Omega$]
ρ_{sc}	Resistivity of superconductor [$\mu\Omega$·m]
E_c	Critical electric field [μV/cm]
n	Index value

Superconductor Coil Parameters

t_{cd}, w_{cd}	Thickness and width of REBCO coated conductor [mm]
r_i, r_o	Inner and outer radius of circular section in racetrack coil [mm]
l	Length of straight section in racetrack coil [mm]
N_t, N_s	Number of turns and number of stacks
I_{op}	Operating current [A]
T_{op}	Operating temperature [K]
L	Inductance [mH]
K	Field constant [mT/A]
R_{ct}	Contact resistivity [$\mu\Omega$·cm^2]
R_c	Characteristic resistance [$\mu\Omega$]

τ Time constant [sec]

E_m Magnetic stored energy [J]

I_θ Current flowing along winding path [A]

I_r Current flowing through turn-to-turn contact path [A]

V_f Terminal voltage of the coil [μV]

V_{coil} Voltage of the coil in finite element method [V]

I_{coil} Current of the coil in finite element method [A]

R_{coil} Resistance of the coil in finite element method [Ω]

J_{coil} Current density of the coil in finite element method [A/mm^2]

P_{AC} AC loss of superconductor coil [mW]

r_b Bending radius [mm]

d_n Distance of the REBCO layer from neutral bending axis [mm]

$\Delta e, \Delta T, \Delta I$ Energy margin [J/cm^3], temperature margin [K], and current margin [A]

V_m Volume of coil [cm^3]

t_{ah} Time taken to rise from the initial temperature to the final temperature [sec]

Machine Parameters

I_a Armature coil current [A]

I_f Field coil current [A]

d_{air} Airgap [mm]

d_c Distance from center [mm]

ω_r Rotating speed [rpm]

T_e Torque [Nm]

A_l Linear current density of armature coil [A/mm]

B_a Airgap magnetic field [T]

r_a Radius of airgap region from center [mm]

l_{REBCO} Total REBCO coated conductor consumption [m]

I_{da}, I_{qa} Armature coil current in d-axis and q-axis [A]

V_{da}, V_{qa} Armature coil voltage in d-axis and q-axis [V]

$\lambda_{da}, \lambda_{qa}$ Flux linkage of armature coil in d-axis and q-axis [Wb]

I_{dk}, I_{qk} Damper coil current in d-axis and q-axis [A]

V_{dk}, V_{qk} Damper coil voltage in d-axis and q-axis [V]

$I_{f\theta}, I_{fr}$ Current through winding path and leak current of field coil [A]

V_f Field coil voltage [μV]

R_a Armature coil resistance [mΩ]

R_{dk}, R_{qk} Damper coil resistance in d-axis and q-axis [mΩ]

$R_{f\theta}, R_{fr}$ Field coil resistance and contact resistance [$\mu\Omega$]

L_{md}, L_{mq} Mutual inductance of d-axis and q-axis [mH]

L_{la} Leakage inductance of armature coil [mH]

L_{ldk}, L_{lqk} Leakage inductance of damper coil in d-axis and q-axis [mH]

L_{lf} Leakage inductance of field coil [mH]

λ_f Flux linkage of field coil [Wb]

M_{fd} Mutual inductance between field coil and armature coil [mH]

J_r Rotating inertia [kg·m^2]

B Friction coefficient [Nm/(rad/s)]

T_L Mechanical load [Nm]

p Number of poles

h_1 Additional length for cryogenic chamber [cm]

h_{LN_2} Surface height of LN_2 in cryogenic chamber [cm]

F_c Centrifugal force [N]

Material Properties

μ Magnetic permeability [H/m]

σ_e Electric conductivity [S/m]

ρ_e Electric resistivity [Ω·m]

ρ_m Mass density [kg/m^3]

E Young's modulus [GPa]

ν Poisson's ratio

G Shear modulus [GPa]

E_Y Yield strength [MPa]

α_L Linear thermal expansion [%]

k Thermal conductivity [W/(m·K)]

C_p Heat capacity [J/(cm^{3}K)]

g Gravity acceleration constant [m/s^2]

Physical Variables

$\boldsymbol{H}$ Magnetic field strength [A/m]

$\boldsymbol{B}$ Magnetic flux density [T]

$\boldsymbol{E}$ Electric field strength [V/m]

$\boldsymbol{D}$ Electric flux density [V·m]

$\boldsymbol{J}$ Current density [A/m^2]

ρ_c Electric charge density [C/m^3]

θ_f Angle of magnetic field [rad]

u Displacement [mm]

σ_r, σ_h Radial and hoop stress [MPa]

σ_{mises} von Mises stress [MPa]

T Temperature [K]

$\varepsilon_c, \varepsilon_t$ Bending strain [%]

Other Symbols

$k_0, k_1, \alpha_0, \alpha_1, \beta_0, \beta_1, \varphi_1, c_1$ Critical current fitting parameters

L_t Thickness of thermal conduction layer [mm]

A_c Area for thermal conduction [mm^2]

$l_1, l_2, ..., l_m$ Materials lengths for effective property calculation [mm]

$A_1, A_2, ..., A_m$ Materials areas for effective property calculation [mm^2]

Abbreviations

LTS Low-temperature superconductor

HTS High-temperature superconductor

NI No insulation

INS Insulated

WFSM Wound field synchronous motor

LN2 Liquid nitrogen

LH2 Liquid hydrogen

LHe Liquid helium

DC Direct current

AC Alternative current

FEM Finite element method

EMF Electromotive force

THD Total harmonic distortion

RMS Root mean square

FFT Fast Fourier transform

Chapter 1

INTRODUCTION

1.1 Superconducting Electric Propulsion System for Next-generation Mobility

1.1.1 Requirements of Alternative-fueled Transportation for Net-zero 2050

As climate crisis due to global warming becomes a confronting threat to human life, international movements to find technical solutions to climate change are in progress. Major countries in the world declare *"Net-zero 2050,"* and they are trying to find proper approaches that fit the situations of their own country. The International Energy Agency (IEA) summarized and announced required greenhouse gas emission reductions in each social sector to achieve *Net-zero 2050* by assembling each country's policies and technology development goals [1]. As shown in figure 1.1 (a), these sectors can be divided into transport, industry, buildings, electricity, and others. In order to achieve *Net-zero 2050* in each sector, all possible technical solutions are being discussed.

Currently, the transport sector accounts for 23% of carbon emissions (figure 1.1 (a)), hence, is one of the major areas in need of carbon reduction. Most of these carbon emissions have resulted from the use of fossil fuels in engine-based propulsion sys-

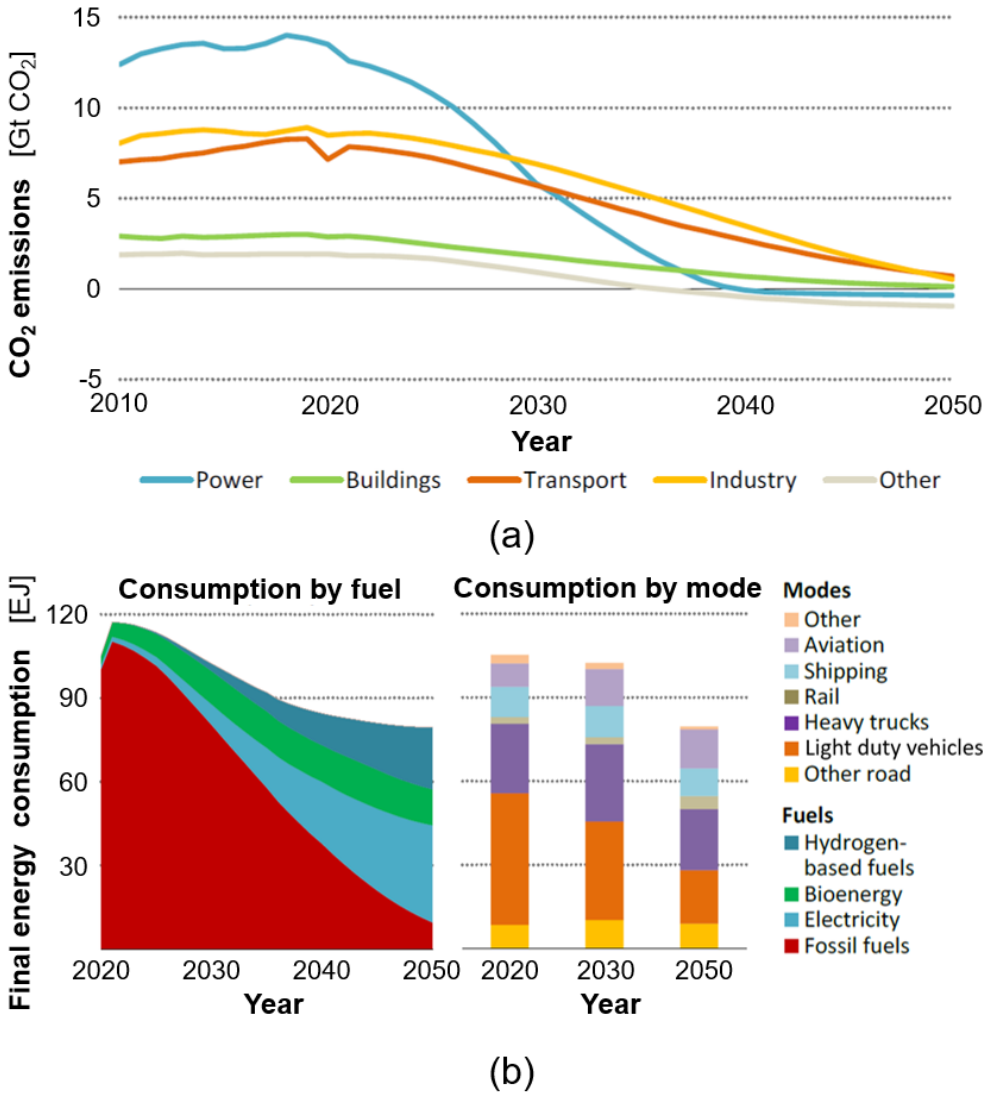

Figure 1.1: Net-zero 2050 scenario suggested by International Energy Agency [1]. (a) Carbon emission trends in each sector of society and future carbon emission aims, (b) Changes in fuel in the transport sector and energy consumption by each application.

tems as shown in figure 1.1 (b). In order to reduce carbon emissions in the conventional engine-based propulsion system, there have been various efforts to improve efficiency or reduce gas emissions, but those are not enough to overcome the current situation. A fundamental solution is to introduce a new propulsion system that can be operated based on an alternative fuel, especially for long-distance transport (heavy-duty trucking, maritime shipping, aviation, etc.), which account for a major portion of emission in the transport sector. The type of alternative fuels being considered is different depending on the applications, but include electricity, bio-fuel, and hydrogen-based fuel. Figure 1.1 (b) shows that these alternative fuel consumption should replace more than 2/3 of the current fossil fuel consumption to achieve *Net-zero 2050*.

However, the adoption of the alternative fuel system is particularly difficult in the transport sector because of the high energy density and power density requirements of each component (e.g., battery packs, motor, generator, and power conversion system) to secure their performance compared to a conventional system and to perform long-distance transport with limited energy storage. Therefore, to accomplish the alternative fuel-based transports, improvement of energy density and power density becomes an important issue. A high power density motor is considered one of the key components of an alternative fuel-based propulsion system. Especially, in the aviation field, since such power density is closely related to their operation time and the maximum travel distance, a high power density motor is being discussed as an enabler technology.

The importance of the motor's power density and its target value vary depending on the application. Figure 1.2 shows power density of various propulsion motors including electric aircraft, ship propulsion, electric car, and train traction. For ship propulsion motors, the rotating speed is within 300 rpm, and the power density is less than 1 kW/kg. Train traction motor has relatively low power density ($<$1 kW/kg) and it mainly comes from the armature cooling method, which is mainly designed as air-cooling. For electric car motors, the power density is up to $<$6 kW/kg. However, in the aviation field, where R&D is currently the most active, the ultimate goal for the most

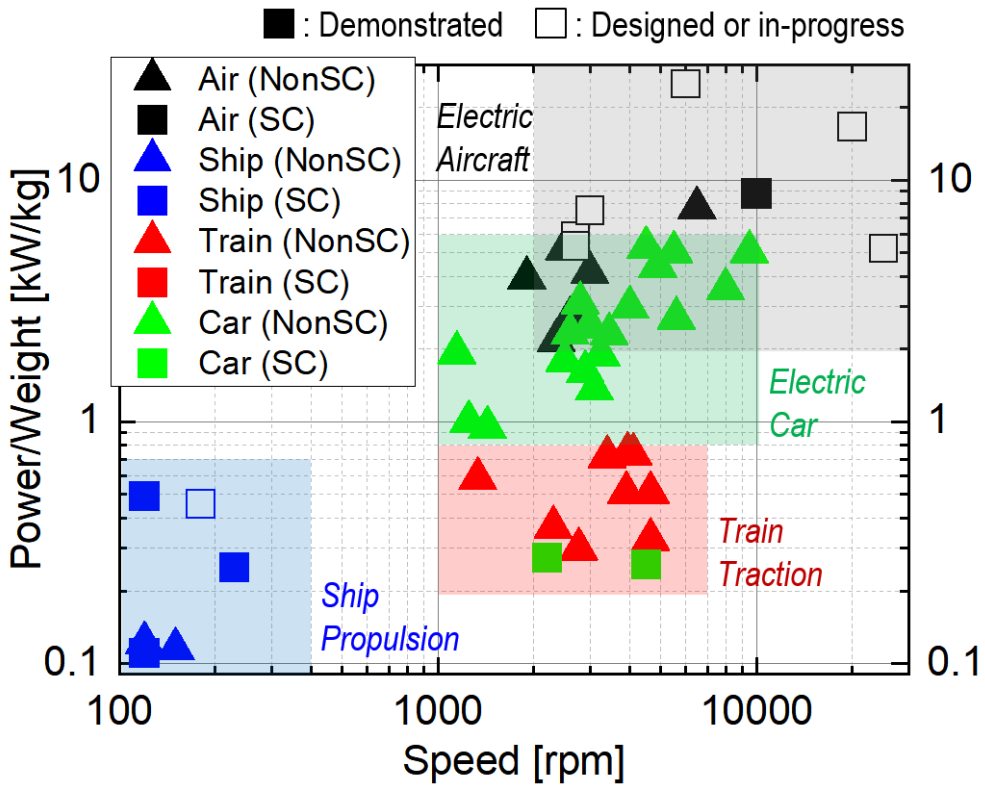

Figure 1.2: Scatter plot of design and development cases of propulsion motors including electric aircraft, ship propulsion, electric car, and train traction [2].

on-going projects is a power density of >10 kW/kg or even higher than 20 kW/kg. Considering that the rated power density of the motor used in the existing electric vehicle and aircraft is ranged in 3–6 kW/kg, this target is challenging. Especially, in the case of the conventional motors, it is difficult to expect significant improvement in power density due to the limitation of the permanent magnet's residual magnetic flux density and the current density of the copper-based winding. This challenging high power density requirement becomes the most important motivation for developing a superconducting motor.

1.1.2 Basic Concept and General Properties of Superconducting Motor

Definition and General Configurations of Superconducting Motor

Definition of the superconducting motor is an "electric motor that relies on the use of one or more superconducting elements in place of permanent magnets or copper winding [3]." In order to maximize the advantages of superconducting motors, various topologies of superconducting motors have been proposed and studied (figure 1.3 [4–7]), but the most common topology applied to actual construction is "synchronous motor with superconductor field coil" so far (figure 1.4). Since the superconductor coil is applied only to the field coil, it is also called a partial superconducting motor.

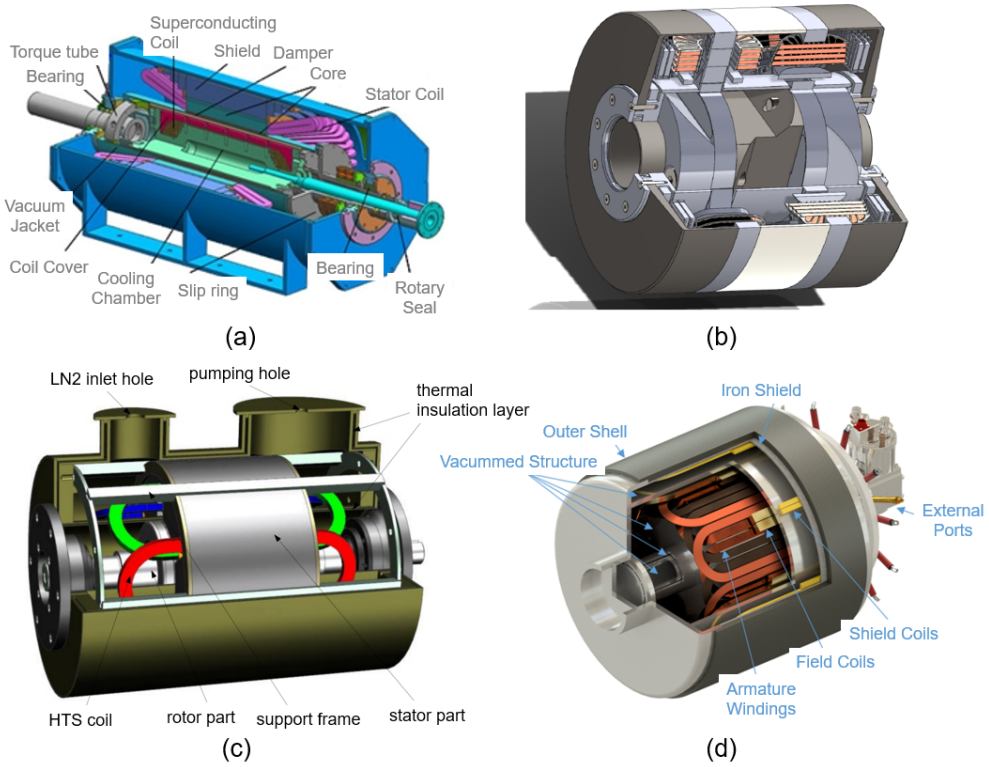

Figure 1.3: Various topologies of superconducting motor [4–7]. (a) Synchronous motor, (b) Homopolar motor, (c) Induction motor, and (d) Fully superconducting motor.

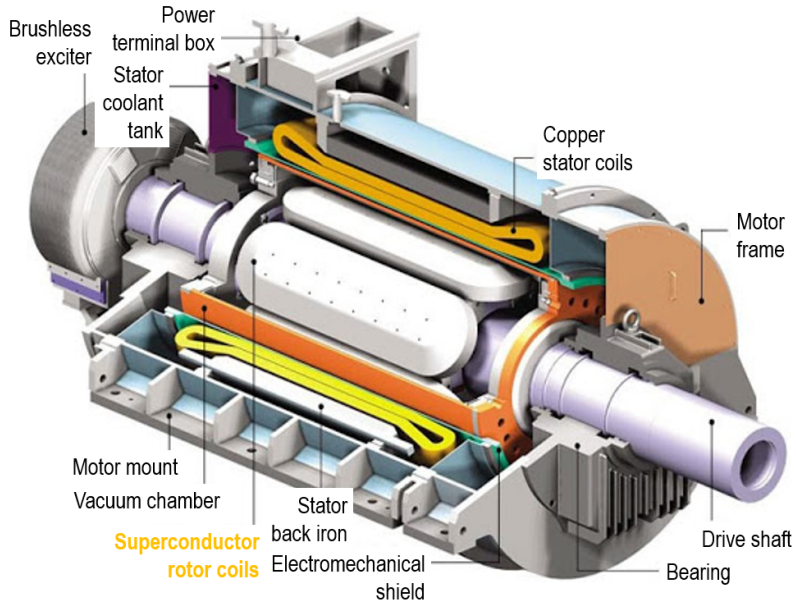

Figure 1.4: Configuration of partial superconducting motor [4].

Figure 1.4 shows a typical configuration of synchronous motor with superconductor field coil. The overall configuration is basically the same as the conventional wound field synchronous motor (WFSM) [8, 9], but the copper field coil is replaced by a superconductor coil, and an additional cryogenic system is added to maintain cryogenic temperature for superconducting elements. As a result of such cryogenic cooling, the superconducting motor is much more complex than conventional motors. Recently, with improved cryocooler technologies and the use of liquid hydrogen as a cryogen, fully superconducting motors, which adopt superconductor coils at both field coil and armature coil, are being studied to achieve even higher power density [7, 10, 11]. However, actual demonstration cases are rare so far.

Pros and Cons of Superconducting Motor

Superconducting motors are generally considered to have the following advantages and disadvantages compared to conventional motors.

- **Pros 1 - Current density & magnetic field increment:** when a superconductor wire is adopted, a much larger current density can flow (>100 A/mm^2) than copper wire (3–20 A/mm^2). Based on the high current density, it is possible to create a higher air-gap magnetic field strength than copper winding or permanent magnets. Due to the higher magnetic field, iron-core is easily saturated, so an air-cored configuration is often adopted in the design [4].

- **Pros 2 - Higher torque density & power density:** by increasing the air gap magnetic field, the same output can be produced in a smaller size and lighter weight. In addition, if the air-core topology is applied, the weight of the motor can be further reduced (figure 1.5 [12, 13]).

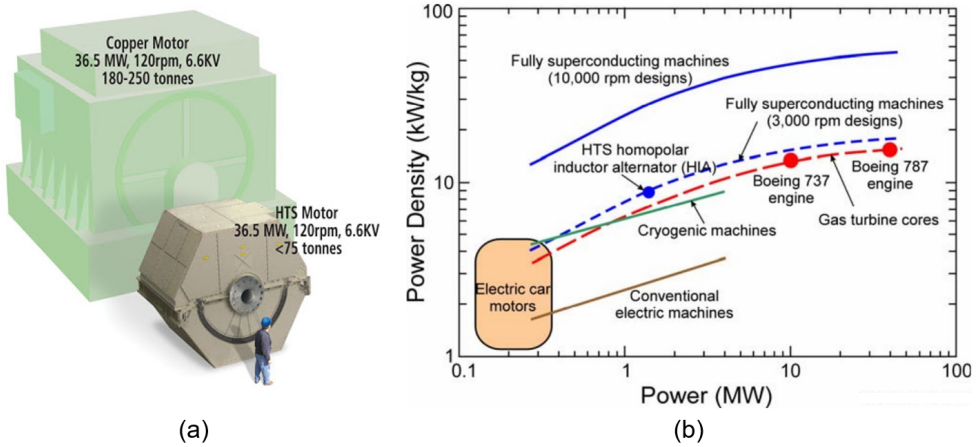

Figure 1.5: Examples showing advantages of superconducting motors [12, 13]. (a) Size and weight comparison, (b) Power density comparison between propulsion systems.

- **Cons 1 - Cryogenic cooling system:** in order to maintain the superconducting state, the superconductor coil must maintain a cryogenic temperature (typically, 4.2–77 K). For that, a sophisticated cryogenic cooling system (e.g., cryogen circulation structure with pump, cryogen coupling, cooling chamber, and heat

conduction channel) is required in addition to the conventional motor cooling system, increasing the complexity of the motor.

- **Cons 2 - Excitation system for high current field coil:** a current supply and brush structure are additionally required to excite a superconductor field coil operated in high current, which is not required for permanent magnet-based motors. To solve this problem, research on a superconducting motor based on the concept of a "flux pump" is also in progress by various institutes [14–16], which operates after excitation of the superconductor coil in a non-contact manner.

- **Cons 3 - Difficult demonstration in a small scale:** due to the reasons of *Cons 1* and *Cons 2* above, a large enough system that can offset these shortcomings is required for high torque & power density in an actual demonstration, or a special concept specialized for superconducting motors is required (e.g., simplification of the cooling system through connection with liquid hydrogen fuel cell power generation system).

1.1.3 Previous Cases, Current Trends, and Key Challenges

Previous Cases (–2010): Ship Propulsion Motor and Large-scale Generator

From the 1980s to the present, considering the pros and cons of the superconducting rotating machines, large-scale machines have been mainly developed. Prior to 2000s, the development of large superconducting generators based on low-temperature superconductor (LTS) was mainly conducted. Since 2000s, the developments of ship propulsion motors and direct-drive wind turbine generators using high-temperature superconductor (HTS) have been carried out. However, although there are many research and demonstration cases around the world, the reported cases that are finally commercialized and are still being operated are rare. This assumed to be due to the high cooling costs, the difficulty of protecting large superconductor coils, and thermal instability problems [17–19]. The major research cases are summarized as follows.

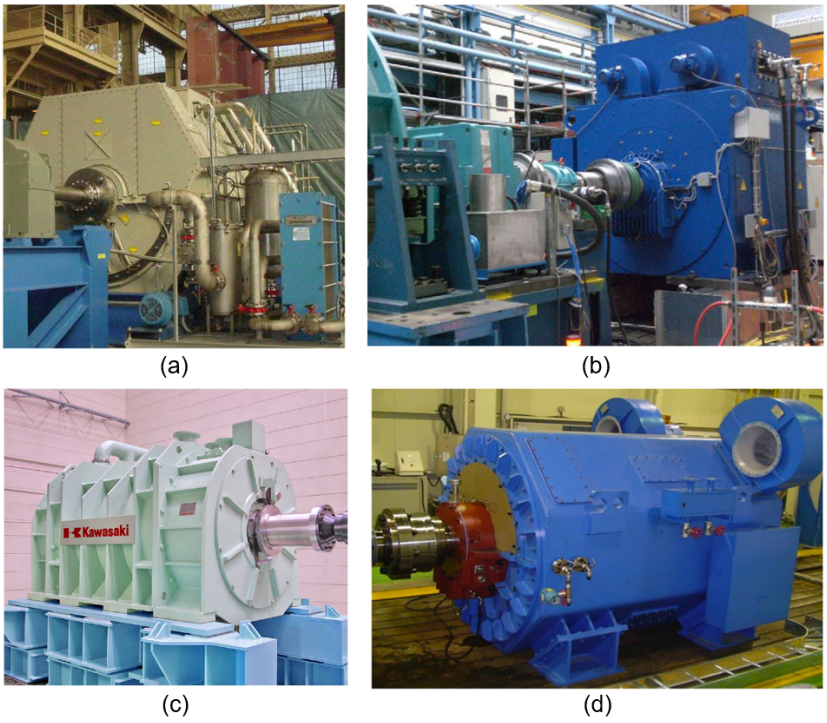

Figure 1.6: Previous superconducting rotating machine projects [12, 17, 20, 21]. (a) AMSC's 36.5 MW 120 rpm motor, (b) Siemens' 4 MW 120 rpm generator, (c) KHI's 3 MW 160 rpm motor, and (d) DHI's 5 MW 213 rpm motor.

- **USA - General Electric (GE) & American Superconductor (AMSC):** from the late 1970s to the early 1980s, GE manufactured superconducting generators and superconducting motors based on LTS (NbTi) [22, 23]. Since the early 2000s, AMSC had been manufacturing superconducting motors based on HTS (BSCCO). They constructed a 3.7 MW 1,800 rpm industrial motor in 2001, a 5 MW 230 rpm class marine motor in 2004, and a 36.5 MW 120 rpm class marine motor in 2007 [12, 24, 25].

- **Germany - Siemens:** based on the BSCCO wire, Siemens constructed a 380 kW 1,500 rpm motor for demo purposes in 2001 and developed a 4 MW 120

rpm superconducting generator in 2010 [20, 26].

- **Japan - Kawasaki Heavy Industry (KHI):** in 2010 and 2012, KHI of Japan developed a 1 MW 190 rpm ship propulsion motor and a 3 MW 160 rpm ship propulsion motor based on BSCCO wire, respectively [21].

- **Korea - Korea Electrotechnology Research Institute (KERI) & Doosan Heavy Industry (DHI):** as part of the DAPAS (Development of the Advanced Power system by Applied Superconductivity technologies) project in Korea, research on superconducting motors has been conducted since 2001 through collaboration between KERI and DHI. A 75 kW 1800 rpm demo motor and a 1 MW 3,600 rpm industrial motor were developed based on BSCCO wire in 2005 and 2008, respectively. And, a 5 MW 213 rpm ship propulsion motor was developed based on REBCO coated conductor [17, 27, 28].

Current Research Trends (2015–): Aviation Motor for High Power Density

Recently, as the development of high power density motors becomes an important issue for the development of alternative-fueled airplanes, the development of superconducting motors for aviation applications is being actively carried out. Since the development targets have a smaller scale and higher speed than the previously developed superconducting machines, the developments of the compact cooling system and non-superconducting components introduced in the previous section are also becoming important research issues. In some projects, not only the superconducting motor itself but also the propulsion system coupled with liquid hydrogen (LH_2) technology are actively studied. A fully superconducting motor is also considered to achieve even higher power density.

- **USA - NASA-Internal & CHEETA & ARPA-E ASCEND:** NASA Glenn Research Center is developing a 1.4 MW 6,800 rpm superconducting motor as an

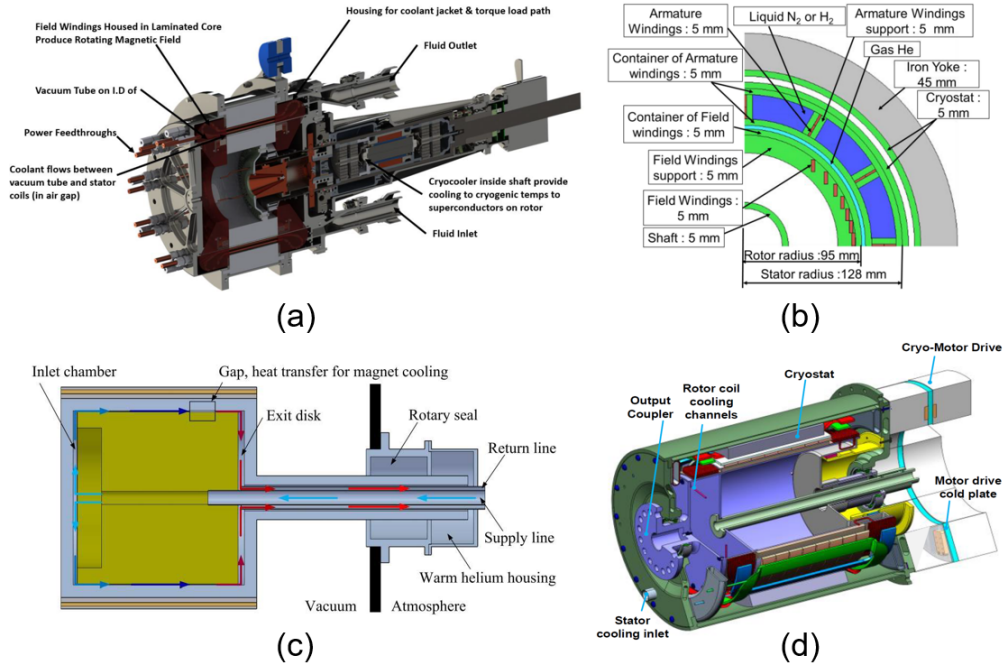

Figure 1.7: Ongoing superconducting motor projects [29–32]. (a) 1.4 MW 6,800 rpm motor by NASA, (b) Superconducting motor project by AIST, (c) ASuMED project in EU, and (d) Superconducting motor project by Raytheon Technologies.

internal project. No-insulation superconductor coils are applied to the motor design, which is discussed in this study, and development is in progress with a target of output density of $>$16 kW/kg. The Center for High-Efficiency Electrical Technologies for Aircraft (CHEETA) is conducting research on the entire superconducting electric propulsion system for aircraft, including superconducting motors. ARPA-E ASCEND Project is a project carried out by Raytheon Technologies. Superconducting motors and cryogenic cooling motor drives are under development in the project [7, 29, 31].

- **Europe - ASuMED & MAI:** Advanced Superconducting Motor Experimental Demonstrator (ASuMED) is a project carried out as part of Europe's Hori-

zon 2020 program and aims to demonstrate superconducting motors for aircraft. Moscow Aviation Institute (MAI) in Russia has been continuously conducting research on superconducting motors for aircraft since 2013 and has developed 50 kW and 200 kW class superconducting motors. Recently, it was reported that the test flight of an airplane (Yak-40) equipped with a propulsion system based on a superconducting motor was successful [32–34].

- **Japan - AIST:** in Japan, as part of the NEDO (New Energy and Industrial Technology Development Organization) project, AIST (Advanced Industrial Science and Technology) is developing superconducting motors for aircraft. As the first demo model, a 1 kW 500 rpm motor was recently manufactured [30].

Major Challenges Need to be Solved

Although various countries and institutions are participating in the development of superconducting motors, there are still various problems to be solved. The key challenges are summarized as follows.

- **Challenge for high-temperature superconductor coil:** most of the superconducting motors currently under development adopt HTS wire. In many cases among them, problems regarding the operation reliability and protection from burn-out upon quench of the HTS coil have been continuously reported [17, 19]. This has been the one of the main reasons that commercialized applications with HTS have not been developed, despite the fact that HTS wire exceeds the performance of existing LTS wire. Even if other parts of the application were successfully manufactured, in that the problem of the HTS coil can lead to the failure of the whole system, this problem can be considered as one of the key problems to be solved first.

- **Challenge for compact cryogenic systems:** in order to apply a superconducting element to a rotating machine, a cryogenic cooling system to maintain a super-

conducting state must be included. Such a cryogenic system not only increases the size of the entire system but also complicates the structure of the motor itself. Therefore, in order to achieve high power and torque density, which are the advantages of superconducting motors, a compact cryogenic system for superconducting motors is an important factor. There are various design considerations and challenges associated with cryogenics such as the selection of cryogens or cryocoolers, development of compact chamber, minimization of heat intrusion, etc.

- **Challenge for electrical & mechanical connection system:** to keep the excitation of the rotating cryogenic superconductor coil, electrical and mechanical connections from the stationary part to the rotating part are required. For electrical connection, slip-ring is commonly used, but to excite superconductor coil operated at high current, optimized slip-ring needs to be developed. Also, as a mechanical connection, a rotary cryocooler or cryogen coupling for a rotating cryogenic system needs to be developed.

1.2 No-insulation High-temperature Superconductor Coil as Potential Technical Solution for Superconducting Motor

As described in the previous section, since the development of the HTS wire, the operation reliability and quench protection of HTS coils have been tricky problems for HTS magnet engineers. In this study, as a potential solution to this problem that occurs in superconducting motors, a motor with no-insulation (NI) technique is discussed. In this section, the background of the NI technique and previous studies are reviewed, and required studies are discussed.

1.2.1 Background of No-insulation High-temperature Superconductor Coil

Firstly suggested in 2011, an NI HTS coil refers to a superconductor coil wound with HTS tape without turn-to-turn insulation [35]. NI HTS winding technique makes the protection of HTS coil much easier and has been widely applied in HTS applications.

General Characteristics of No-insulation High-temperature Superconductor Coil

Because the resistance of the superconductor is zero under critical temperature, a current is flowing in a wound direction even without insulation between turns in steady-state, because contact resistance between turns is enough for insulation in steady-state. It means that even without insulation between turns, a nominal operation is possible. Meanwhile, when a local hot spot occurs due to an inner defect or external disturbance at a specific turn of the coil, the current can bypass through turn-to-turn contact, making it easier to protect the coil and improve operational reliability. The overall pros and cons of NI HTS coil are as follows.

- **Pros 1 - Robustness to defects and disturbances:** NI HTS coils show stable operation even with inner defects and external disturbances (figure 1.8 (a)), so a highly reliable coil could be fabricated and operated [36, 37].
- **Pros 2 - Prevention of permanent thermal damage:** when a quench occurs, a local hot spot could make permanent thermal damage to the insulated HTS coil. However, in NI HTS coils, local thermal runaway does not easily occur because the current could bypass the hot spots.
- **Pros 3 - Compact coil and improved mechanical properties:** by erasing insulation materials between turns, the coil can be more compact and its mechanical properties can be more robust because of no “soft” insulation materials in the coil. In addition, the winding process becomes simple.
- **Cons 1 - Charging delay due to leak current through turn-to-turn contacts:**

during charging-discharging of the NI HTS coil, charging-discharging delay happens due to its leak current through turn-to-turn contacts as shown in figure 1.8 (b). Also, in other transient operations (external magnetic field changes, operating current fluctuation, etc.), the leak current is generated so the magnetic field could be momentarily changed [38, 39].

- **Cons 2 - Additional AC loss from turn-to-turn Joule loss:** the leak current flows through the contact resistance between turns, so it becomes a source of additional AC loss. Therefore, in the case of the NI HTS coil, it is necessary to estimate this additional turn-to-turn Joule loss for cryogenic system design.

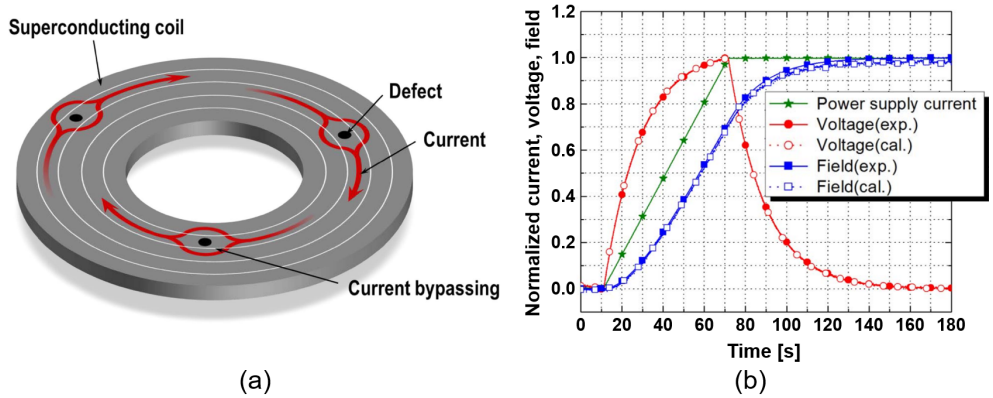

Figure 1.8: Major characteristics of no-insulation coil. (a) Defect-irrelevant behavior [36], (b) Charging delay due to leak current [39].

Major Applications of No-insulation High-temperature Superconductor Coil

Since the first suggestion of the NI winding technique in 2011, a lot of superconductor magnets have been manufactured and successfully achieved the target performance. In particular, it has been mainly applied to high-field magnets. Through these several experimental demonstrations, the NI technique is evaluated as experimentally proven technology. The demonstration cases include NI HTS insert magnets of 45.5 T magnets

from National High Magnetic Field Laboratory (NHMFL, USA), 26 T NI All-REBCO magnets from SuNAM (Korea), inter-layer NI HTS insert magnets for 31.4 T magnets from RIKEN (Japan), 32.5 T metal insulation HTS insert magnets from Grenoble Research Center (France), and 32.35 T NI HTS magnets from Chinese Academy of Sciences (CAS, China) [40–44].

Recently, paying attention to the potential of the NI HTS coil, the development of not only high-field magnets but also various applications using the NI HTS coil is underway worldwide [45–51]. Figure 1.9 shows examples of application development projects using NI HTS coils. Application fields include fusion tokamak magnets, accelerators, NMR magnets, transportation, and industrial magnets. A superconducting motor with NI HTS coils, which is the theme of this study, is also being developed by NASA Glenn Research Center.

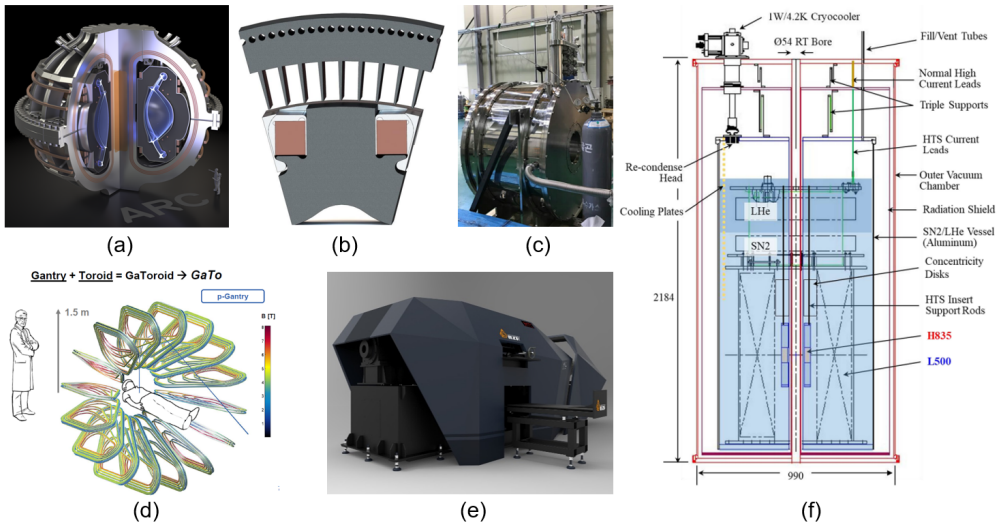

Figure 1.9: Various applications being developed based on NI techniques [45–51]. (a) Tokamak magnet by CFS-MIT (USA), (b) Superconducting motor by NASA, (c) Accelerator magnet by IBS-RAON, (d) GaToroid accelerator magnet by CERN, (e) Induction heater by SuperCoil, and (f) NMR magnet by MIT

1.2.2 Applicability of No-insulation High-temperature Superconductor Coil to Superconducting Motor

NI HTS coil's strength in protection and operation reliability could be a potential solution to the reliability problem of HTS coil in previous superconducting motors. But when applying NI HTS coil to motors, we need to consider NI HTS coil's unique characteristics due to leak current between turns, so-called *"NI characteristics."* Considering that due to charging delay by leak current, NI HTS coil cannot be used as an AC armature coil, but can be adopted as DC field coil of synchronous machine. If we use NI HTS coils as DC field coils, after synchronization, it would work fine theoretically because the current & magnetic field exposed to the NI HTS coil is DC in ideal conditions. It means the NI HTS coil can be applicable in principle, but additional research would be required to identify the detailed characteristic changes due to leak current in practical conditions in steady-state as well as transient operation.

Expectations for Applying No-insulation Technique to Motor Application

The main expectations for applying the NI HTS coil to the partial superconducting motor are as follows.

- **Improved protection and operation reliability of HTS field coil:** thermal instability and protection failure have been the main causes of failure in conventional HTS motor projects. The NI HTS coil has shown robust characteristics against defects and disturbances, and improved protection characteristic is verified in various magnet experiments.

- **Damping coil effect on d-axis of motor:** damping coils have been used to prevent hunting in some synchronous motors. Due to the turn-to-turn contact current path of the NI HTS coil, NI HTS coil might do the same role as damping coils previously used for synchronous motors. Figure 1.10 compares the equivalent circuit of a conventional synchronous motor with a damping coil and the

equivalent circuit of a synchronous motor with an NI HTS coil applied to the field coil. This shows that in the case of a motor to which the NI HTS coil is applied, there could be a similar effect as having a damping circuit on the d-axis without an additional damping coil.

- **Other unknown behaviors might be induced from NI behavior:** since there has been no demonstration case of synchronous motor adopting the NI HTS field coil, how the NI HTS field winding will react in practical operation situations has not been studied in detail so far. In particular, it is also necessary to discuss the effect of leak current that may occur during transient operation. Expectations for this unknowns on NI HTS coil became the study target of this study.

Previous Studies for No-insulation High-temperature Superconducting Motor

Since the NI HTS winding technique was first proposed, several studies have been conducted to apply the NI technique to superconducting rotating machines. Coil-level studies, which are the studies using a single NI HTS coil without an actual motor system, were mainly conducted as basic studies, also, some studies on motor design applying NI HTS coil were performed.

- **Coil-level studies as basic studies of NI HTS rotating machine:** Kim *et al.* fabricated a racetrack-type NI HTS coil which is suitable for rotating machines for the first time [52], and it was shown that the equivalent circuit model applied to the existing solenoid-type NI HTS coil can be applied to the racetrack coil in similar manners (figure. 1.11 (a)). Song *et al.* demonstrated that the NI HTS coil can generate Lorentz force without excessive leak current [53], by placing an additional insulated HTS coil that interacts with the NI HTS coil (figure. 1.11 (b)). Also, NI HTS coils' characteristic when an external field is applied is investigated by Choi *et al.* [37], considering that the field coils could be exposed to a changing external magnetic field by harmonic field components (figure.

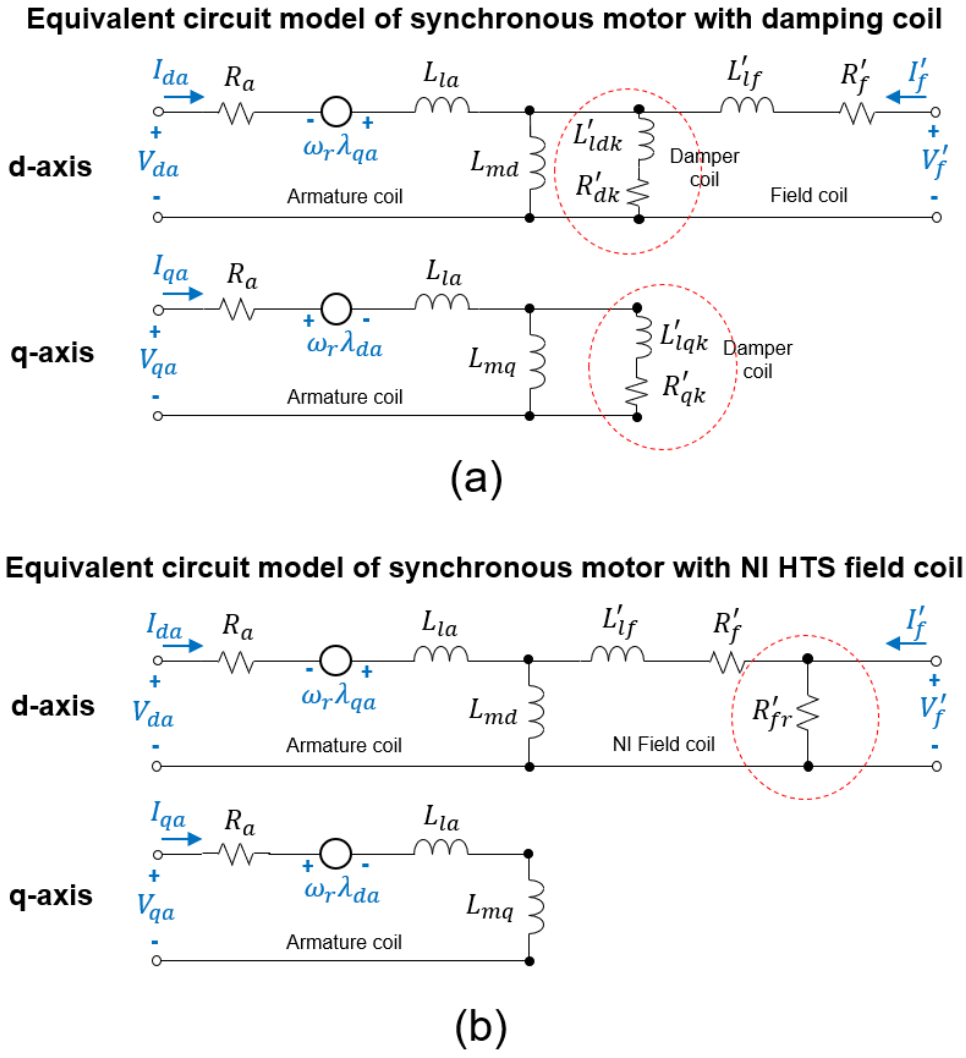

Figure 1.10: Damping circuits in synchronous motor and NI HTS motor. (a) Circuit model of synchronous motor with damping coils, (b) Circuit model of NI HTS motor.

1.11 (c)). In the study, NI HTS coils show more stable characteristics in terms of terminal voltage compared with insulated counterparts.

- **Design studies on NI HTS rotating machine:** there have been a few cases where design studies on NI HTS motors are conducted. However, the operation characteristic change by NI behaviors was not studied in detail, and in some papers, the designs were conducted assuming the NI HTS coil would work exactly the same as the insulated one in steady-state [2, 54, 55].

1.2.3 What Needs to be Studied for NI HTS Motor: Requirements of Analysis Model and Experimental Study

Previous works were almost limited to coil-level study, even for motor design, limited to steady-state characteristics and performance with ideal conditions assumed. However, as long as there are unknowns about the behavior of NI HTS field winding in the synchronous motor, the applicability of NI technique to superconducting motor cannot be determined. Therefore, for NI HTS motor, research on applicability of NI technique to superconducting motors is required first as a key question, and for this, the following research is needed.

- **Proposal of an analysis model for NI HTS motor:** in the case of previous studies, there was no proper analysis model considering the NI characteristics that may occur during motor operation. Therefore, it is required to present a proper analysis model reflecting the NI characteristics in the motor operations and to analyze the characteristics through it.

- **Actual demonstration of NI behavior in motor operation:** the key question about NI HTS motor can be directly investigated with an actual demonstration. Also, in terms of verification of the analysis model, actual demonstration is required even on a small scale.

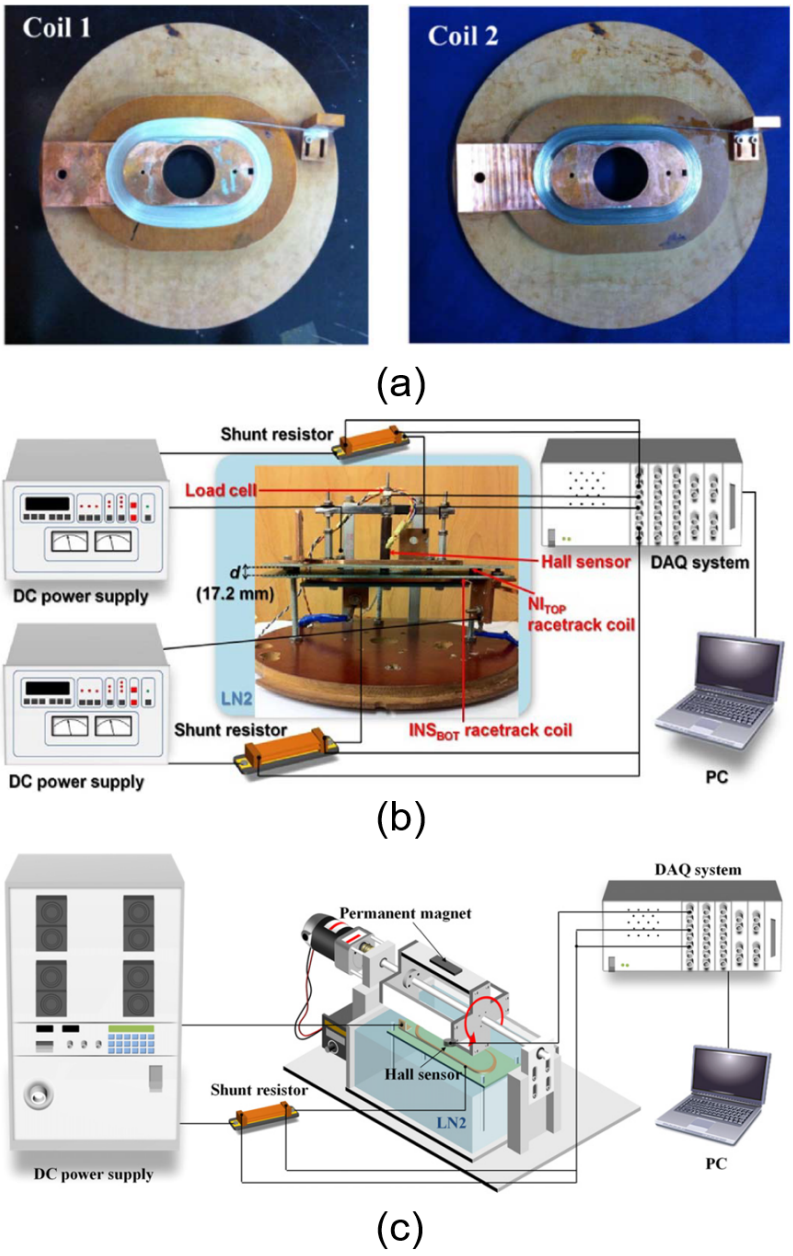

Figure 1.11: Previous coil-level studies for NI HTS machine [37,52,53]. (a) Derivation of an equivalent circuit of NI HTS racetrack coil, (b) Lorentz force measurement, and (c) NI behavior under external magnetic field ripple.

1.3 Goal and Significance of this Study

Goal of the Study

This study discusses the applicability of NI HTS field winding to superconducting motors, in that NI HTS field winding can be a solution to the problems of operation reliability and quench protection of HTS coils in conventional HTS motors. So, it is needed to note that this study is not to show high power density compared to conventional motors but to study one of the techniques that could help realize high power density superconducting motors by exploring areas that have not been studied. The detailed goals of the study are as follows.

- Proposal of an analysis model for a superconducting motor with NI HTS field winding
- Design and construction of a test-purposed superconducting rotating machine with NI HTS field winding and experimental systems
- Experimental observation and analysis on operation characteristics of NI HTS field winding as well as NI HTS motor
- Establishment of other analysis and design techniques required for superconducting motor demonstration

Significance of the Study

- **First proposal of analysis model for "NI" HTS rotating machine:** the analysis model of the NI HTS motor is firstly proposed in this paper. Based on this, it is possible to analyze the operation characteristics of the NI HTS motor considering the turn-to-turn leak currents of the NI HTS coil. Also, it is expected that a control algorithm suitable for the characteristics of NI HTS motors can be developed based on this analysis model.

- **Verification on the applicability of NI HTS field winding to superconducting motor through actual experiments:** the concept of NI HTS motors has been continuously discussed since the NI technique was proposed. However, since the main research was limited to coil-level studies or simulations, there was no case of experimentally researching the actual applicability of NI HTS field winding. In this paper, the concept of the NI HTS motor is experimentally proven by manufacturing and testing the simple NI HTS motor.

- **Experimental observation of non-linear behavior of NI HTS field winding in motor operation:** since there was no actual demonstration case of the NI HTS motor, there was no report of how the NI HTS field winding responds in an actual operation situation. In this study, such an NI response was first observed, and the mechanism of non-linear behavior was analyzed with the proposed analysis model.

1.4 Structure of the Thesis

This thesis consists of a total of 7 chapters.

Chapter 1 “INTRODUCTION” describes the research background, goals, and significance of the research. In the background of the study, the reason for the need to develop a superconducting motor is introduced, and the results of previous superconducting motor studies are reviewed. By applying NI HTS coils, the possibility of improving the reliability and protection problems of the conventional HTS motors is considered, and the overall direction of the study is set.

In chapter 2 “THEORETICAL BACKGROUND ON SUPERCONDUCTIVITY AND SUPERCONDUCTOR WIRE”, the theoretical background of superconductivity and superconductors necessary for the development of HTS motors is briefly reviewed. Especially, the main characteristics of HTS wire (REBCO) that should be considered when designing a test motor are described.

In chapter 3 “ANALYSIS METHODS OF COIL AND ROTATING MACHINE ADOPTING NO-INSULATION TECHNIQUE,” key analysis methods for NI HTS coils are reviewed. Based on previously established analysis models, the first analysis models are proposed for the characteristic analysis of NI HTS motors.

In chapter 4 “DESIGN OF TEST MACHINE AND EXPERIMENTAL SYSTEM FOR APPLICABILITY TEST OF NI HTS FIELD WINDING,” a test machine with NI HTS field winding for a demonstration is designed. For the actual test, a liquid nitrogen-based cooling chamber and motor test system are also designed considering various characteristics in terms of electromagnetic, mechanical, and thermal.

Chapter 5 “CONSTRUCTION OF TEST MACHINE AND EXPERIMENT SYSTEM” describes the manufacturing process of the test machine with NI HTS field winding, liquid nitrogen cooling chamber, and motor test system designed in the previous chapter. The winding process of the NI HTS coils, the configuration of the rotor assembly, and the instrumentation of the test system are described.

Chapter 6 “EXPERIMENTAL STUDY ON APPLICABILITY OF NI HTS FIELD WINDING TO SUPERCONDUCTING MOTOR” summarizes the experimental results based on the constructed test system. The overall performance of the motor was reviewed based on experiment results, and the non-linear behavior of the NI HTS field winding was analyzed through the proposed analysis model. The key findings found in the experimental results are summarized.

In chapter 7 “CONCLUSION”, the conclusion of this thesis and required improvements are written.

Chapter 2

THEORETICAL BACKGROUND ON SUPERCONDUCTIVITY AND SUPERCONDUCTOR WIRE

Before discussing NI HTS field winding and the motor to which it is applied, this chapter briefly describes the background of superconductivity and superconductor wires required for the design of HTS motor. The fundamental theories, types, and properties of superconductor would be introduced. And, key properties of (RE)$Ba_2Cu_3O_{7-x}$ (REBCO) coated conductor, which is actively researched recently for HTS applications and used for this study as NI HTS field winding, is presented.

2.1 Superconductivity

Superconductivity is a set of physical properties observed in certain materials where electrical resistance vanishes and magnetic flux fields are expelled from the material in certain conditions. Any material exhibiting these properties is considered a superconductor [56]. Superconductivity is commonly characterized with "Meissner effect," the complete ejection of magnetic field from the interior of the superconductor during its transitions into the superconducting state. Meissner effect indicates that superconductors cannot be simply understood as the ideal perfect conductors in conventional electromagnetics, which is simply their electrical resistivity is zero. To maintain the

superconductivity, superconductors should be below a certain "critical temperature (T_c)," a certain "critical magnetic field (B_c)," and a certain "critical current density (J_c)." Values of T_c, B_c, and J_c are different according to superconductor materials. Superconductors can be classified based on their physical properties. Here, the classification of type-I superconductor and type-II superconductor and the classification of low temperature superconductor (LTS) and high temperature superconductor (HTS) will be introduced.

2.2 Classification of Superconductors

2.2.1 Type-I and Type-II Superconductor

Superconductors can be classified into type-I and type-II based on response to a magnetic field.

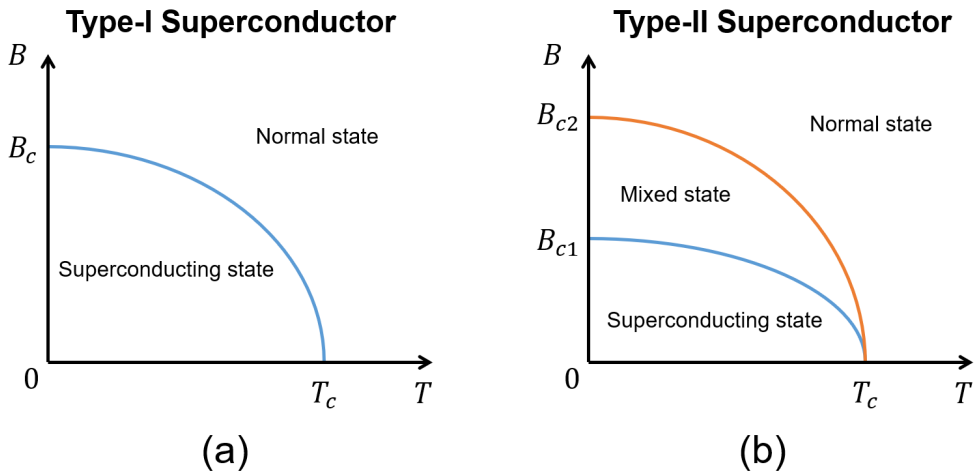

Figure 2.1: Phase diagram of (a) type-I and (b) type-II superconductors.

Type-I Superconductor

Type-I superconductors have a single critical magnetic field (B_c) as shown in figure 2.1 (a), and lose their superconductivity easily and abruptly at B_c compared to type-II superconductors. Type-I superconductors perfectly obey the Meissner effect, which means penetration of magnetic field is not allowed under magnetic field lower than B_c. B_c of type-I superconductors is typically less than 10^5 A/m or $\sim$0.1 T. Because of their low B_c value, type-I superconductors are considered not suitable for superconductor magnet applications. Typical examples of type-I superconductor include aluminum (B_c = 0.0105 T) and zinc (B_c = 0.0054 T).

Type-II Superconductor

Type-II superconductors have two critical magnetic fields (B_{c1} and B_{c2}) as shown in figure 2.1 (b). When the magnetic field becomes higher than the lower critical field (B_{c1}), type-II superconductor starts to lose their superconductivity, and partial penetration of the magnetic field happens through vortices generated in superconductors. It means that type-II superconductors do not perfectly obey the Meissner effect. When the magnetic field becomes higher than the upper critical field (B_{c2}), type-II superconductors now lose their superconductivity perfectly. A state between B_{c1} and B_{c2} is called a mixed state or intermediate state. Typically, B_{c2} is $>$0.1 T and in some cases $>$20 T, so type-II superconductors are considered suitable for superconductor magnet applications. Currently, all commercial superconductor wires used for magnets are based on type-II superconductors. Typical examples of type-II superconductors include NbTi, Nb_3Sn, MgB_2, YBCO, and BSCCO.

2.2.2 Low-temperature Superconductor and High-temperature Superconductor

Superconductors are also classified into a low-temperature superconductor (LTS) and a high-temperature superconductor (HTS), based on their critical temperature (T_c).

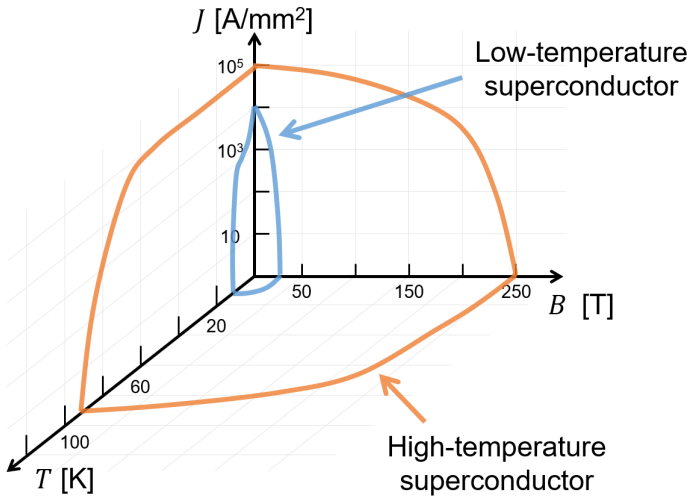

Figure 2.2: Comparison of critical values between LTS and HTS [57].

Low-temperature Superconductor (LTS)

Superconductors with relatively lower T_c (typically below 30 K, which is predicted as the limit of superconductivity by Bardeen–Cooper–Schrieffer theory [58]) are referred to as LTS [59]. There are a variety of LTS materials, but NbTi (T_c = 9.2 K) and Nb_3Sn (T_c = 18.3 K) are the most common materials used to make superconductor wires. Because T_c is relatively low, applications with LTS typically require cooling to 4.2 K using liquid helium (LHe), which is one of the main reasons for the high operating cost of LTS-based applications [60]. Also, due to the relatively lower critical field (B_c) as shown in figure 2.2, feasible generation of magnetic field intensity with an LTS magnet is limited to $<$15 T. Most of the commercialized superconductor magnet applications are based on LTS wire, and typical applications include MRI, NMR, accelerator, and fusion.

High-temperature Superconductor (HTS)

Superconductors with relatively higher T_c (generally above 30 K) are considered HTS [61]. Major HTS materials used as superconductor wire are REBCO including YBCO (T_c = 92 K) and GdBCO (T_c = 91 K), ...), BSCCO including Bi2212 (T_c = 96 K) and Bi2223 (T_c = 108 K), and MgB_2 (T_c = 39 K). Due to their higher T_c, various cryogens (liquid helium - 4.2 K, liquid hydrogen - 20 K, liquid neon - 27 K, and liquid nitrogen - 77 K) and cryocoolers could be used for cooling HTS-based applications. It means that there are other applicable cooling options except "expensive" LHe cooling for HTS applications. Also, HTS has usually higher B_c compared to LTS, so a much higher magnetic field could be reached with an HTS-based magnet (e.g., 45.5 T generation using HTS insert and LTS background magnet in 2019 at NHMFL [40]). Due to their high potential, various applications using HTS are being studied since their presence.

However, despite their higher T_c and B_c, HTS technology has not been successfully applied to commercial applications like LTS so far. There are various reasons such as expensive HTS conductor price and in-mature manufacturing technology, but one of the key challenges is the difficulty of protecting the HTS coil in quench (sudden disappearance of superconductivity). Compared to typical LTS wires (NbTi and Nb_3Sn) which are based on alloys, major HTS wires (YBCO and GdBCO) are based on ceramic materials. In LTS, due to their relatively low heat capacity and high thermal conductivity, fast quench propagation occurs and stored energy can be dissipated over a wide range within the magnet. However, ceramic-based HTS has a much slower quench propagation speed compared to LTS because of high heat capacity and low thermal conductivity, and it leads to a dangerous local "hot spot" of a coil in the quench, which could damage the HTS magnet permanently. The difficulty of protecting this hot spot in HTS magnet has been a technical challenge for the successful commercialization of HTS applications. Therefore, research on HTS applications with better protection techniques, such as the no-insulation (NI) winding technique, are being actively performed recently [45–51].

2.3 Key Properties of (RE)$Ba_2Cu_3O_{7-x}$ Coated Conductor

In this study, (RE)$Ba_2Cu_3O_{7-x}$ (REBCO) coated conductor, one of the HTS wires, was selected as a superconductor wire to be used for the design and fabrication of the test motor. Figure 2.3 shows a typical structure of REBCO coated conductor [62]. It consists of a substrate, buffer layers, REBCO superconductor layer, and stabilizer layers. As a substrate, stainless steel and Hastelloy are mainly used, and various buffer layers are deposited on it. A REBCO superconductor layer is placed on the deposited buffer layer, a silver overlayer is added, and a copper stabilizer layer is coated on both sides of the wire.

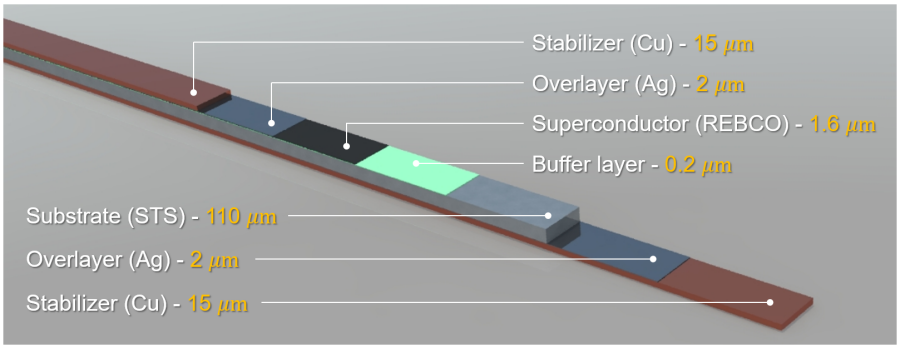

Figure 2.3: Typical structure of REBCO coated conductor.

Considering superconductors' properties explained in the previous section, the following advantages are available in terms of conductors when designing and fabricating a superconducting motor using REBCO coated conductors.

- Due to its high T_c, various cooling methods including LN_2 cooling (77 K) can be applied, thereby simplifying the cooling system.
- With high J_c and B_c, it is possible to secure the output of the motor even at a relatively high operating temperature.
- Through the application of the NI technique, the protection of the coil, which

was a major problem of the HTS coil, can be improved.

- Various major manufacturers exist, and supply of conductors from a domestic company is possible.

In this study, a 4.1 mm width REBCO coated conductor manufactured by SuNAM is selected to be used. The key properties of the SuNAM's REBCO coated conductor are as follows.

Electromagnetic Property: Field-dependent Critical Current

Superconductors show an electromagnetic characteristic that the critical current (I_c) decreases as the magnetic field strength ($|B|$) increases. In the case of REBCO coated conductor, due to the anisotropy of the molecular structure, it shows additional electromagnetic property affected by the angle of the magnetic field (θ_f) [63]. Because superconducting applications are commonly designed to generate a high magnetic field and the superconductor coil itself is exposed to its magnetic field, this field-dependent $I_c(|B|,\theta_f)$ characteristic is quite important in the design process. Figure 2.4 (a) shows $I_c(|B|,\theta_f)$ characteristics of SuNAM 4.1 mm REBCO coated conductor at 77 K [64]. The x-axis represents the angle between the c-axis of the REBCO coated conductor and the magnetic field (θ_f), and the y-axis represents $I_c(|B|,\theta_f)$. It can be seen that I_c increases, as the value of $|B|$ is larger and the value of θ_f is closer to 90 degrees.

Electro-mechanical Property: Strain-dependent Critical Current

In REBCO coated conductor, when mechanical strain over a certain level is applied, the critical current (I_c) decreases. When the coil wound with REBCO coated conductor is excited, it is subjected to a hoop strain (ε_h) extending in the longitudinal direction by receiving the Lorentz force induced by magnetic field and current. Therefore, $I_c(\varepsilon_h)$ acts as one of the mechanical constraints in the design process. Figure 2.4 (b) shows the electro-mechanical properties of various commercial REBCO coated conductors

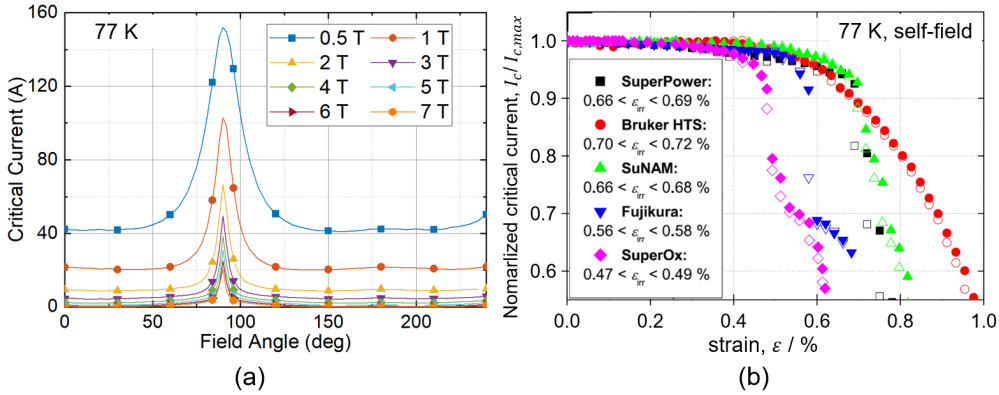

Figure 2.4: Key properties of SuNAM's REBCO coated conductor. (a) field-dependent I_c at 77 K, (b) Electro-mechanical property at 77 K, self-field.

measured at 77 K in the absence of an external magnetic field [65]. When strain is lower than 0.4%, I_c maintains its value, but when strain over 0.4% is applied to the conductor, it can be seen that I_c decreases significantly.

Chapter 3

ANALYSIS METHODS OF COIL AND ROTATING MACHINE ADOPTING NO-INSULATION TECHNIQUE

This chapter describes the basic electromagnetic analysis technique of superconductor coil and the characteristic analysis method of NI HTS coil. Based on the analysis techniques of a single superconductor coil, analysis models of the NI HTS motor are further proposed. Depending on the structure of the coil and the topology of the motor, the required analysis technique may be slightly different. For coils, this chapter focuses on analysis techniques of superconductor coil wound with REBCO coated conductor, especially "racetrack-type" coil, which is commonly used in motor applications [37, 52–55, 66, 67]. For motors, analysis models of a partial superconducting synchronous motor with NI HTS field winding are proposed.

Table 3.1 represents the geometric parameters of the coil to be used for the following coil analysis sections. The coil is an 80-turn single pancake racetrack coil and was designed to be wound using SuNAM's 4.1 mm REBCO coated conductor. The geometric parameter of the coil was derived through the test motor design process, and how the parameter is determined will be described in detail in chapter 4.

Table 3.1: Racetrack Coil Parameters for Coil Analyses

Parameters		**Values**
Conductor thickness (t_{cd})	[mm]	0.14
Conductor width (w_{cd})	[mm]	4.1
Inner radius of circular section (r_i)	[mm]	28
Outer radius of circular section (r_o)	[mm]	39.2
Length of straight section (l)	[mm]	180
Number of turns (N_t)		80

3.1 Electromagnetic Analysis Model of Superconductor Coil

An electromagnetic analysis is the first step to analyzing the basic performance of a REBCO racetrack coil. Through electromagnetic analysis, magnetic field strength and distribution are derived, and electromagnetic parameters of the coil (inductance, field constant, etc.) are obtained. Also, operation current (I_{op}) is decided by estimating the critical current (I_c) of the coil.

3.1.1 Magnetic Field Analysis Based on Finite Element Method

A 2D magnetic field analysis that considers only the straight section of the racetrack coil is often used in the analysis of rotating machines for simple time-dependent simulation. However, a 3D static magnetic field analysis is required to consider the end-effect of the circular section for the derivation of electromagnetic parameters of a single racetrack coil. Some analytical approaches have been proposed to analyze the magnetic field and inductance of a racetrack-type coil considering the 3D shape of racetrack coils [68, 69], but not widely used because the thickness of the coil is ignored or it includes complex numerical integration. Instead, numerical calculations such as the finite element method (FEM) can be effectively utilized for electromagnetic analysis.

In the case of REBCO coated conductor, a type-II superconductor, the lower crit-

ical magnetic field (B_{c1}) is less than 0.1 T, and it maintains a mixed state under most operating conditions. Accordingly, it is possible to obtain more precise results by performing numerical calculations with relative permeability $\mu_r = 1$ rather than with perfect diamagnetism caused by the Meissner effect. Therefore, with these properties, static field analysis is performed by applying the same governing equations as those applied to general non-superconducting coils. The governing equations used for electromagnetic analysis in FEM are derived from the following Maxwell's equations [70].

$$\nabla \times \boldsymbol{H} = \boldsymbol{J} + \frac{\partial \boldsymbol{D}}{\partial t}, \tag{3.1}$$

$$\nabla \times \boldsymbol{E} = -\frac{\partial \boldsymbol{B}}{\partial t}, \tag{3.2}$$

$$\nabla \cdot \boldsymbol{D} = \rho_c, \tag{3.3}$$

$$\nabla \cdot \boldsymbol{B} = 0. \tag{3.4}$$

Equations (3.1)–(3.4) represent Ampere's circuital law, Faraday's law, Gauss's law, and Gauss's law for magnetism in order. $\boldsymbol{H}$, $\boldsymbol{B}$, $\boldsymbol{E}$, $\boldsymbol{D}$, $\boldsymbol{J}$, and ρ_c are magnetic field strength, magnetic flux density, electric field strength, electric flux density, current density, and charge density, respectively.

At this time, the problem to be solved here is the "Magneto-statics" condition, which is a time-invariant condition without an electric charge source. Therefore, Ampere's circuital law (3.1) and Gauss's law for magnetism (3.4) are used as the governing equations [8]. As a stationary condition, it can be assumed that $\boldsymbol{D} = 0$, so governing equations are simplified as follows.

$$\nabla \times \boldsymbol{H} = \boldsymbol{J}, \tag{3.5}$$

$$\nabla \cdot \boldsymbol{B} = 0. \tag{3.6}$$

Also, the constitute relation and continuity equation are given as follows.

$$\boldsymbol{B} = \mu \boldsymbol{H}, \tag{3.7}$$

$$\boldsymbol{J} = \sigma_e \boldsymbol{E}. \tag{3.8}$$

Here, σ_e means electrical conductivity. The above equations (3.5)–(3.8) are finally given as the governing equations in FEM analysis.

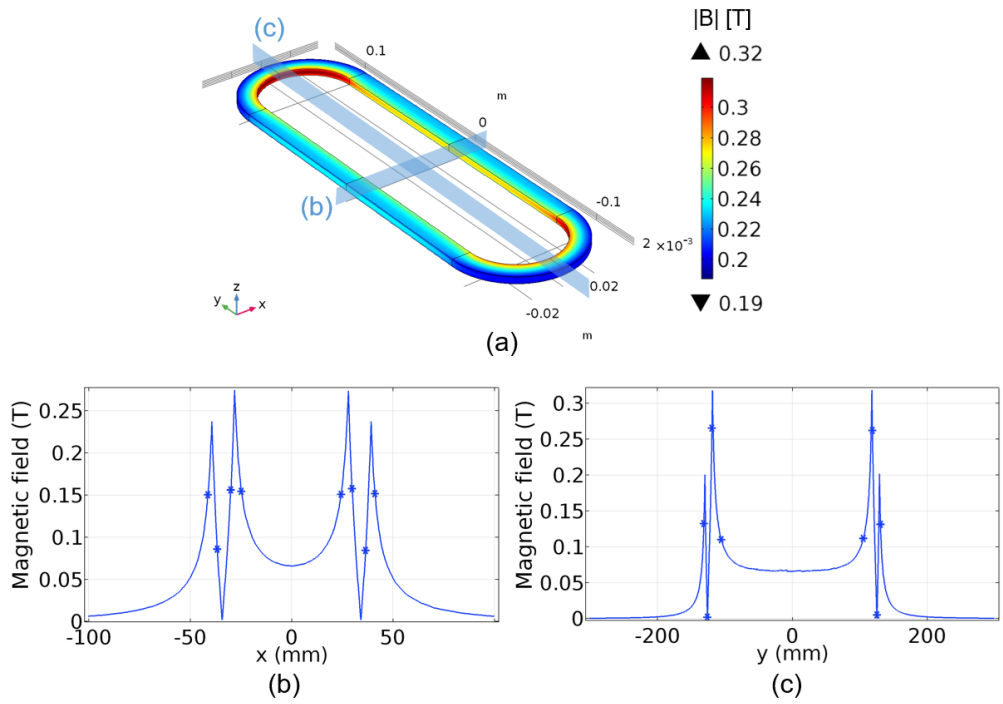

Figure 3.1: FEM analysis results of magnetic flux density (a) on the racetrack coil surface, (b) along with the x-axis coordinates, and (c) along with the y-axis coordinates.

When only the excited racetrack coil exists in the 3D space, the magnetic field distribution is calculated based on the above governing equations. Figure 3.1 is the magnetic field calculation result of the racetrack coil based on the parameters given in table 3.1. Here, the operating current is 66.2 A. Since the analysis is performed in the absence of ferromagnetic material, the magnetic field distribution appears dependent on the shape of the coil. The closer to the coil, the stronger the magnetic field strength, and the peak magnetic field was calculated inside the circular section. Figure 3.1 (c) shows the magnetic field distribution along with the y-axis when $x = z = 0$, and it

can be seen that the magnetic field distribution appears relatively uniformly inside the coil along the straight section. Finally, based on the calculated magnetic field analysis result, the inductance of the coil can be calculated using the energy method ($L = 2E_m/I_{op}^2$, where E_m is magnetic stored energy) [70]. The inductance of the coil was calculated to be 2.05 mH. Field constant (K = center magnetic field / operating current) is calculated to be 0.994 mT/A.

3.1.2 Critical Current Estimation with Load Line Method

One of the key analysis targets of electromagnetic analysis of a superconductor coil is to estimate the critical current (I_c) of the coil and determine the proper operating current (I_{op}) with enough margin. Considering the REBCO coated conductor's field-dependent $I_c(|B|, \theta_f)$ previously presented in figure 2.4 (a), we need to determine I_c at coil level, which means the minimum current value at which the superconductivity begins to disappear in the coil. I_c is calculated to be different in each turn of the coil because exposed magnetic field intensity and field angle are different. Usually, I_c of the coil is determined as the minimum I_c value in the coil's I_c distribution.

To derive the I_c distribution in the coil, based on I_c measurement data of the conductor at each temperature, the field-dependent $I_c(|B|, \theta_f)$ function is interpolated and used. As the $I_c(|B|, \theta_f)$ model, a simple linear interpolated model is used, or models based on a formula describing superconductivity such as the Kim-Anderson model [71] or Hilton's model [72] are used. In this study, Hilton's fit-function was used, and the model is given as follows.

$$\begin{aligned} I_c(|B|, \theta_f) =& \frac{k_0}{(|B| + \beta_0)^{\alpha_0}} + \frac{k_1}{(|B| + \beta_1)^{\alpha_1}} \\ & \times [\omega_1^2(|B|) \cos^2(\theta_f - \varphi_1) + \sin^2(\theta_f - \varphi_1)]^{-1/2}, \end{aligned} \tag{3.9}$$

$$\omega_1(|B|) = c_1 \left[|B| + \left(\frac{1}{c_1} \right)^{1/0.6} \right]^{0.6}. \tag{3.10}$$

In the above formula, k_0, k_1, α_0, α_1, β_0, β_1, φ_1, and c_1 are fit parameters.

Table 3.2: Fit Parameters of I_c Fit-function at 77 K

Parameters	k_0	k_1	α_0	α_1	β_0	β_1	φ_1	c_1
Values	289	172	3.17	1.02	1.58	0.801	0.226	16.6

Table 3.2 shows fit parameters obtained using the curve fitting toolbox in MATLAB [73], based on I_c measurement data at each temperature from Victoria Wellington University, shown in figure 2.4 (a) [64]. By adopting the derived $I_c(|B|, \theta_f)$ function to the magnetic field analysis results, I_c was estimated at each point of the coil. Since there are differences in the values of magnetic field and angle even along the width of REBCO coated conductor, firstly J_c of each point is calculated, then calculated J_c is integrated along the width of conductor to obtain I_c of each turn.

Figure 3.2 shows I_c calculation result. When there is no external magnetic field and magnetic materials, the minimum critical current point of a single racetrack coil is usually identified at the inner radius of the curved section, where magnetic field intensity is maximized.

Here, the operating current (I_{op}) of the coil can be determined with the so-called "load-line" method as shown in figure 3.2 (a) [74]. When coil's I_{op} is increased, I_c is decreased because of self-field increment. So, when plotting I_{op} and I_c along with the I_{op}, the crossing-point of I_{op} and I_c is considered as I_c of the coil. To have enough margin during operation, I_{op} is determined lower than I_c (typically 20–30%). The gap between I_c and I_{op} is called the current margin. In this study, I_c was calculated to be 94.6 A, and I_{op} was determined to be 66.2 A with a margin of 30%.

3.2 Analysis Model of NI Characteristics in NI HTS Coil

In this section, in addition to the general electromagnetic analysis performed in general superconductor coils, an analysis method for analyzing the NI behavior additionally required for the characteristics analysis of NI HTS coils is described. In the case of an

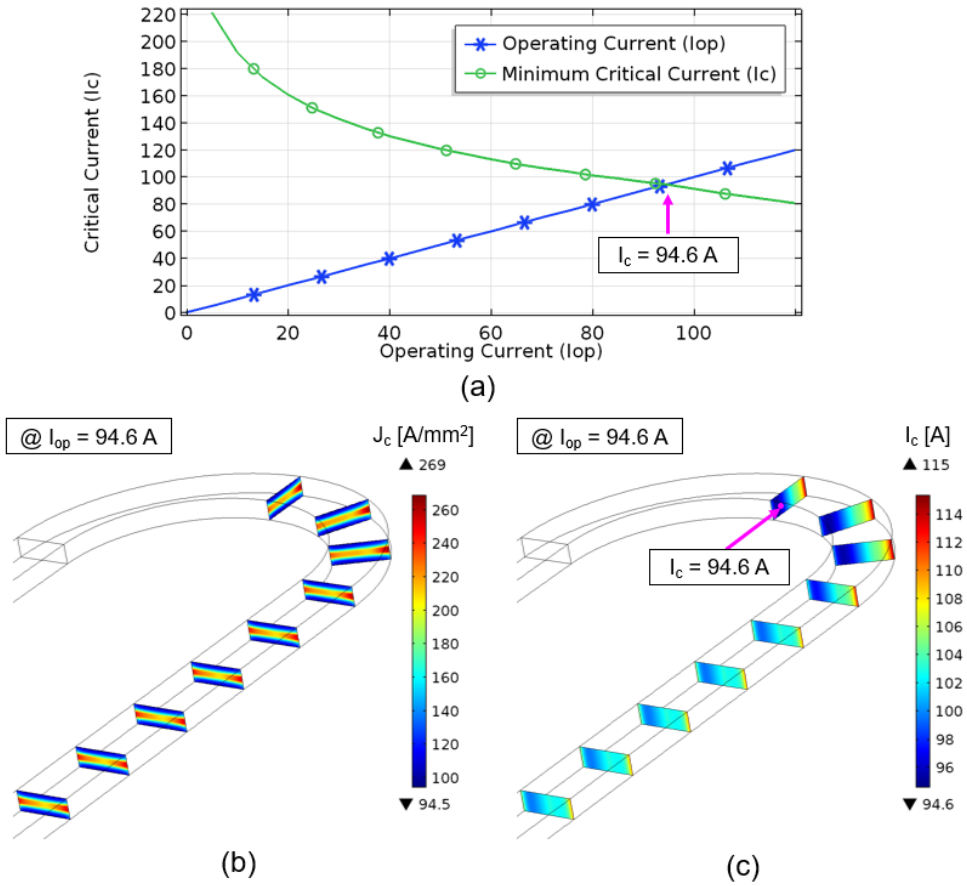

Figure 3.2: Critical current calculation of racetrack coil. (a) load line analysis, (b) J_c distribution when I_{op} = 94.6 A, (c) I_c distribution when I_{op} = 94.6 A.

NI HTS coil, except current path along the winding, there is another resistive current path through turn-to-turn contact, thus so-called leak current exists in transient operation. Therefore, consideration of leak current is required for proper operation in the design step. For modeling of the NI HTS coil, lumped parameter circuit model, turn-distributed circuit model, and partial equivalent element circuit (PEEC) model have been proposed [75–78]. In this study, the equivalent circuit analysis of the NI REBCO racetrack coil was performed based on the lumped parameter circuit model.

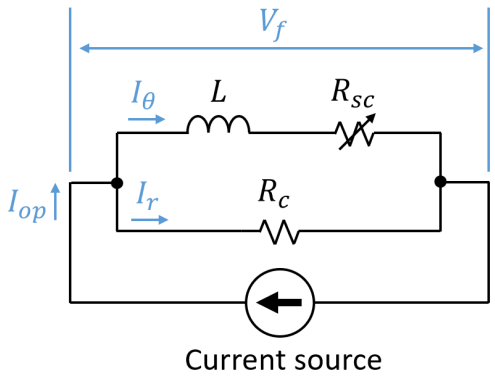

Figure 3.3: Lumped parameter equivalent circuit of NI HTS coil.

Figure 3.3 shows the lumped parameter circuit model of the NI HTS coil. L, R_c, R_{sc}, I_θ, I_r, and V_f are the inductance of the coil, the characteristic resistance of the coil, the resistance of the superconductor, the current flowing along the winding path, the current flowing through the turn-to-turn contact path, and the terminal voltage of the coil, respectively.

In the circuit, the resistive path through turn-to-turn contact of an NI HTS coil is expressed by R_c. R_c is obtained as the sum of each turn-to-turn contact resistance. Basically, the coil is actually spirally wound and the contact surface exists also in a spiral shape, but it can be approximated that the multiple closed contacts overlap in several layers as shown in figure 3.4 [38]. Here, based on assumption that the current is flowing evenly through all contact (which means that turn-to-turn contact resistivity

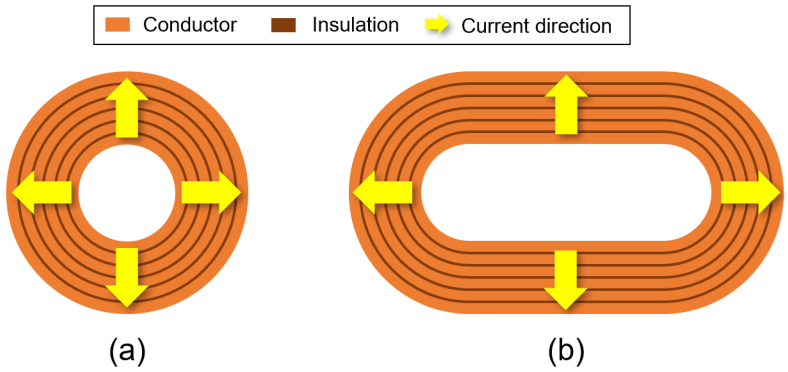

Figure 3.4: Contact resistance model of (a) NI HTS solenoid coil and (b) NI HTS racetrack coil.

is equal on all contacted surfaces), we can model this turn-to-turn current path with one characteristic resistance. The characteristic resistance can be obtained as a series sum of the contact resistance of each surface and is given by the following formula.

$$R_c = \sum_{j=1}^{N_t} \frac{R_{ct}}{(2\pi r_j + 2l)w_{cd}}. \tag{3.11}$$

R_{ct}, N_t, r_j, l, and w_{cd} mean contact resistivity, the number of turns, radius of each turn, straight section length, and width of turn, respectively. R_{ct} value has a different value for each coil, and it varies depending on the pressure between the surfaces by the winding tension, the surface condition of the conductor, the co-winding insulation material, and so on. It is known that the magnitude of contact resistivity can be controlled through various methods, but it is also known that it is still difficult to obtain an exact value of contact resistivity as users want. Even if the coil of the same specification is wound in the same way, the value of the detailed contact resistivity is different to some extent in many cases [79, 80]. The reported R_{ct} value is in a range from 2–5000 $\mu\Omega$·cm^2 [81]. In this study, just for the simulation, averaged R_{ct} value of 10 $\mu\Omega$·cm^2 was employed considering values obtained in the previous magnet project [82], and R_c is calculated to be 34.2 $\mu\Omega$.

In figure 3.3, R_{sc} is employed to represent the resistance of the superconductor in the circuit. In order to express superconductivity, the index resistance model is generally used for R_{sc}, and it is a model representing the relationship between current and resistance in superconductors. Superconductors show resistance close to zero below I_c, but when the operating current is above I_c, an exponentially increasing resistance appears, and this is mathematically modeled as the index resistance model [83].

$$R_{sc} = \frac{E_c}{I_\theta}\left(\frac{I_\theta}{I_c}\right)^n. \tag{3.12}$$

E_c is a critical electric field, and typically 1 μV/cm is used [84]. n is an index value, and depending on the value of n, the response of the superconductor appears differently as shown in figure 3.5. n-value of SuNAM's REBCO coated conductor is reported as 20–40 [85, 86]. In this paper, $n = 20$ is employed.

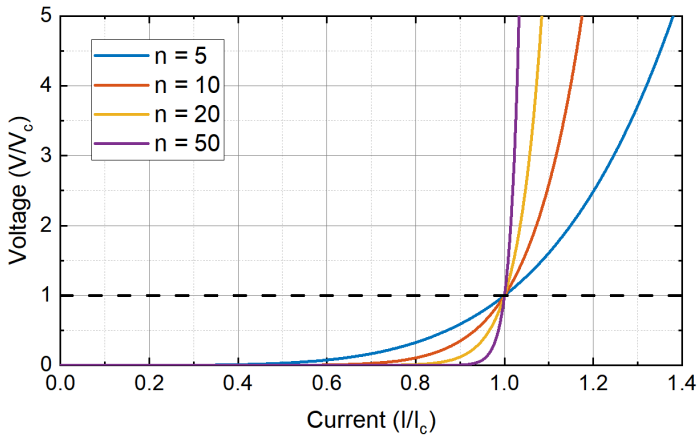

Figure 3.5: I-V characteristic curve of index resistance model.

Based on the circuit parameters described above, by applying Kirchhoff's law to the equivalent circuit, the following circuit equations can be derived.

$$I_{op} = I_\theta + I_r, \tag{3.13}$$

$$V_f = L\frac{dI_\theta}{dt} + R_{sc}I_\theta = R_c I_r. \tag{3.14}$$

Based on the given circuit equation and coil parameters, the simulation of charging and discharging of a given coil is performed and the result is shown in figure 3.6. The coil is charged to 66.2 A at a ramping rate of 0.05 A/s. The center magnetic field is calculated by $K \cdot I_\theta$.

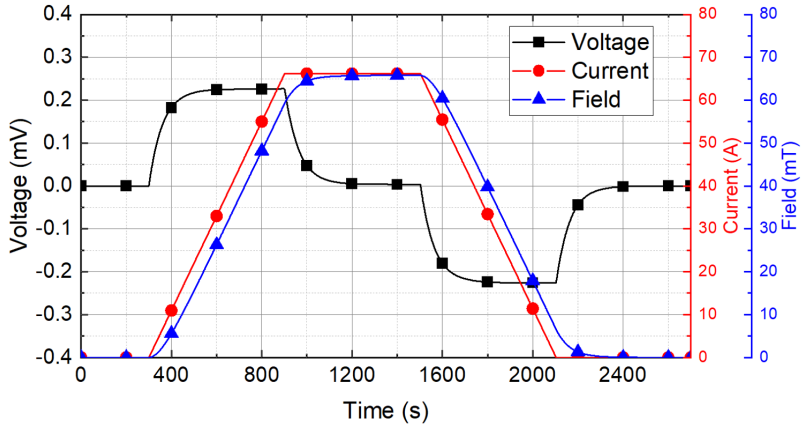

Figure 3.6: Charging-discharging simulation based on equivalent circuit model.

In the simulation, it can be seen that the magnetic field does not increase linearly with the increase of the current, but increase with a delay. This is a charging delay caused by turn-to-turn leak current, and this behavior is often referred to as "NI characteristics." This charging delay can be quantified using the coil's time constant ($\tau = L/R_c$). Roughly, L is proportional to (number of turns)^2 and R_c is proportional to (number of turns), so τ generally becomes larger as the number of turns increases. Also, the turn-to-turn leak current in the coil causes Joule heating, which is called turn-to-turn loss, and this turn-to-turn loss becomes an additional heat source for the superconductor coil. Further details on turn-to-turn loss will be discussed in the thermal analysis section.

3.3 The First Non-linear Analysis Models for NI HTS Motor

In the case of NI HTS motors, we need to consider NI characteristics that have not been considered before in steady-state operation as well as transient operation. As can be seen from the previous sections, the analysis technique of the NI HTS coil to interpret its NI characteristics at the coil level is well established. This is also the case for electromagnetic analysis of motors using conventional insulated coils. In this section, new analysis techniques for NI HTS motor are proposed by combining analysis techniques based on established analysis techniques. Analysis methods based on the equivalent circuit for transient analysis, which are the first non-linear analysis models for NI HTS motor were proposed. In addition, the FEM analysis model for NI HTS motor analysis, which grafted the principle of the proposed equivalent circuit model, was also presented.

3.3.1 Equivalent Circuit Model of Synchronous Motor with NI HTS Field Winding

When analyzing the operation of a motor, an analysis based on the equivalent circuit model has been widely used [8, 9, 87]. In the case of a partial superconducting motor using an insulated superconductor field coil, a conventional equivalent circuit of a wound-field synchronous motor (WFSM) could be applied. However, in the case of NI HTS motors, a new equivalent circuit model considering the turn-to-turn leak current in the NI HTS coil is required. In particular, since this turn-to-turn leak current generally occurs in transient operations, it is necessary to analyze how the motor characteristics change from the turn-to-turn leak in various transient operations.

Figure 3.7 shows the suggested equivalent circuit analysis model of synchronous motors with NI HTS field winding [18]. This model is based on two well-known circuit models previously suggested: 1) dq-axis equivalent circuit for synchronous motor, and 2) lumped parameter circuit model of NI HTS coil explained in section 3.2.

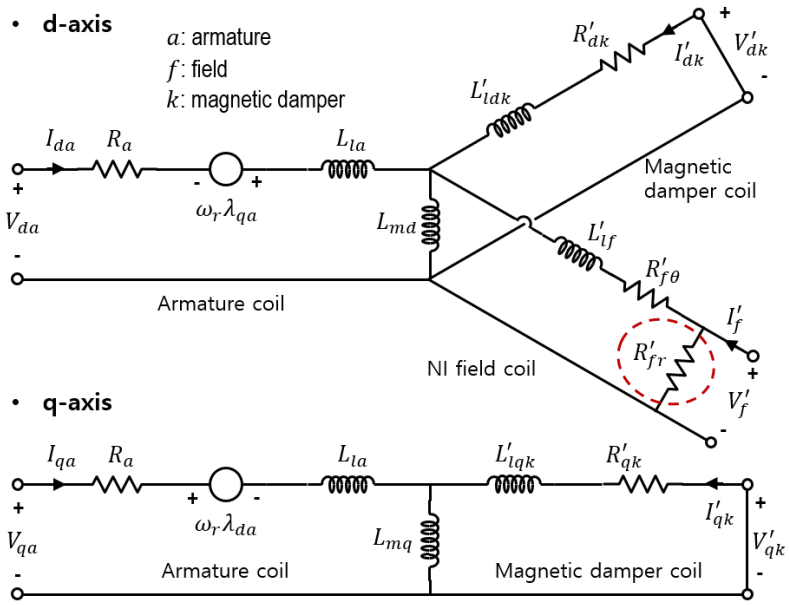

Figure 3.7: Equivalent circuit model of synchronous motor with NI HTS field winding.

The lumped circuit model is combined with an existing equivalent circuit model for a conventional insulated synchronous machine in figure 3.7, where the subscripts of a, f, and k represent the armature, field, and magnetic damper coils, respectively. These coils share a common mutual inductance (L_m) and have their own leakage inductances (L_l), and coil resistances (R). ω and λ_a are rotating speed and flux linkage of armature winding, respectively. By applying Kirchhoff's law to the proposed equivalent circuit model, the following circuit equations can be derived.

$$V_{da} = R_a I_{da} - \omega_r \lambda_{qa} + \frac{d}{dt}\left[L_{la} I_{da} + L_{md}\left(I_{da} + I'_{dk} + I'_{f\theta}\right)\right], \tag{3.15}$$

$$V_{qa} = R_a I_{qa} + \omega_r \lambda_{da} + \frac{d}{dt}\left[L_{la} I_{qa} + L_{mq}\left(I_{qa} + I'_{qk}\right)\right], \tag{3.16}$$

$$V'_f = R'_{f\theta} I'_{f\theta} + \frac{d}{dt}\left[L'_{lf} I'_{f\theta} + L_{md}\left(I_{da} + I'_{dk} + I'_{f\theta}\right)\right], \tag{3.17}$$

$$V'_{dk} = R'_{dk} I'_{dk} + \frac{d}{dt}\left[L'_{ldk} I'_{dk} + L_{md}\left(I_{da} + I'_{dk} + I'_{f\theta}\right)\right], \tag{3.18}$$

$$V'_{qk} = R'_{qk} I'_{qk} + \frac{d}{dt}\left[L'_{lqk} I'_{qk} + L_{mq}\left(I_{qa} + I'_{qk}\right)\right], \tag{3.19}$$

$$V'_f = R'_{fr} I'_{fr}, \tag{3.20}$$

$$I'_f = I'_{fr} + I'_{f\theta}. \tag{3.21}$$

In equations, the apostrophe ($'$) means that the parameter is converted to the armature side considering the turn ratio. Equations (3.15)–(3.19) are the same as the circuit equations derived from the dq-axis equivalent circuit model of the conventional insulated motor. In figure 3.7, the resistive current path marked with a red circle is added, adding equations (3.20) and (3.21), which describe NI behavior in the motor.

In addition to the circuit equations above for transient operation simulation, the following equations were used to represent the motor's mechanical rotating motion [87].

$$T_e = \frac{3p}{4}\left[L_{md} I'_{f\theta} I_{qa} + (L_{md} - L_{mq}) I_{qa} I_{da} + (L_{md} I'_{dk} I_{qa} - L_{mq} I'_{qk} I_{da})\right], \tag{3.22}$$

$$T_e = J_r \frac{d\omega_r}{dt} + B\omega_r + T_L. \tag{3.23}$$

In the above formulas, T_e, p, J_r, B, and T_L mean output torque, the number of poles, rotational inertia, friction coefficient, and load torque, respectively.

In this paper, based on the suggested analysis model, the characteristic analysis of the designed motor and the analysis of the experimental results were performed in section 4.1.3 and section 6.4.2, respectively.

3.3.2 Finite Element Method Analysis Model Combined with Lumped Parameter Circuit Model

In actual motor operation, due to field harmonics generated by nonlinear components like iron teeth, a potential turn-to-turn leak current may occur. Therefore, analysis of potential characteristic change due to turn-to-turn leak current from nonlinear components is required [88]. Only with the equivalent circuit model proposed in the previous section, it is difficult to consider the detailed effect of nonlinear components like iron.

Therefore, in this study, for the detailed analysis of the effect of NI behavior, the new FEM analysis model, which has a principle similar to the previous equivalent circuit model, was additionally proposed and used.

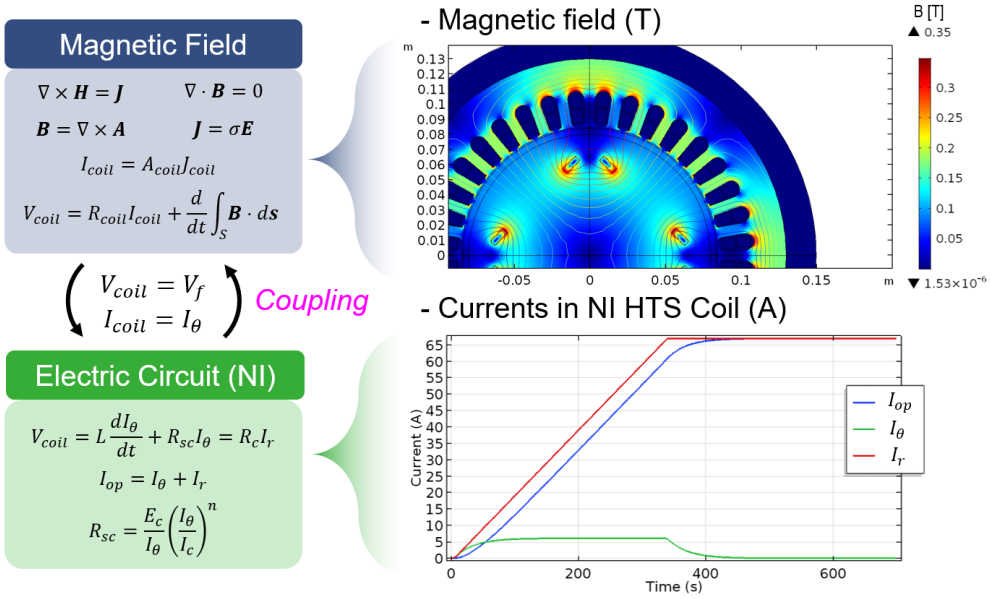

Figure 3.8: Concept of 2D FEM analysis of NI HTS synchronous motor.

Figure 3.8 shows the concept of 2D FEM analysis of synchronous motor with NI HTS field winding. The basic concept of analysis is combining a lumped equivalent circuit of NI HTS coil with a conventional FEM magnetic field analysis module. Therefore, the governing equations of the magnetic field analysis (equation (3.5)–(3.8)) and the circuit equations of the NI HTS coil (equation (3.12)–(3.14)) introduced in section 2.2.2 are combined in the FEM module. Also, the current and voltage in the field and stator coil are calculated through equations (3.24) and (3.25).

$$I_{coil} = A_{coil} J_{coil}, \tag{3.24}$$

$$V_{coil} = R_{coil} I_{coil} + \frac{d}{dt} \int_S \boldsymbol{B} \cdot d\boldsymbol{s}. \tag{3.25}$$

In equation (3.25), $\frac{d}{dt} \int_S \boldsymbol{B} \cdot d\boldsymbol{s}$ represents the electromotive force by the flux linkage change in the coil. I_{coil}, V_{coil}, R_{coil}, and J_{coil} are the current, voltage, resistance,

and current density of the FEM coil, and in the NI HTS coil, I_{coil}, V_{coil}, and R_{coil} correspond to I_θ, V_f, and R_{sc} in the formula (3.12)–(3.14), respectively.

In the analysis based on the suggested model, the governing equations and the circuit equations are simultaneously satisfied. Through this, it is possible to analyze the magnitude of the turn-to-turn leak current (I_r) and its effect on motor characteristics.

In this paper, the characteristic analysis of the designed motor and the analysis of the experimental results were performed in section 4.1.3 and section 6.3.2, respectively.

Chapter 4

DESIGN OF TEST MACHINE AND EXPERIMENTAL SYSTEM FOR APPLICABILITY TEST OF NI HTS FIELD WINDING

This chapter describes the design of the test machine and experimental system for the experimental study on the applicability of the NI HTS coil to superconducting motors. Since this study aims to investigate the applicability of the NI technique to a superconducting motor, goal-oriented design directions that can effectively achieve the purpose of the experiment were considered rather than aiming for the high-end performance of the tested motor. Based on the analysis models proposed in the previous chapter, the expected results are presented in the test of the designed test machine. In addition, based on the test machine design, a rotor structure and a cooling chamber were designed. The analyses related to the mechanical and thermal properties considered in the design processes are also described.

4.1 Electromagnetic Design of Test Machine for Experiment

Based on the suggested analysis models of NI HTS motor in chapter 3, in this section, the test system to evaluate NI applicability was designed. The overall design directions

were established first, and the required electromagnetic design was performed under the design assumptions.

4.1.1 Purpose of Test System and Overall Design Directions

Review on Purpose of the Test System

The operating conditions of NI HTS field winding in the motor would be different from the conventional stationary NI HTS magnets, For example, the variation of characteristic parameters according to rotation and interaction with the external armature coil needs to be additionally considered. Since there has not been a detailed study on how the NI HTS coil responds under these operating conditions, there is a concern that the NI HTS motor may not operate as designed. Therefore, for a direct investigation of applicability of the NI HTS coil to superconducting motors, an experimental study on how the NI HTS coil reacts in motor operation is needed. In addition, it is necessary to investigate whether the proposed analysis models can sufficiently explain the characteristics of the experimental results.

Design Directions of Test Motor and Test System

The best way to investigate the applicability of the NI technique to HTS motor would be to develop a high-performance superconducting motor incorporating NI technology and derive its characteristics through an actual operation. However, developing such an NI HTS motor in the current situation where NI applicability is not judged has uncertainty in terms of machine performance, and a lot of costs are incurred for development. Therefore, in this test, a simple motor with NI HTS field winding was developed, but even if some machine performance is sacrificed, a test system capable of cost-saving and reliable test of the NI response was developed. The test motor and experiment system were designed based on the following three design directions: 1) use of a commercial stator, 2) air-cored type rotor, and 3) liquid nitrogen cooling.

- **Use of a commercial stator:** for the convenience of fabrication and cost reduction, it was decided to use the commercial motor's stator as it is. Accordingly, the motor topology, the rotating NI HTS field coil was placed inside, and the 3-phase copper armature coil was placed outside for the test machine design.
- **Air-cored type rotor:** for straightforward characteristic analysis on NI HTS field coil, the rotor was designed to have no ferromagnetic materials in this study. Therefore, the superconducting rotor was designed as an air-cored type, which is often used in superconducting motor design, not an iron-cored type.
- **Liquid nitrogen cooling:** cooling system of the superconducting motor is one of the major factors causing the complexity of the design and manufacture of the superconducting motor. In this study, in order to simplify the cooling system, liquid nitrogen (LN_2) was used to cool the NI HTS field coil, and accordingly, the operating temperature was determined to be 77 K. Also, the cooling system was designed to be easy to repeat test without an additional pump or circulation system.

Expected Limitation of Test Motor and Test System

Owing to the above design approaches, it can be effective for achieving the primary goal of this study, the investigation of NI applicability, while the test system in this study does have limitations including:

- **Relatively low performance of the test motor:** in this system, the operating temperature is set to 77 K with LN_2, so the critical current of the field coil is relatively low (figure 2.4 (a)). It leads to a low air-gap magnetic field. Also, for thermal insulation of the LN_2 chamber, a large air-gap is required and it is another factor for low performance.
- **Limited operation time:** in this system, a pump or cryogen circulation system was not employed, instead, dunk cooling was used for quick and easy cool-

down and warm-up of the rotor (will be introduced in detail in section 4.2.2). So, operation time is limited according to the thermal loss of the system, even though repeated experiments can be easily performed through LN_2 refill.

- **Additional effect from the use of commercial product:** a commercial slip-ring is used to supply the operating current of the field coil and to detect the signals of the rotor in this system. The commercial slip-ring used has its own maximum speed rating, so possible rotating speed is limited.

4.1.2 Electromagnetic Design Based on Parameter Sweep

With the determined design directions, it is necessary to design a superconducting rotor with an NI HTS field winding to be manufactured, which is the subject of analysis in the experiment. This section describes the electromagnetic design for this.

Design Assumptions for the Test Machine

Table 4.1: Design Assumptions for the Test Machine

Category	Assumptions
Topology	Synchronous motor with Air-cored rotor
REBCO coated conductor	SuNAM's REBCO CC (4.1 mm×0.14 mm)
Armature coil current	$I_a =$ (rated value of stator winding)
Field coil current	$I_f = 0.7 \times I_c$
Axial length of racetrack	$l =$ (effective length of stator)
Temperature of superconductor	$T_{op} = 77$ [K]
Magnetic airgap	$d_{air} = 15$ [mm]
Target rotating speed	$\omega_r = 300$ [rpm]

The following assumptions were made for the electromagnetic design of the NI HTS motor. First, for the stator and superconductor wire of the machine, the stator

of the commercial motor and SuNAM's 4.1 mm REBCO coated conductor were used each. The target operating current of the armature coil (I_a) was determined to be the rated value as that of the given stator. The operating current (I_{op}) of the NI HTS field coil was determined to be 70% of the estimated critical current (I_c) considering the current margin. Considering LN_2 cooling, the operating temperature (T_{op}) is set to 77 K. In addition, a sufficient magnetic airgap (d_{air}) of 15 mm was determined to install the structure for cooling the rotating NI HTS field coil rotor. Finally, the target rotating speed (ω_r) was determined to be 300 rpm to avoid overflowing LN_2 by centrifugal force and to prevent signal disorder of the commercial slip-ring.

For the commercial stator to be used, a stator of 15 kW class induction motor which has three-phase, four-pole, and 380 V_{rms} rated voltage was selected to be used. The outer and inner diameters of the stator are 260 mm and 170 mm, respectively, and the effective axial length is 180 mm. The number of slots is 36. The winding pitch of the winding is 7, and it is composed of 2 layers per slot. The total number of parallel circuits is 2. The number of turns per layer is 14, and the winding end connection is a wye connection. Table 4.2 summarizes the parameters of the stator.

Table 4.2: Parameters of Non-superconducting Stator

Parameters	**Values**	**Parameters**	**Values**
Rated current	28.9 A_{rms}	Slot number	36
Current density	2.74 A/mm^2	Layer per slot	2
Phase	3	Turns per layer	14
Pole	4	Parallel circuit	2
Stator OD	260 mm	Winding pitch	7
Stator ID	170 mm	Connection	Wye
Axial length	180 mm	Core material	50PN470

Detailed Design Process of Parameter Sweep

When specifications of a stator are given, and since a designing motor has an air-cored rotor shape, the output torque and NI charging delay can be predicted if the geometry of the field coil is given. The geometry of the racetrack is determined by the specification of the conductor (w_{cd} and t_{cd}), number of turns (N_t), number of stacks (N_s), inner radius (r_i), and length of the straight section (l). Considering the design assumptions, the design range of the possible racetrack coil designs is limited, so all combinations of possible field coil designs are investigated through a parameter sweep and the design to be fabricated was selected between them. The overall flowchart of the parameter sweep is shown in figure 4.1.

The parameter sweep process of this study is as follows in the order of progress.

- **Step 1:** first, the design parameters to perform the parameter sweep and their ranges are set. When determining the range, the critical bending strain, the inner diameter of the stator, and the determined air-gap are considered. With design parameters and their ranges, design parameter sets for parameter sweep are generated.

- **Step 2:** FEM model is created using the given design parameter set.

- **Step 3:** the design is reviewed whether the geometric constraints are satisfied, and if not satisfied, the design is dumped.

- **Step 4:** I_{op} of the field coil is determined. The calculation of I_c was performed in an iterative way based on the load-line technique introduced in section 3.1.2, and I_{op} is determined so that the current margin was $>30\%$.

- **Step 5:** based on the determined I_{op}, the motor performance (airgap field and out torque) and parameters relevant to NI characteristics (characteristic resistance and time constant) are estimated.

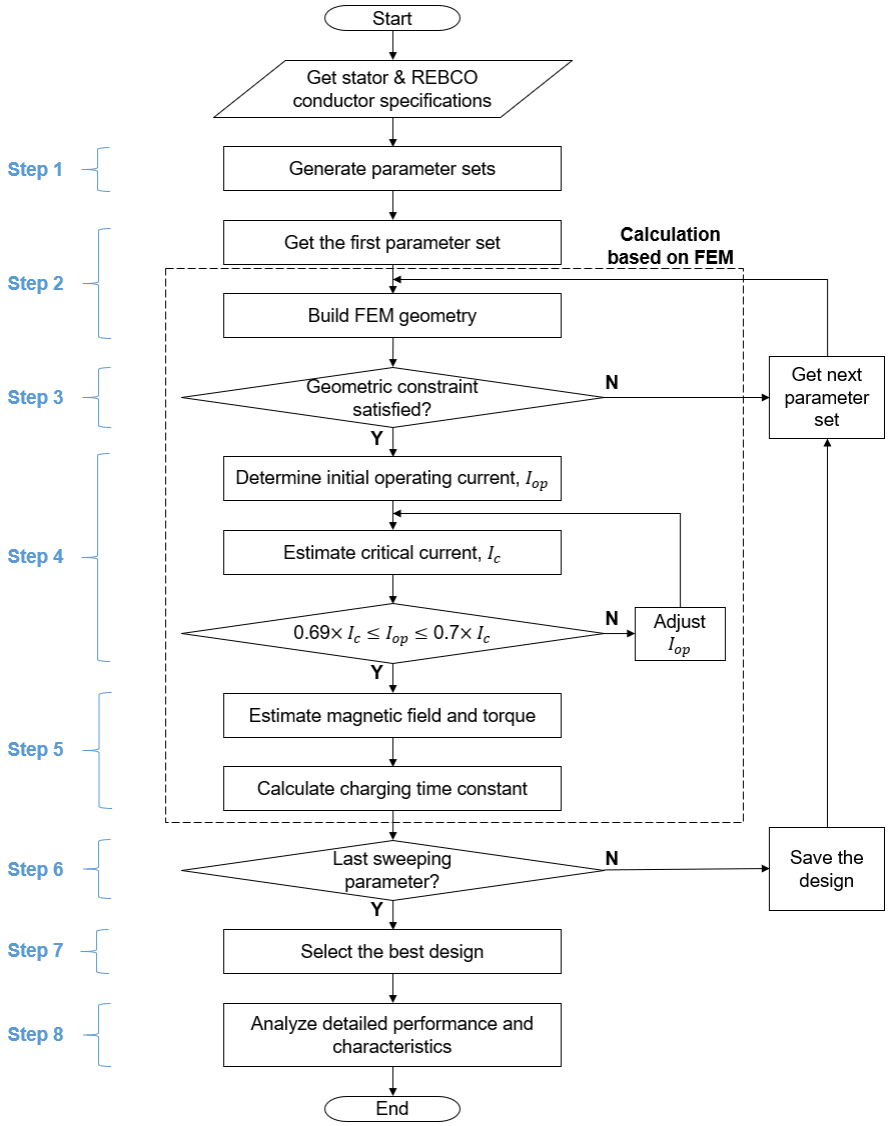

Figure 4.1: Design flowchart of the test motor.

- **Step 6:** calculated data is saved. *Step 2* to *step 5* are repeated with the next design parameter set. This process is repeated until the calculation with the last sweeping parameter set.
- **Step 7:** among the design options obtained through parameter sweep, the design that best met the design purpose is selected.
- **Step 8:** detailed analyses of the selected design are performed.

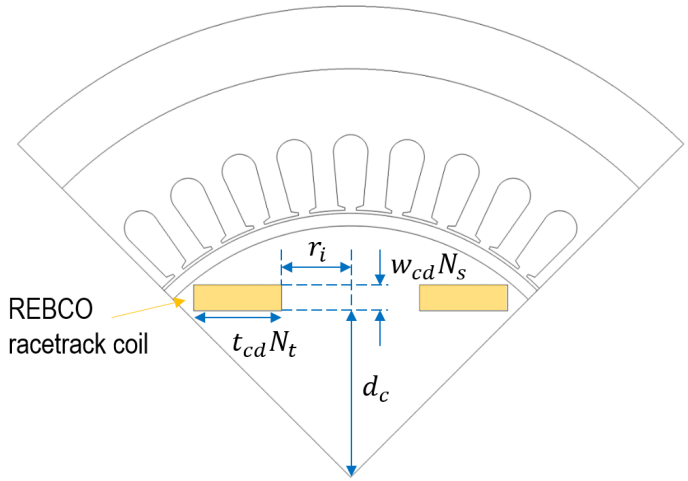

Figure 4.2: Design parameters for parameter sweep represented in quarter 2D drawing.

In *step 1*, first, design parameters to perform parameter sweep were selected. When the width and thickness of the REBCO tape are given, considering the shape of a racetrack coil, the whole geometry of the racetrack can be completely determined using the following four parameters shown in figure 4.2: 1) inner radius (r_i), 2) the number of turns (N_t), 3) the number of stacks (N_s), and 4) distance from rotating center (d_c). Also, because the output power is proportional to flux linkage between field and armature coil, an additional assumption is added that the edge of the field coil is located as close as possible to the stator within the given area for the rotor. Then, when 1)–3) is decided, 4) is automatically obtained. Therefore, 1) inner radius, 2) turn number, and

3) stack number were finally selected as design parameters. For the sweeping ranges, the minimum value of the inner radius was set to 14 mm to prevent I_c reduction due to bending strain (will be introduced in section 4.2.1). Also, due to the limited rotor area, the maximum value of the turn number was automatically set to <200. In addition, the stack number is limited to a maximum of 2 for ease of manufacturing. The sweeping ranges determined are summarized in table 4.3.

Table 4.3: Sweeping Range of Each Design Parameter

Parameters	**Min.**	**Max.**	**Interval**
Inner radius, r_i [mm]	14	48	2
Number of turns, N_t	10	200	5
Number of stacks, N_s	1	2	1

In *step 2*, the geometry of the FEM model was built based on the design parameters in the sweeping range. If the edge of the designed coil exceeds the area set for the rotor, the design is dumped and moves on to the next parameter set (*step 3*). Using the FEM model, the operating current of the field coil (I_{op}) was determined in *step 4*. The critical current (I_c) of a given racetrack coil was estimated based on the load-line technique introduced in section 3.1.2, and for this purpose, an iterative calculation was performed by changing I_{op}. When I_c is estimated, I_{op} is determined to be 70% of I_c.

In *step 5*, the basic performance and parameters relevant to NI characteristics were calculated based on the given FEM model. The magnetic field distribution and radial direction air-gap magnetic field (B_a) were calculated, and the torque (T_e) generated in effective length was estimated using the equation (4.1) [2]. In the design process, an additional torque generation due to end-effect was neglected.

$$T_e = \frac{1}{\sqrt{2}} A_l \cdot 2\pi r_a \cdot l \cdot r_a \cdot B_a = K_a \cdot B_a. \tag{4.1}$$

A_l means the linear current density of the armature coil, and r_a means the radius of the air-gap region from the center. Since A_l, r_a, and l are given as constants here, the

equation (4.1) can be expressed with a constant K_a, thus T_e is proportional to B_a. In addition, for the estimation of NI characteristics, the methods introduced in section 3.2 were employed. The inductance of the field coil (L) was calculated using the energy method, and the characteristic resistance (R_c) was calculated using equation (3.11). With L and R_c, the time constant (τ) of the designed coil was estimated.

As described in figure 4.1, *step 2* to *step 5* are repeated for all design parameter sets (*step 6*). In *step 7*, the design options derived in the parameter sweep were compared. Comparisons were made based on the following two criteria:

- **Criterion 1:** considering the economic efficiency, a design with a large output torque (T_e) compared to the input amount of REBCO coated conductor (l_{REBCO}) was selected.
- **Criterion 2:** since one of the key purposes of this study is to analyze NI response in motor operation, a design showing large NI characteristics, that is, a design with a relatively large charging time constant was selected. It needs to be noted that a large charging time constant cannot be said to be good for motor performance. However, in this study, this criterion was established in terms of NI applicability investigation.

Expressing these as an objective function ($\boldsymbol{F}(\boldsymbol{x})$), it is given as equation (4.2).

$$\begin{aligned} \text{Max.} \quad & \boldsymbol{F}(\boldsymbol{x}) = (f_1(\boldsymbol{x}), f_2(\boldsymbol{x})), \\ \text{subject to} \quad & f_1(\boldsymbol{x}) = T_e / l_{REBCO}, \\ & f_2(\boldsymbol{x}) = \tau, \\ & \boldsymbol{x} = (r_i, N_t, N_s). \end{aligned} \tag{4.2}$$

Figure 4.3 shows the parameter sweep result as a scattering plot for comparison of objective function values (f_1 and f_2). x-axis is time constant (τ), and y-axis is torque per REBCO consumption (T_e/l_{REBCO}). All the obtained designs through parameter sweep are represented as blue circles. Potential design candidates having high values

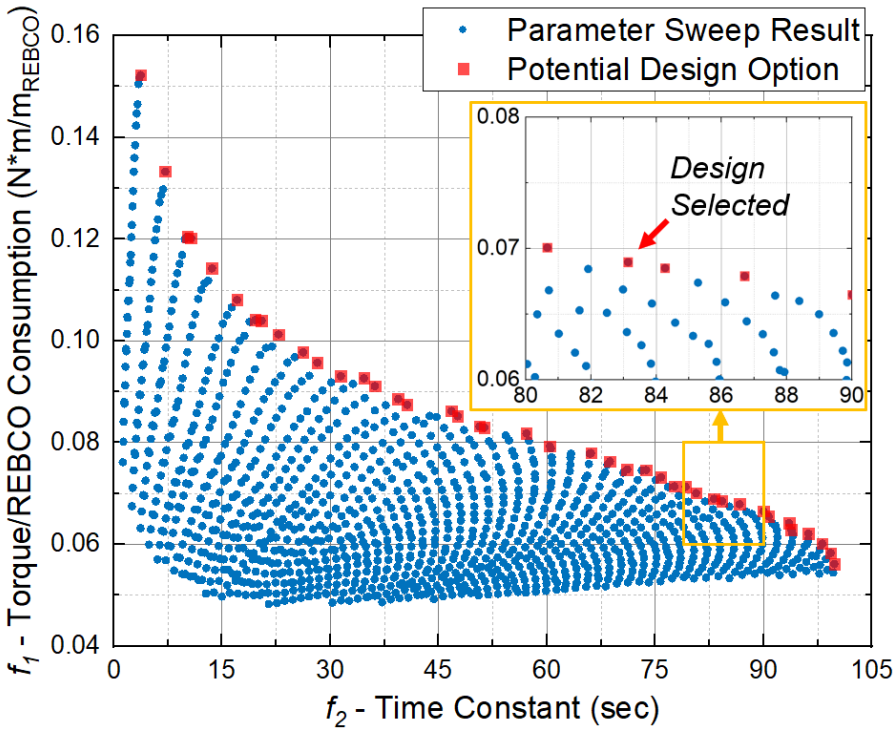

Figure 4.3: Scatter plot of the parameter sweep results.

of f_1 and f_2 at the same time are marked with a red square. The design marked with the red arrow (r_i= 28 mm, N_t= 80, N_s= 1, and d_c= 49 mm) was finally selected in consideration of the amount of REBCO coated conductor in stock.

4.1.3 Operation Characteristics Analysis of Designed Test Machine

For the designed test motor, its characteristics were analyzed and derived in detail based on the proposed analysis models. Considering the tests to be actually performed using the test system to be built, the following analyzes were performed.

- **Analysis on interaction with stator winding:** simulations were performed on the response of the NI HTS field winding when a direct magnetic axis (d-axis) current (I_{da}) and a quadrature magnetic axis (q-axis) current (I_{qa}) were applied

to the stator winding, respectively. Through this, the effect of the stator current on the NI HTS field winding was analyzed.

- **Steady-state operation analysis:** back electromotive force (EMF), torque, and NI response generated when the test motor rotated at a constant speed were analyzed. Through this, the effect of inductance variation on the NI HTS field winding in the rotation that might be caused by iron teeth or others was analyzed.

- **Transient operation analysis:** through a simulation coupled with a simple PI controller, the phenomena appearing in the NI HTS field winding during transient motor operation such as external load fluctuations were comprehensively analyzed.

In order to compare the performance of the NI HTS motor (NI) and insulated counterpart (INS) under ideal conditions, each analysis was performed for NI and INS, and potential differences were analyzed.

Analysis on Interaction with Stator Winding

First, in order to analyze the response of the NI HTS motor by the stator winding current, the response that appears when I_{da} or I_{qa} is applied as a step function, respectively, was simulated under stationary condition (locked motor without rotation). For simulation, the FEM model proposed in section 3.3.2 was used, and the voltage, current of the NI HTS field winding, and generated torque were derived.

Figure 4.4 shows the magnetic field distribution in each simulated condition in this section. Figure 4.4 (a) shows the saturated magnetic field distribution after only the NI HTS field winding is excited before I_{da} or I_{qa} is applied. Figure 4.4 (b) and (c) show the saturated magnetic field distribution after applying I_{da} and I_{qa}, respectively. Figure 4.4 (b) and (c) correspond to the situations shown in figure 4.5 and figure 4.6. As can be seen from the magnetic field distributions, since I_{da} generates a magnetic field in the same direction as the magnetic field generated by I_f, the overall magnetic field

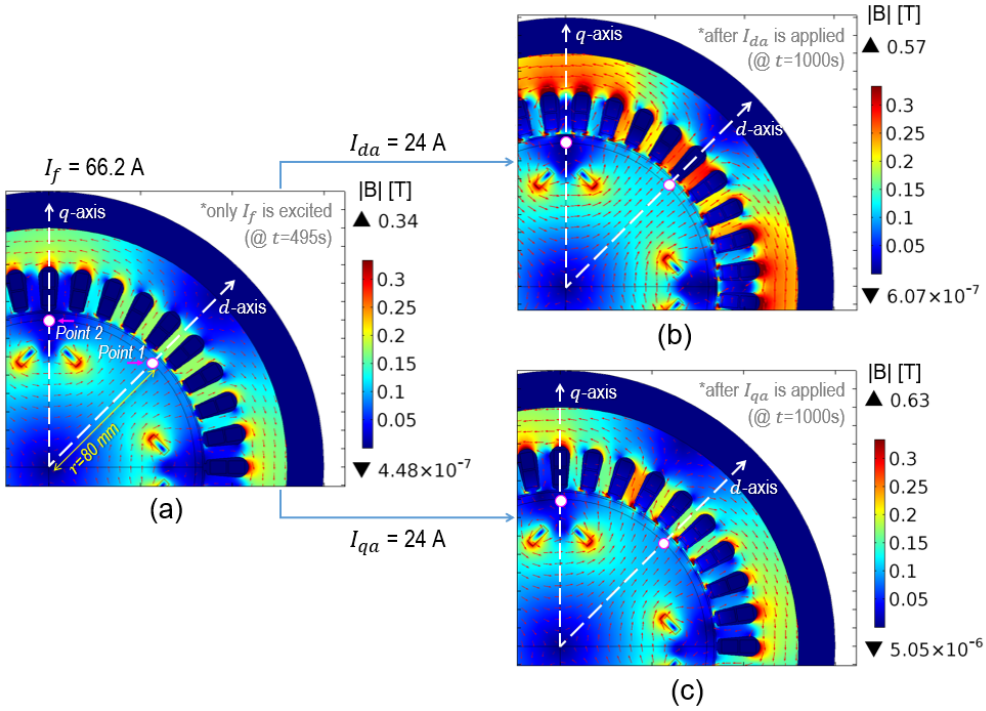

Figure 4.4: Magnetic field distribution of simulated situations in FEM. (a) Before I_{da} or I_{qa} is applied, (b) After I_{da} is applied, (c) After I_{qa} is applied.

distribution tends to be strengthened. While I_{qa} creates a magnetic field in the quadrature direction of the magnetic field generated by I_f, the direction of the magnetic field tends to slightly change to the q-axis in this case. In each simulation situation, when I_{da} or I_{qa} is given as a step function, in order to investigate the magnetic field distribution over time, the magnitude of the magnetic field at point 1 (at r=80 mm on d-axis) and point 2 (at r=80 mm on q-axis) over time was derived and additionally shown in figure 4.5 and figure 4.6.

Figure 4.5 shows simulation results when NI HTS field winding is charged to 66.2 A, applying 24 A of I_{da} as a step function while maintaining I_{qa} at 0 (figure 4.5 (a)). In figure 4.5 (b)–(f), the blue solid line represents the response of the motor with the NI HTS field winding, and the orange dashed line represents the response of the insulated

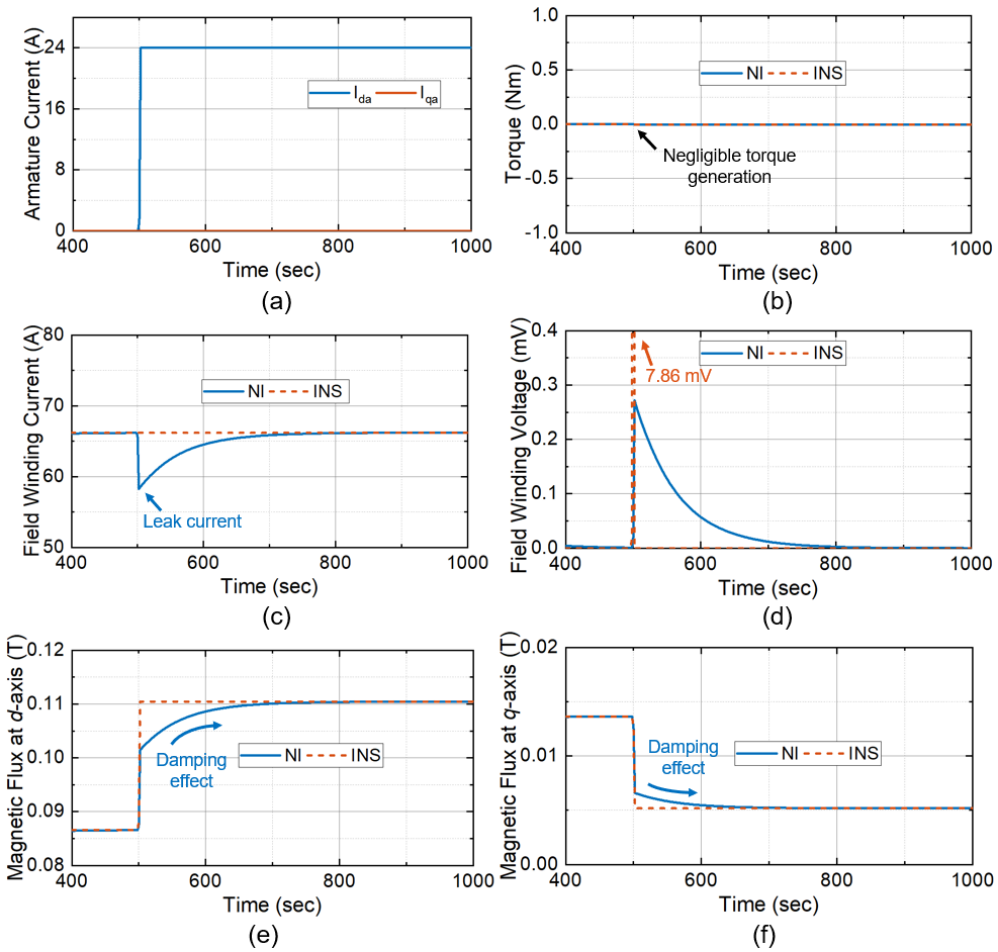

Figure 4.5: Analysis of NI HTS motor response on I_{da} current. (a) Applied I_{da} and I_{qa}, (b) Torque, (c) Field winding current, (d) Field winding voltage, (e) Magnetic field at d-axis, and (f) Magnetic field at q-axis.

counterpart (INS). Because a d-axis component of the stator current is a component contributing to the magnetic field by the rotor, it can be seen that the magnitude of the magnetic field of the d-axis increases (figure 4.5 (e)). However, in the case of NI, it was confirmed that the magnetic field did not immediately increase as much as the applied magnetic field due to the "flux conservation" characteristics to maintain the existing magnetic field, that is, a damping effect that magnetic field increased slowly according to the time constant appeared. In the case of the current of the field winding, in the case of INS, it maintained 66.2 A regardless of I_{da}, but in the case of NI, as the rotor magnetic field instantaneously increased, the current decreased, and the current was restored at the rate of the charging time constant (figure 4.5 (c)). it was confirmed in both NI and INS that induced voltage was identified in the field winding due to an instantaneous external magnetic field change (figure 4.5 (d)). However, compared with the INS, where a maximum of 7.86 mV appeared momentarily and disappeared, in the case of NI, the maximum voltage of $<$0.3 mV appeared, and it was found that it gradually decreased at the rate of the charging time constant. On the other hand, since the magnetic field by I_{da} does not contribute to the torque generation, no torque appears (figure 4.5 (b)).

Figure 4.6 shows the simulation results when I_{qa} is applied with 24 A instead of I_{da}, with the same conditions for others. Because I_{qa} is a component that contributes to torque generation of stator current, in the case of the d-axis magnetic field magnitude, there is relatively little change in figure 4.6 (e) compared to the previous figure 4.5 (e). In the case of the q-axis magnetic field, it increased with I_{qa} (figure 4.6 (f)). In particular, unlike the case where I_{da} was applied, it was confirmed that the damping effect such as flux conservation did not appear. This characteristic can be seen more clearly with the voltage and current of the field winding. There are no changes in voltage and current of the field winding for both NI and INS (figure 4.6 (c) and (d)). In the case of torque, it was found that the torque was generated in proportion to the I_{qa} applied by both NI and INS, and there was no difference in response time between

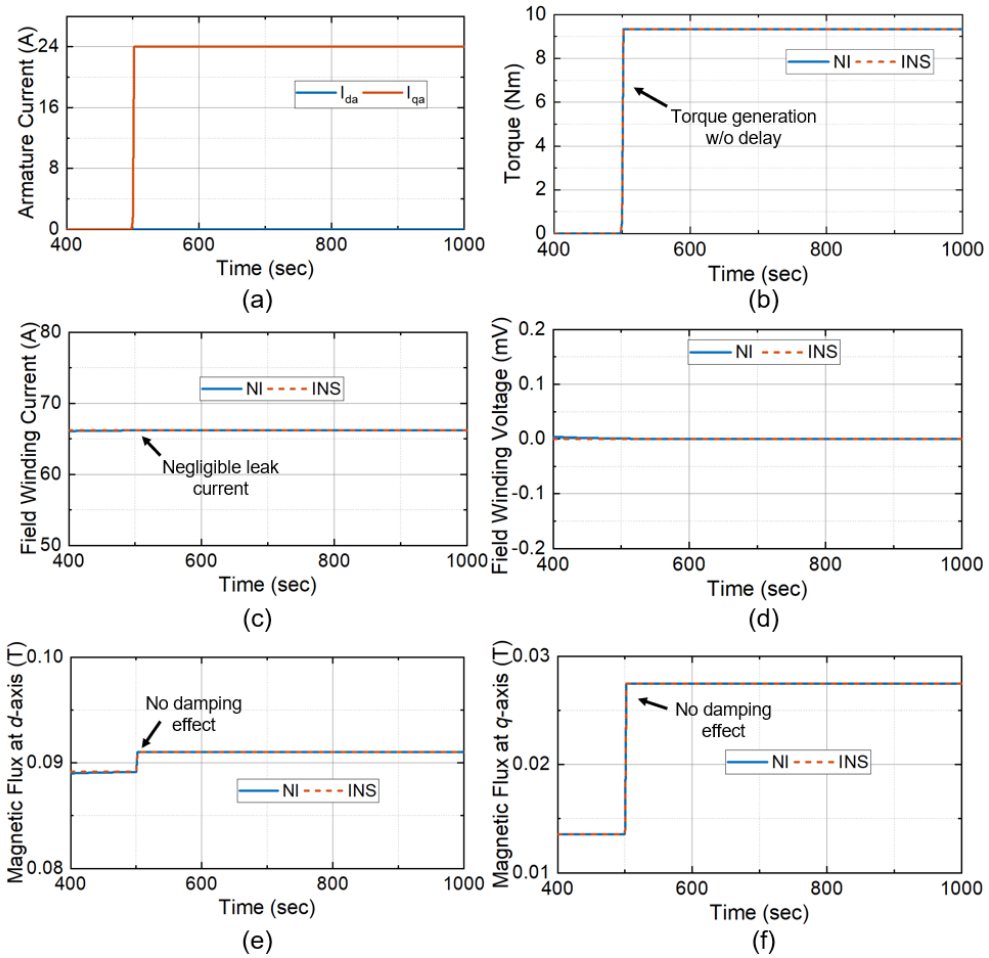

Figure 4.6: Analysis of NI HTS motor response on I_{qa} current. (a) Applied I_{da} and I_{qa}, (b) Torque, (c) Field winding current, (d) Field winding voltage, (e) Magnetic field at d-axis, and (f) Magnetic field at q-axis.

them (figure 4.6 (b)). That is, even if NI HTS field winding was applied, there was no damping effect on torque.

Through the above two simulations, it was expected that there would be no major problem in controlling the torque of the motor by applying q-axis current in the stator winding. However, when the d-axis current was applied, it was confirmed that the leak current occurred in the NI HTS field winding just like the situation in which an external magnetic field was applied to the previous NI HTS magnet. Since this leak current disappears to the rate of the charging time constant, it was expected that NI behavior must be considered when controlling I_{da} for additional control of magnetic flux.

Steady-state Operation Analysis

The steady-state performance simulation of the test motor was performed based on the proposed FEM analysis model in section 3.3.2. Back EMF simulation and load analysis were performed respectively, and the magnetic field, output, and NI response at that time were analyzed.

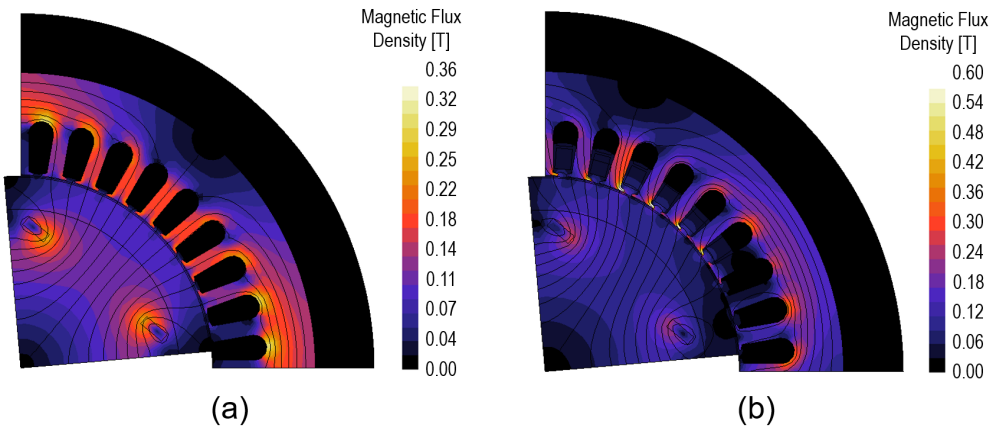

Figure 4.7: Magnetic field analysis results of the test motor. (a) Back EMF analysis result, (b) Load analysis result.

Figure 4.7 (a) shows the magnetic flux density distribution of the test motor when only NI HTS field winding is excited with I_f = 66.2 A, while figure 4.7 (b) when the rated armature current is also supplied (I_a = 28.9 A_{rms}). The maximum magnetic flux density is lower than the saturation level of the 50PN470 core (∼1.4 T) of the stator due to the air-cored structure of the rotor and the large magnetic air-gap (15 mm) for the cryogenic chamber installation. It implies that the leak current and characteristic change of the NI HTS coil due to iron saturation would not be significant in this study.

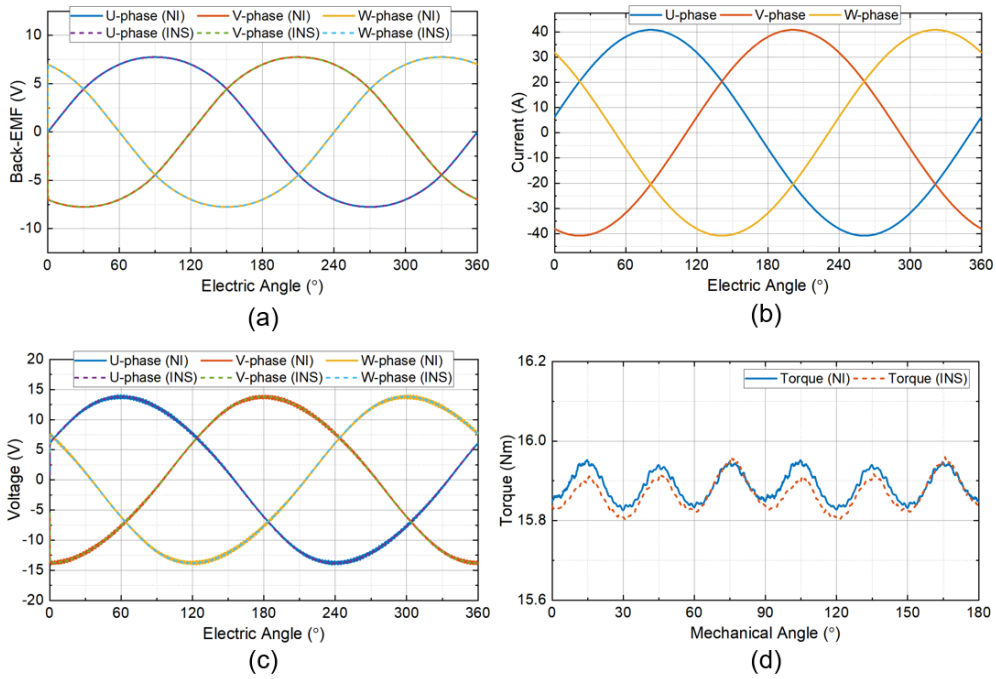

Figure 4.8: FEM analysis results in steady-state operation. (a) Back EMF in no-load simulation, (b) Current, (c) Phase voltage, and (d) Torque in load simulation.

Next, each of the output values was derived in no-load conditions (I_a = 0, ω_r = 300 rpm) and load conditions (I_a = 28.9 A_{rms}, ω_r = 300 rpm), respectively. Figure 4.8 (a) shows the phase voltage of the stator in the no-load simulation. Figure 4.8 (b) presents the profile of the input current of load simulation, and (c) and (d) show the phase voltage of the stator and generated torque under load conditions. In each graph, the

solid blue line represents the simulation result of the test motor with NI characteristics considered, while the dashed orange line is the result of the insulated counterpart.

The back EMF of the NI HTS test motor under no-load conditions was 5.73 V_{rms}, and the difference with its insulated counterpart was 0.04%, which showed a negligible difference. THD was 4.40% and 4.38% for NI and INS, respectively. The phase voltage of the NI HTS motor under load conditions was 9.77 V_{rms} and shows a 0.09% difference from the INS case. The average torque under the load condition was calculated to be 15.9 Nm, and the difference with the INS was 0.12%. The torque ripple was 0.8%. Overall, it was expected that the difference in motor operation characteristics due to NI HTS field winding in steady-state was not significant in terms of the phase voltage and torque.

In order to directly confirm how much turn-to-turn leak current is generated in the NI HTS coil, the value of I_θ is shown in figure 4.9 under (a) no-load condition and (b) load condition. In the case of INS, I_θ maintains 66.2 A equal to the power supply current under both conditions. In the case of NI, a small leak current does exist. It is because due to nonlinear components like iron teeth and the arrangement of each winding, there is inductance change during rotation ($<$0.120 μH in no-load condition, $<$0.460 μH in load condition in terms of self-inductance of field coil), and it leads to a leak current in NI HTS coil. In the case of the insulated coil, the current remains the same even if there is a change in inductance, but in the case of the NI coil, it was confirmed that the change in inductance becomes the source of the leak current. However, the magnitude of the leak current was found to be rather insignificant in simulation. The peak-to-peak current difference of I_θ under no-load conditions was 4.83 mA, and 17.9 mA under no-load conditions.

In this study, no iron core was used in the rotor and a large air-gap of 15 mm was set. This could be the main reason for fewer NI characteristics in the steady-state simulation. Actually, the air-cored structure and large air-gap are often considered in the actual design and manufacture of partial superconducting motors, therefore, it is

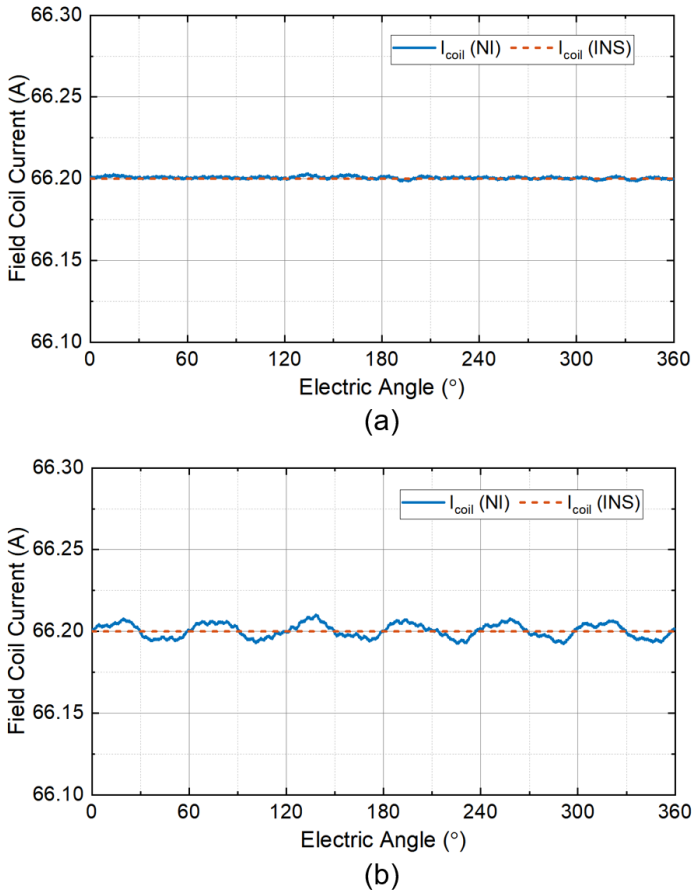

Figure 4.9: Analysis of field winding current in steady-state operation. (a) No-load condition, (b) Load condition.

considered that NI characteristics would not be easily identified in an ideal steady-state analysis. On the other hand, there is a case where the analysis was performed assuming a small air-gap size (3 mm) in the simulation [88]. In that study, as the air-gap size decreases, the NI characteristics become more influential, but it has been suggested that there is no negative effect of this leak current.

Transient Operation Analysis

Lastly, based on the proposed equivalent circuit model in section 3.3.1, characteristics in transient operation were derived. In this study, The MATLAB Simulink was used for time-dependent simulation of the equivalent circuit with two feedback controllers for synchronous motors: 1) a simple PI controller to control the motor speed, and 2) a vector controller for the armature current [87]. Considering the air-cored structure of the motor ($L_{md} = L_{mq}$), armature current is controlled to be $I_{da} = 0$ for maximum torque generation which is commonly used in surface permanent magnet synchronous motor (SPMSM).

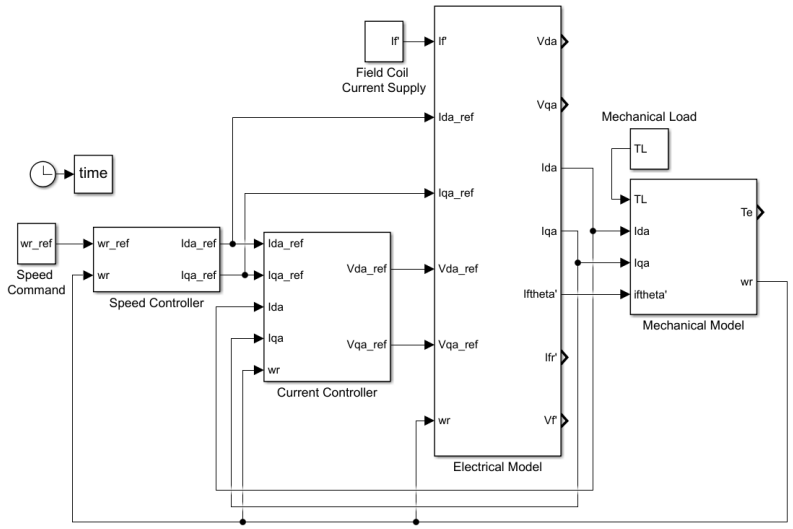

Figure 4.10: The overall structure of MATLAB Simulink simulation model.

Figure 4.10 shows the overall schematic of MATLAB Simulink used in this study. The detailed implementation is included in appendix A.4. The power supply current for the field coil is assumed to be ideally controlled by a current source at 66.2 A. Circuit and mechanical parameter values used in the simulation are summarized in table 4.4.

In the case of the motor designed in this study, since there is no damping circuit, the corresponding parameters were not considered in the simulation. In the case of the inductance of the equivalent circuit, after calculating through the energy method in FEM simulation, the value was converted to the armature side by considering the number of turns between the armature and field coil. As a mechanical parameter, rotating inertia was calculated using a commercial tool based on the designed CAD drawing (section 4.2.2).

Table 4.4: Circuit and Mechanical Parameters for MATLAB Simulink Simulation

Parameters	**Values**	**Parameters**	**Values**
L_{md}, L_{mq} [mH]	0.817	L_{la} [mH]	1.86
R_a [mΩ]	0.278	L'_{lf} [mH]	0.712
$R'_{f\theta}$ [Ω]	~ 0	R'_{fr} [$\mu\Omega$]	14.1
J_r [kg·m^2]	0.111	B [Nm/(rad/s)]	0.0201

All operations except steady-state operations can be considered transient operations. Various transient simulations were performed, but in this section, the following situation in which the characteristics of transient operation are well exhibited was set as an operation scenario and the results were summarized: half of the rated mechanical load is suddenly applied while the motor drives at a target rotation speed. For comparison, simulations on the insulated counterparts (INS) were also performed, of which the equivalent circuit model is identical to that of NI in figure 3.7 except that R'_{fr} should be removed.

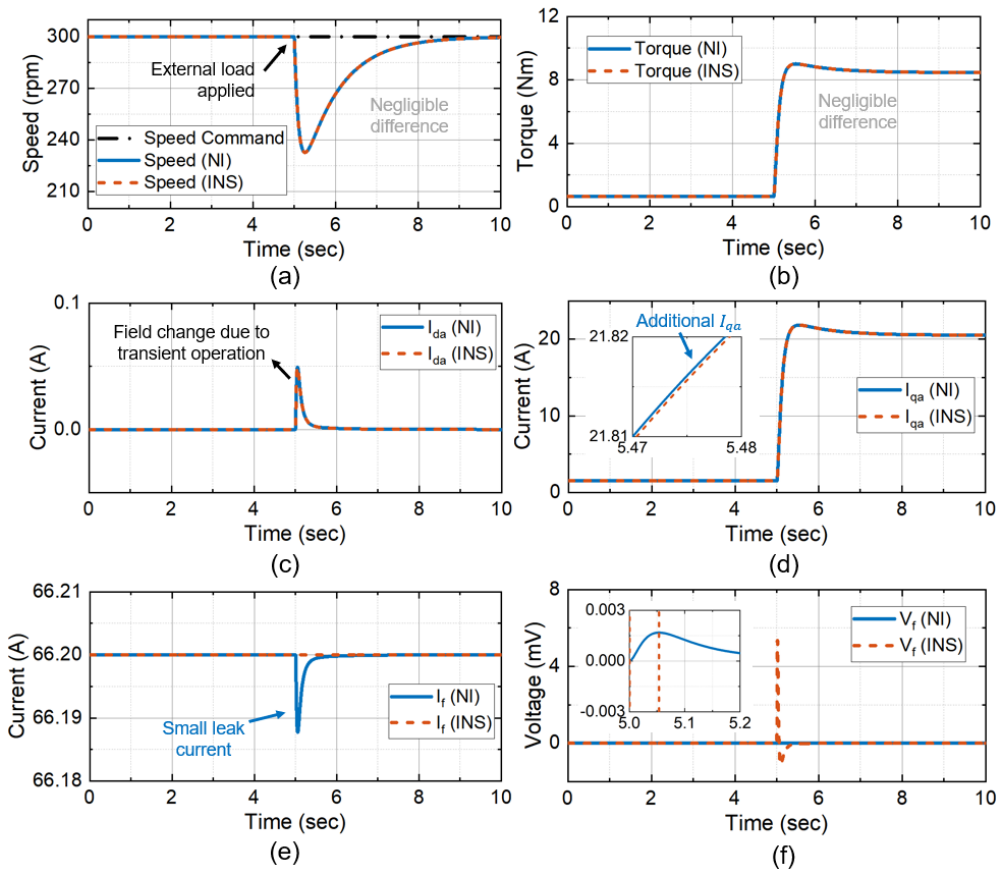

Figure 4.11: Sudden load simulation result. (a) Rotating speed (ω_r), (b) Torque (T_e), (c) d-axis current (I_{da}), (d) q-axis current (I_{qa}), (e) Azimuthal current of the field coil, (I_θ), and (f) Voltage of the field coil (V_f).

Figure 4.11 shows the simulation result: (a) rotating speed of the motor, ω_r, (b) total torque of the motor, T_e, (c) d-axis current of the armature coil, I_{da}, (d) q-axis current of the armature coil, I_{qa}, (e) azimuthal current of the field coil, I_θ, and (f) voltage of the field coil, V_f. In the figure, the solid blue line represents the result of NI, while the dashed orange line INS. A situation in which a torque corresponding to 50% of the target torque is suddenly applied at 5 seconds is simulated while driving at 300 rpm with no-load. The key observations in the transient simulation are summarized as follows.

- **Observation 1:** in simulation, the feedback current control is performed so that $I_{da} = 0$, but during transient operation, I_{da} momentarily becomes non-zero (figure 4.11 (c)). As I_{da} contributing to rotor magnetic flux is instantaneously generated, the NI REBCO coil is exposed to an external field change and turn-to-turn leak current is generated accordingly (figure 4.11 (e)).

- **Observation 2:** despite the change in the magnetic field due to the turn-to-turn leak current in the NI REBCO coil (figure 4.11 (e)), the difference in torque and speed between NI and INS in the simulation was almost negligible (figure 4.11 (a) and (b)).

- **Observation 3:** the reason for the negligible difference in speed and torque between NI and INS is due to speed feedback control. Torque is given as $T_e = \frac{3p}{4} L_{md} I'_{f\theta} I_{qa}$, and the possible change in torque due to turn-to-turn leak current ($I'_{f\theta}$) is being compensated by a slight change of I_{qa} (figure 4.11 (d))

- **Observation 4:** on the other hand, in the case of field coil voltage, a relatively low μV level voltage is induced compared to the insulated coil due to the low characteristic resistance of the NI REBCO coil (figure 4.11 (f)).

This simulation result shows that the effect of the turn-to-turn leak current generated is negligible under the assumption that $I_{da} = 0$ is well controlled as in simulation in

the case of air-cored structure. Also, with additional armature current injection, an NI motor could be controlled as an INS motor in terms of speed and torque. In conclusion, when controlling an air-cored type motor NI motor with $I_{da} = 0$ control, there was no critical problem identified in transient operation simulation.

However, when looking at the NI response by I_{da} and I_{qa} of the stator winding to be performed earlier, the response may appear sufficiently different under different control conditions using I_{da}. Also, even if $I_{da} = 0$ control, it is expected that an additional leak current may occur if ideal control is not achieved (when the inverter has an error in estimating the rotor position).

Parameter Table of Designed Test Motor

Table 4.5 summarizes key parameters among the results of a detailed analysis for the selected design.

4.2 Rotor Assembly and Cryogenic System Design for Experiment

As a next step of the electromagnetic design of the test machine, this section describes the design of the rotor assembly and cryogenic chamber for actual experiments. The CAD design of the rotor assembly was performed considering the mechanical fixation of the racetrack coil, and it was analyzed whether there was any problem of mechanical stress of the rotor assembly under the target operating conditions. For the cryogenic chamber, the size of the thermal load was estimated through FEM and the possible operating time was predicted. Also, the change of the rotating inertia according to LN_2 was estimated.

Table 4.5: Key Parameters of Designed Test Machine

Parameters		**Values**	**Parameters**		**Values**
REBCO Coated Conductor			**Armature Coil**		
Width; thickness	[mm]	4.1; 0.14	Number of stator slots		36
Sustrate; stabilizer thickness	[mm]	0.11; 0.03	Layers per slot		2
Self-field critical current	[A]	200	Turns per layer		14
E_r; E_θ; E_z	[GPa]	169; 175; 175	Winding pitch		7
REBCO Racetrack Field Coil			Connection		Wye
Number of poles		4	Stator inner radius	[mm]	85
Number of stacks per pole		1	Stator outer radius	[mm]	130
Inner radius of circular part	[mm]	28	Effective length	[mm]	180
Distance from rotating center	[mm]	49	Magnetic airgap	[mm]	15
Length of straight part	[mm]	180	Armature current density	[A/mm^2]	2.74
Turns per pole		80	Stator core		50PN470
Insulation method		NI	**Performance of Test Motor**		
Operating current	[A]	66.2	Phase voltage	[V_{rms}]	9.77
Field current density	[A/mm^2]	115	Line current	[A_{rms}]	28.9
Critical current	[A]	94.6	No-load voltage	[V_{rms}]	5.73
Peak magnetic field at coil	[T]	0.319	Total harmonic distortion	[%]	4.40
Operating temperature	[K]	77.4 (LN_2)	Armature resistance	[Ω]	0.338
Total field coil inductance	[mH]	11.4	Synchronous reactance	[pu]	0.464
Contact resistivity	[$\mu\Omega$·cm^2]	10	Cogging torque	[mNm]	28.3
Characteristic resistance	[$\mu\Omega$]	137	Torque ripple	[%]	1.15
Charging time constant	[sec]	83.2	Rotating speed	[rpm]	300
Total REBCO consumption	[m]	183	Output torque	[Nm]	15.9
Rotor core		Air-cored	Output power	[W]	498

4.2.1 Rotor Assembly Design and Mechanical Characteristics Analysis

In this section, based on the electromagnetic design, the rotor assembly structure was designed in consideration of actual fabrication. Before the detailed CAD design of the rotor assembly, the mechanical analysis of the designed racetrack coil was performed first, and the necessity of the support structure was determined. The CAD design was performed considering the support structure for mechanical fixing of the coil, air-cored structure of the rotor, and electrical connection between poles. Finally, an overall mechanical analysis was performed on the whole rotor assembly to determine whether it was mechanically stable.

Magnetic Stress Analysis Due to Lorentz Force

As one of the main stress sources of the mechanical stress of superconductor coils, magnetic stress is the stress that originated from Lorentz force, so magnetic stress becomes larger with higher current density and higher magnetic field. Displacement and magnetic stress due to Lorentz force generated during the charging process were calculated first in this section. In this study, the dry winding technique was applied to the racetrack coil mainly to avoid delamination problems [89], and magnetic stress calculation was performed considering the characteristics of the dry winding racetrack coil. The details of the performed stress calculation are in [67].

Table 4.6: Effective Mechanical Property of SuNAM's REBCO Coated Conductor

Parameters		**Values**
Thickness of substrate; stabilizer	[mm]	0.11; 0.03
Young's modulus of substrate; stabilizer	[GPa]	190; 120
Poisson's ratio of substrate; stabilizer		0.27; 0.34
Shear modulus of substrate; stabilizer	[GPa]	45; 74
Effective Young's modulus, E_r; E_h; E_z	[GPa]	169; 175; 175
Effective Poisson's ratio, ν_{rh}; ν_{hr}; ν_{hz}; ν_{zh}; ν_{zr}; ν_{rz}		0.275; 0.285; 0.280; 0.280; 0.285; 0.275
Effective Shear modulus, G_{rh}; G_{hz}; G_{zr}	[GPa]	65.0; 67.8; 65.0

The material properties used for stress calculation are shown in table 4.6. Based on the specification of SuNAM's REBCO coated conductor, effective mechanical properties were calculated and used based on the calculation formulas introduced in appendix A.2.

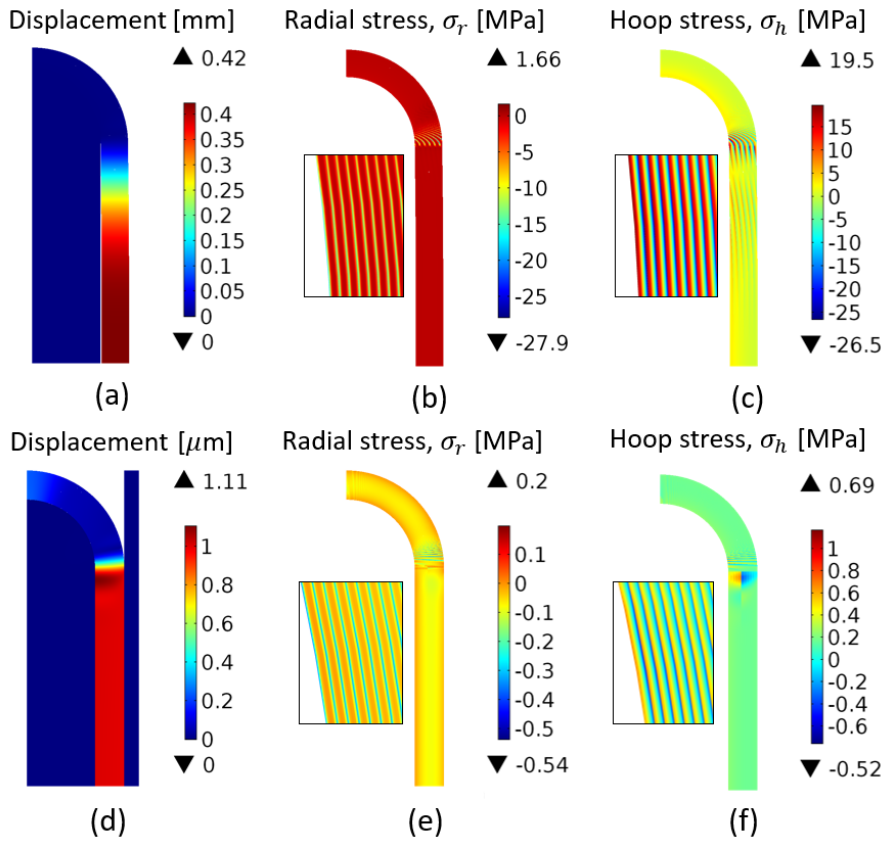

Figure 4.12: Results of the mechanical analysis on the racetrack. Without support - (a) Displacement, (b) Radial stress (σ_r), and (c) Hoop stress (σ_h). With support - (d) Displacement, (e) Radial stress (σ_r), and (f) Hoop stress (σ_h).

Figure 4.12 shows the mechanical analysis result when the dry-wound racetrack coil is excited to 66.2 A at 77 K. Figure 4.12 (a)–(c) shows displacement, radial stress, and hoop stress without support, respectively, while figure 4.12 (d)–(f)) shows displacement, radial stress, and hoop stress with support. Overall stress and strain are

calculated to be relatively low compared to their critical values since the Lorentz force induced in the coil is moderate level (figure 4.12 (b) and (c)). However, it was found that, despite such low-stress values, visible displacement (0.42 mm) occurred in the straight section as shown in figure 4.12 (a). It implies that a supporting structure of a straight section is required for sturdy fixation of the racetrack coil. By restraining the displacement at the straight section of racetrack coils with an ideal supporting structure, calculated displacement and stress could be effectively reduced in the simulation (figure 4.12 (d)–(f)). As a result, in this study, to fix the turns of dry wound racetrack coil, supporting structure of straight section were considered even at the low-stress value in simulation.

CAD Design of Rotor Assembly Considering Mechanical Support Structure

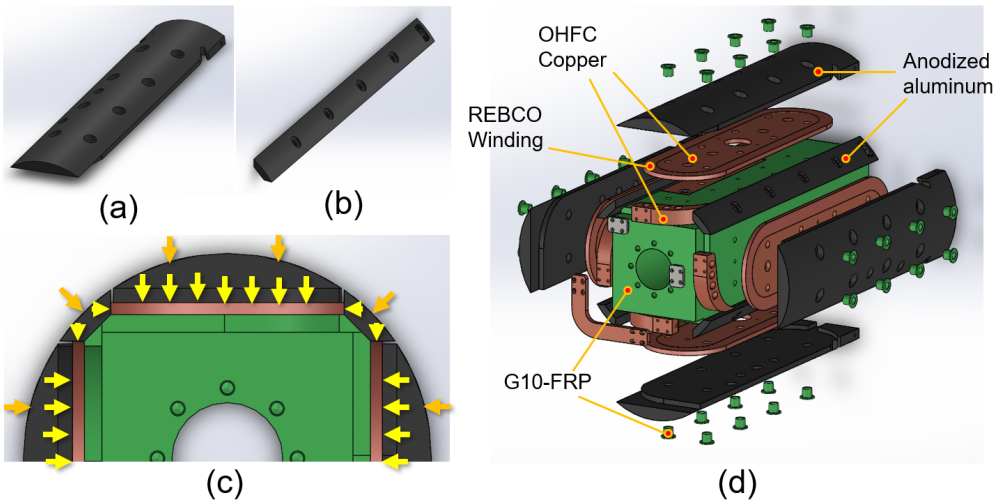

Figure 4.13: (a) An upper support structure, (b) A side support structure, (c) Pre-load directions by support structures, and (d) Overall configuration.

Based on the electromagnetic design and mechanical analysis result of the racetrack coil, a CAD design of the rotor assembly for actual fabrication was performed. Racetrack coils were placed on each pole, and the rotor body part, support structure

part, and connector parts constituting the assembly were designed each. As a material of the rotor body, G10-FRP was selected for air-core structure and rotor weight reduction. For the stable operation of the designed racetrack coil as field winding, the support structures that can mechanically fix the racetrack coil were designed. The support structures are composed of 1) an upper support structure that can prevent the coil from moving in the outward direction from the rotating axis due to centrifugal force, and 2) a side support structure that can prevent displacement of the straight section in the racetrack coil by Lorentz force after excitation. Figure 4.13 (a)–(b) shows the designed upper support structure and side support structure, respectively, and (c) shows the drawing of the rotor assembled with these support structures and the direction of the applied force. The support structure receives pre-load in the direction of the orange arrows through the bolt, and through this, the forces to fix the racetrack coils are applied in the direction of the yellow arrow. The support structure was designed with anodized aluminum for better heat transfer through the support structures during cooling through LN_2. The rotor assembly was completed by adding copper connectors for current leads and pole-to-pole electrical connections. Figure 4.13 (d) shows the material of each component and its overall configuration.

Overall Mechanical Stress Estimation in Rotor Assembly

With the rotor assembly design, mechanical analysis was performed in consideration of the stress sources that may occur in the process from manufacturing to operation. Through mechanical analysis, it is necessary to check 1) whether the strain generated in the racetrack coil is below the level at which I_c degradation occurs, and 2) whether the stress generated in other components is below their yield strength. Classification of mechanical stress on the superconducting system according to time sequence is as follows.

- Stress due to pre-load is applied through bolts to fix each part during the assembly process of the rotor.

- Thermal stress is caused by different thermal expansivity when the rotor is cooled from room temperature (300 K) to cryogenic temperature (77 K).
- Magnetic stress due to Lorentz force is applied when the racetrack coil is excited.
- Stress due to additional operations could be additionally generated. In the case of rotating machines, stress from the centrifugal force would be applied.

First, in the case of pre-load by bolt, the fastening force of the bolt according to the bolt size was considered. The M6 bolt used for upper support was assumed to have a pre-load of 9.01 kN, and the M3 bolt used for side support was assumed to have a pre-load of 3.93 kN [90], which was considered as the boundary load in the simulation. To consider thermal stress, thermal expansion data of the material of each part is required, and linear thermal expansion data (α_L = ($l(T)$-l(293 K))/l(293 K)) [%]) used for simulation was shown in table 4.7 [83]. Table 4.7 also includes other mechanical properties such as mass density (ρ_m), Young's modulus (E), Poisson's ratio (ν), and yield strength (E_Y), which are required for mechanical analysis.

Table 4.7: Mechanical Properties of Rotor Materials for Stress Calculation

Material	ρ_m [kg/m^3]	E [GPa]	ν [-]	E_Y [MPa]	α_L @ 80 K [%]
Aluminum	2700	70	0.33	280	-0.391
Copper	8960	120	0.34	280	-0.300
Stainless steel	7800	190	0.27	1100	-0.281
G-10 (warp)	1800	18	0.14	-	-0.211
G-10 (normal)		14	0.12	-	-0.638

For the REBCO racetrack coil, thermal expansion data of substrate (stainless steel) was approximately used. Thermal stress was calculated through multi-physics simulation in COMSOL combining solid mechanics module and heat transfer module [91].

The magnetic stress was calculated by importing the Lorentz force from 3D FEM magnetic field analysis with I_f = 66.2 A. Finally, considering the mass density of each material (table 4.7), centrifugal force was calculated by analytic equation ($F_c = \rho_m r \omega_r^2$ [N/m^3], where r is the radius from the rotating axis), and used for stress calculation by centrifugal force. ω_r is assumed to be 300 rpm.

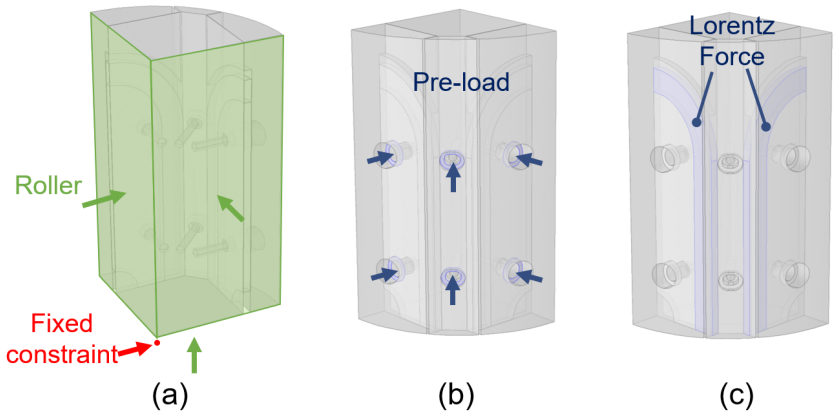

Figure 4.14: Boundary conditions for analysis. (a) Roller condition and fixed constraint condition, (b) Pre-load condition, and (c) Body load condition by Lorentz force.

Figure 4.14 shows a simplified model FEM analysis and its boundary conditions. Considering the symmetric structure of the rotor, only the 1/8 section of the rotor was used for analysis, and the roller condition was applied for the symmetric boundary. A fixed constraint was set for the central point of the rotor. Figure 4.14 (b) and (c) show how the pre-load and Lorentz force were applied as loads in the simulation, respectively, and the thermal contraction and centrifugal force were analyzed by applying the corresponding conditions to the entire rotor.

Figure 4.15 shows the von Mises stress values for each rotor component when all stress sources are considered. In the case of the REBCO racetrack coil, its peak stress value is 72 MPa, which is far lower than the typical critical stress value when I_c degradation occurs. The peak stress of copper bobbin and two types of aluminum

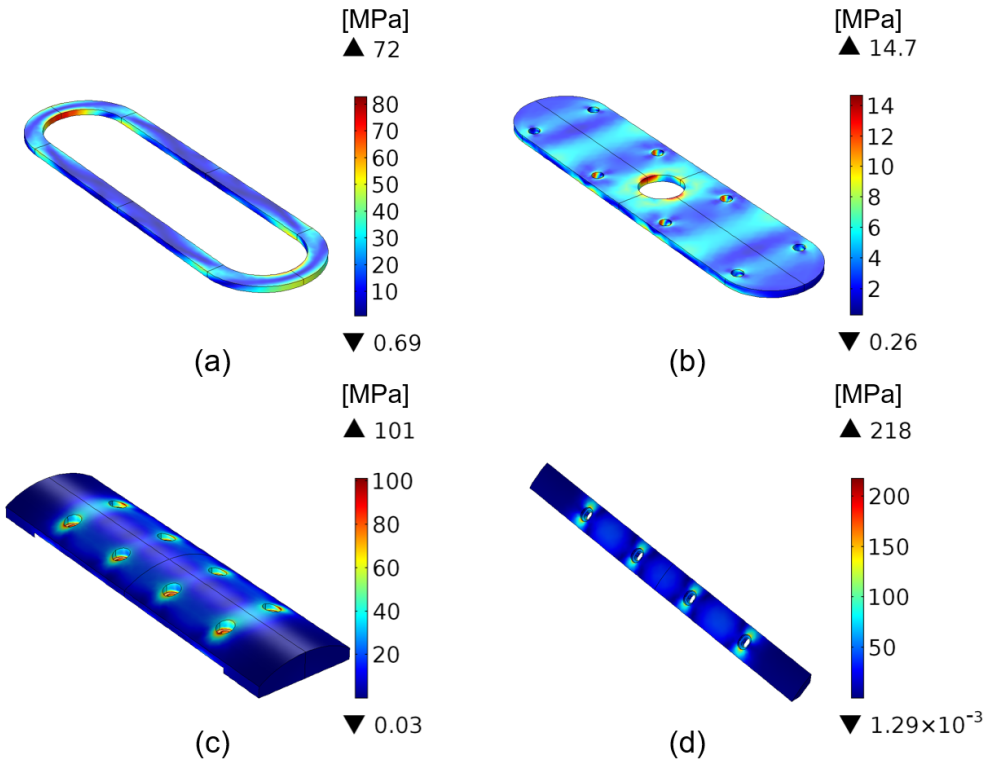

Figure 4.15: von Mises stress of each rotor component. (a) REBCO racetrack coil, (b) Copper bobbin, (c) Upper support structure, and (d) Side support structure.

supports are 14.7 MPa, 101 MPa, and 218 MPa each, which are lower than the yield strengths of 275 MPa and 380 for each material at 77 K [83].

Table 4.8: von Mises Stress Calculation Results in Each Loading Process

Component	**von Mises stress, σ_{mises} [MPa]**			
	Pre-load	**Thermal**	**Magnetic**	**Rotation**
REBCO racetrack coil	19.3	72.8	72.0	72.0
Copper bobbin	18.8	14.9	14.7	14.7
Aluminum upper support	128	129	129	101
Aluminum side support	113	220	220	218

Table 4.8 shows when the peak von Mises stress in each part is summarized considering the load added in each process from the assembly to the rotating operations. As can be seen from the results, the change in peak stress due to Lorentz force and centrifugal force in the rotor of this study was almost negligible. This is thought to be because the operating current and rotation speed in this study are relatively low. This suggests that the most mechanical stress in this study would be generated during the assembly process of the rotor using bolts and the cryogenic cooling process and additional care should be given to these processes.

4.2.2 LN_2 Chamber Design and Thermal Loss Estimation

As explained in the overall design direction of the test motor, in this study, LN_2 cooling was considered to maintain the superconductivity of the field winding. Several cooling concepts could be possible with LN_2, and an appropriate design of the LN_2 chamber is required. Therefore, in this section, issues related to chamber design were first reviewed and some key concepts were decided based on the purpose of the test motor, and then the chamber was designed. Thermal load to the chamber and the operating time accordingly were estimated on the given design. Also, as the rotating LN_2

chamber is adopted for a cooling system, the rotating inertia may change due to the evaporation and movement of LN_2 in the chamber. Because the rotating inertia is one of the key parameters representing a mechanical property of the motor, therefore, the possible change range of the rotating inertia was additionally investigated.

Design Considerations on LN_2 Cryogenic Chamber

In this study, a simple and inexpensive cooling system using LN_2 was attempted. For the cooling system configuration using LN_2, the following factors were reviewed as key considerations.

- **Consideration 1 - LN_2 Dunk vs. LN_2 Circulation:** when cooling using LN_2, there are a dunk-type cooling in which a system is put in a chamber containing LN_2, and a circulation-type cooling that cools a system indirectly with pipes in which LN_2 circulates. In the case of the LN_2 dunk method, cooling is easily performed and the temperature of the components in the chamber can be stably maintained at 77 K, but the operation time is limited by the evaporation of LN_2. In the case of the LN_2 circulation method, a rotating cryogen coupling or a cryogen transfer system is required for LN_2 circulation in a rotating chamber. Especially, the design and manufacturing complexity of the rotor is greatly increased. Therefore, in this study, since the NI applicability is the primary goal, the dunk cooling method, which is relatively easy to manufacture and operate, was adopted.

- **Consideration 2 - Only Rotor in LN_2 vs. Whole system in LN_2:** in the case of dunk cooling, only the superconducting rotor can be cooled with LN_2, or the entire motor system including the stator can be cooled with LN_2. When the entire motor system is cooled with LN_2, fluid resistance of LN_2 could exist when the rotor rotates, and a relatively large amount of LN_2 is consumed due to the loss of the stator. In particular, since the cryogenic operation performance

of components other than superconducting coils is not guaranteed (especially bearings), a method of cooling only the rotor with LN_2 was adopted even with the relatively large air-gap (15 mm) for the chamber wall.

- **Consideration 3 - Vacuum layer vs. Thermal insulation layer:** with the LN_2 dunk mode cooling, the possible operating time is determined according to the amount of cryogen contained and the thermal load. External heat intrusion is one of the major thermal loads of the LN_2 chamber. As a method to minimize the amount of heat intrusion into the chamber, there is a method to make a vacuum wall by composing the chamber wall as a double layer. However, in the case of a vacuum layer, the required air-gap becomes larger and the output torque of the test motor could be decreased. In this study, in order to maintain the size of the air-gap, an additional thermal insulation layer was added to the chamber to reduce the amount of heat intrusion and an additional chamber height was designed to secure enough operation time.

Figure 4.16 shows the overall LN_2 chamber concept determined based on the above considerations and cross-sections at each location. A 5 mm chamber wall exists in the 15 mm air-gap between the rotor and the stator, and a 10 mm thermal insulation layer was added to the rotor part that is not enclosed by the stator (figure 4.16 (b)). As can be seen in the cross section of (b)–(c), a sufficient gap of 5 mm was placed between the rotor assembly and the chamber wall to prevent the evaporated N_2 bubble from being stuck inside. Accordingly, the mechanical air-gap between the rotating part and the stationary part was determined to be 5 mm. The additional chamber height above the rotor assembly is to secure enough operation time according to the thermal load, and the height (h_1) was determined by performing thermal analysis.

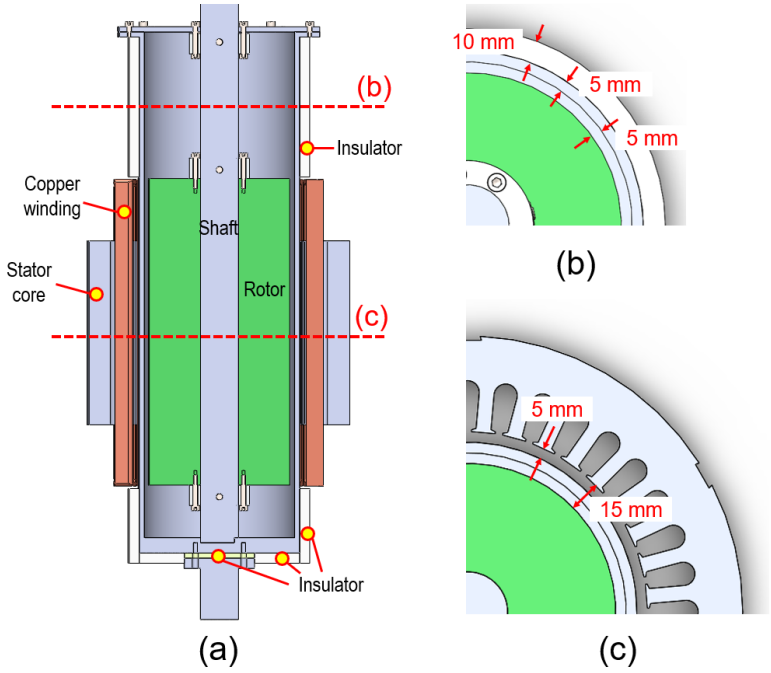

Figure 4.16: Concept of LN_2 chamber for test motor. (a) Front cross-sectional view, (b) Cross-sectional view at the upper part, and (c) Cross-sectional view at the middle.

Thermal Load Estimation in Cryogenic Chamber

In this section, the thermal load of the chamber was calculated, and based on this, the operable time for one LN_2 charge was estimated. In order to stably maintain the temperature of the field winding at 77 K, it was assumed that the upper end of the rotor was always submerged in LN_2 during operation. Therefore, when LN_2 is fully filled up to the additional height (h_1) of the chamber, the time when the LN_2 surface level reaches the upper end of the rotor by evaporation was defined as a possible operation time in this study. At the additional height of the chamber, the diameter of the shaft and the inner diameter of the chamber wall are 38 mm and 150 mm, respectively, and LN_2 is filled between these spaces. Here, if the height of the additional chamber is h_1, the latent heat of LN_2 is 161 J/cm^3 [83], so the total heat of vaporization of LN_2 is

given as h_1[cm]$\times$26.6 [kJ/cm]. Given this capacity of LN_2, in order to estimate the operating time, the thermal load including AC loss of the REBCO racetrack coil and thermal intrusion into the cryogenic chamber should be considered.

In the case of the NI HTS racetrack coil's AC loss, in addition to magnetization loss, there is turn-to-turn loss from leak current through contact resistance. In the case of motor operation, AC loss can be generated under various operating conditions, but since the charging-discharging process is one of the operations where AC loss occurs the most, the AC loss during the charging process was calculated at this time.

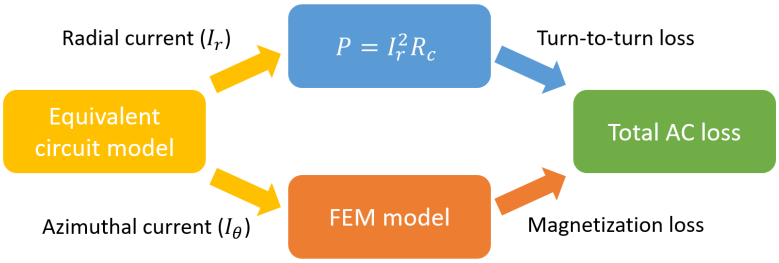

Figure 4.17: Calculation process for AC loss of NI HTS coil [92].

To estimate the total AC loss of the NI HTS coil, the calculation process as shown in figure 4.17 [92] is considered. In this calculation process, firstly, an azimuthal current (I_θ) and a radial current (I_r) are calculated in a given operation situation based on the equivalent circuit model, respectively. With I_r, the turn-to-turn loss ($= I_r^2 R_c$) is first calculated, and then the magnetization loss is calculated based on the FEM with I_θ. Finally, the total AC loss is calculated as a sum of them.

In this study, the H-formulation method was used to calculate the magnetization loss of the racetrack coil [93, 94]. In H-formulation, field distribution and magnetization loss are calculated using the following governing equation with $\boldsymbol{H}$ as a variable

for efficient calculation on FEM.

$$\nabla \times (\rho_{sc} \nabla \times \boldsymbol{H}) = -\frac{\partial (\mu_0 \mu_r \boldsymbol{H})}{\partial t}, \tag{4.3}$$

$$\nabla \times \boldsymbol{H} = \boldsymbol{J}, \tag{4.4}$$

$$\boldsymbol{E} = \rho_{sc} \boldsymbol{J}, \tag{4.5}$$

$$\boldsymbol{B} = \mu \boldsymbol{H}, \tag{4.6}$$

$$\rho_{sc} = \frac{E_c}{|\boldsymbol{J}|} \left(\frac{|\boldsymbol{J}|}{J_c} \right)^n, \tag{4.7}$$

$$P_{AC} = \int_V \boldsymbol{E} \cdot \boldsymbol{J} \, dV. \tag{4.8}$$

In the above equation, ρ_{sc} and P_{AC} represent resistivity and magnetization loss of the superconductor, respectively. More details about H-formulation can be found in [93].

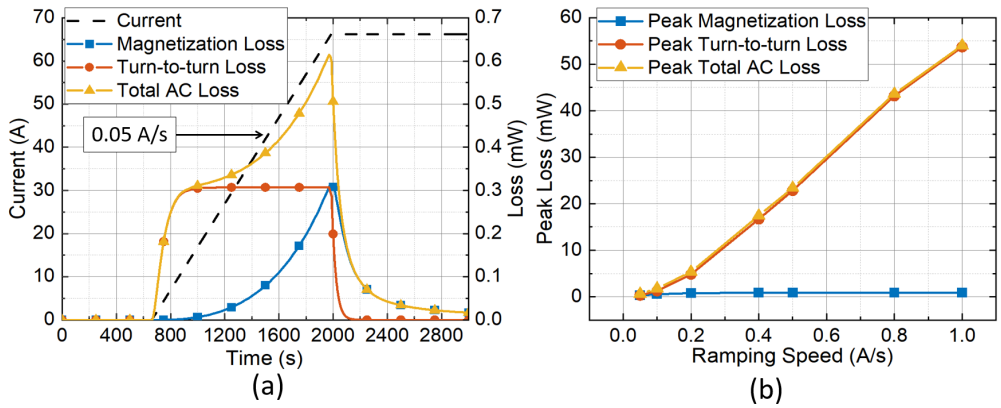

Figure 4.18: AC loss calculation results of the coil. (a) AC loss during charging process with 0.05 A/s, (b) Comparison of AC loss with different ramping speeds.

Figure 4.18 shows the AC loss calculation result. The magnetization loss and turn-to-turn loss generated when charging up to the target operating current at the rate of 0.05 A/s are shown in figure 4.18 (a), and figure 4.18 (b) is the peak values of AC loss in accordance with ramping speeds. In figure 4.18 (a), it can be seen that the amount of magnetization loss generated increases as I_{op} increases during the charging process, while turn-to-turn loss remains constant with a constant ramping rate. In figure

4.18 (b), As the current ramping speed increases, the turn-to-turn loss increases significantly, hence the total loss increases as well. As the ramping rate becomes fast, the turn-to-turn loss becomes a major loss. However, when looking at the magnitude of the total loss, even if four racetrack coils are considered, the generated heat is less than 1 W, indicating that the LN_2 latent heat is sufficient to cover it.

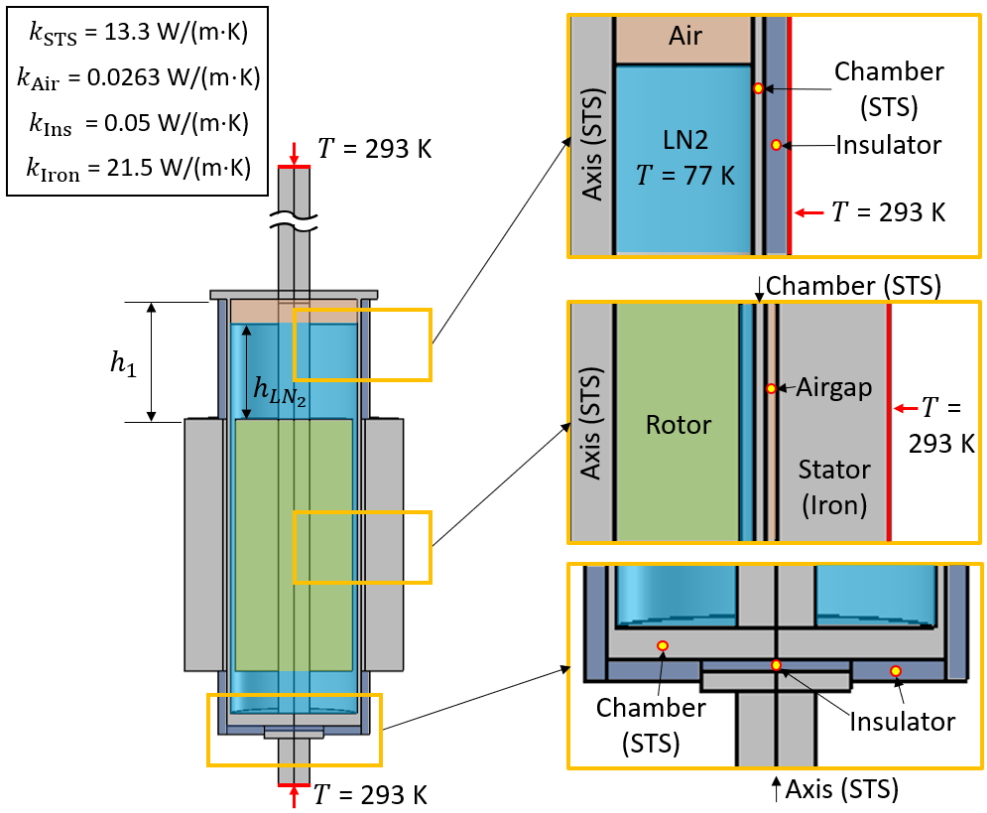

Figure 4.19: Thermal analysis condition of LN_2 chamber.

Next, the heat intrusion into the LN_2 chamber, which is the largest source of the thermal load, was calculated. When a gradient of temperature $(T_1 - T_2)$ exists, heat intrusion occurs depending on the conductivity (k), thickness (L_t), and conduction area (A_c) of the material, and the theoretical formula for an ideal plane wall having a

thermal gradient is given as follows.

$$Q = kA_c \frac{T_1 - T_2}{L_t}. \tag{4.9}$$

In the case of the designed cooling chamber, heat is conducted inside in various directions, unlike a simple plane wall, so a simulation was performed using a commercial FEM module (COMSOL Multiphysics) having the above analytic equation as the governing equation. Figure 4.19 shows the FEM simulation conditions. The additional chamber height is h_1, and the height of LN_2 in the chamber is h_{LN2}. As shown in figure 4.16, the thermal insulator was given, and the additional insulator structure for the thermal insulation of the chamber bottom was also considered. The temperature of the part in contact with LN_2 inside the chamber was assumed to be 77 K, and the temperature of the part exposed to external air on the side of the system such as an external surface of the thermal insulation layer and stator was assumed to be room temperature (293 K). Also, assuming that both ends of the shaft are at room temperature (293 K), heat intrusion from the shaft was also considered. The thermal conductivity values of the materials used are shown in figure 4.19.

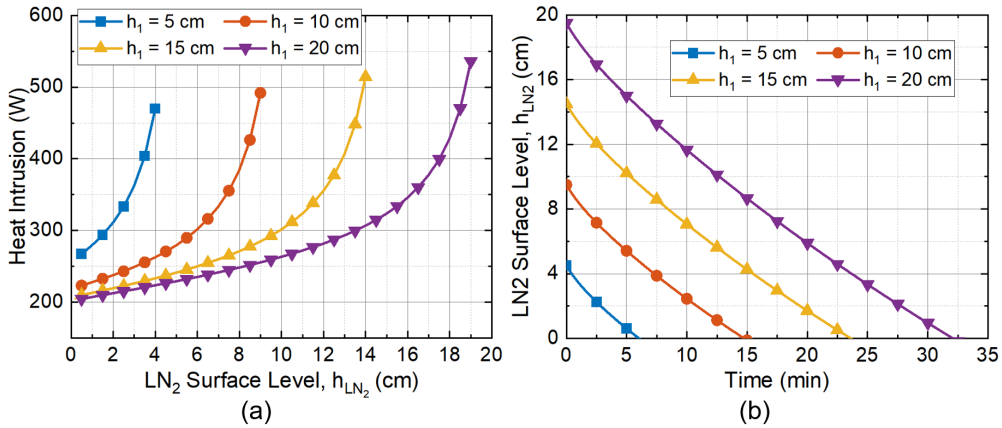

Figure 4.20: (a) Thermal load into LN_2 chamber with different additional lengths, (b) Possible operating time of LN_2 chamber with different additional lengths.

Figure 4.20 (a) shows the calculated thermal intrusion value by changing h_1 and

h_{LN_2}. When h_1 was given as 5 cm, 10 cm, 15 cm, and 20 cm, the amount of heat intrusion was calculated, respectively. First, the overall heat intrusion ranged around several hundred watts, and it was found to be much more dominant compared to the AC loss of the racetrack coil. Also, even with the same h_1, the amount of heat intrusion changed according to h_{LN_2}. Using the previously obtained total vaporization heat of LN_2, the LN_2 surface level according to the operation time was calculated as shown in figure 4.20 (b). When the additional length was 5 cm, 10 cm, 15 cm, and 20 cm, respectively, the operable time per one LN_2 charge was 4.78, 11.3, 18.0, and 24.4 minutes, respectively. In this study, an additional length of 15 cm was determined as the final chamber design with the goal of operation for more than 15 minutes.

Rotating Inertia Change Estimation due to LN_2

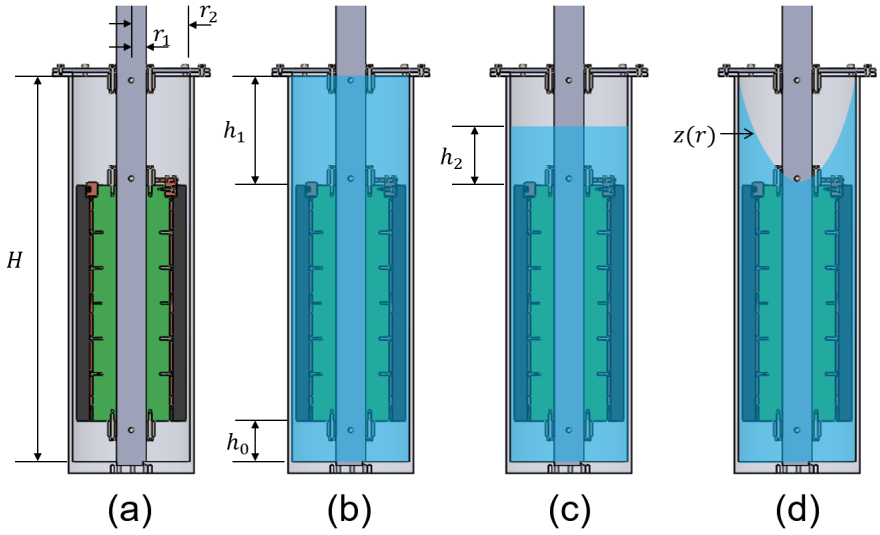

Figure 4.21: Rotating inertia calculation in different cases. (a) Without LN_2, (b) Fully filled with LN_2, (c) Half filled with LN_2, and (d) Rotated after half filled with LN_2.

In the case of the rotor with the LN_2, since LN_2 rotates together in the chamber, the rotating inertia of the rotor may be changed by the amount of LN_2 filled and the

fluid movement inside the chamber. In order to estimate the change in mechanical properties, as shown in figure 4.21, four situations in which LN_2 is contained in the chamber were set, and the difference in rotational inertia was estimated and compared. (a) is a situation in which no LN_2 is in the chamber, so the rotating inertia is the smallest, (b) is a situation in which LN_2 is fully filled, so the rotating inertia is the largest. (c) and (d) are to compare the difference of rotating inertia in the internal movement of LN_2 although the same amount of LN_2 is filled. (c) is a case in which LN_2 is maintaining its surface parallel to the ground in a stationary situation, and (d) is a case in which LN_2 is being received centrifugal force during rotation and pushed out to the inner wall of the chamber.

In the case of rotating inertia of the designed rotor except for LN_2 (case (a)), it was calculated using a commercial tool (SOLIDWORKS) based on the CAD drawing, and the value was 0.111 kg·m^2. The rotating inertia due to LN_2 can be calculated by the following equation assuming that LN_2 exists axis-symmetrically in the rotor.

$$J_r = \int r^2 \, dm = \int r^2 \rho_m \, dV, \tag{4.10}$$

$$dV = z(r) 2\pi r \, dr, \tag{4.11}$$

$$J_r = 2\pi \rho_m \int r^3 z(r) \, dr. \tag{4.12}$$

In the above equations, J_r is the rotating inertia, r is the distance from the axis center, m, ρ_m, and V are mass, mass density, and volume. The calculation was performed considering the height of LN_2 that changes according to r by using the variable $z(r)$. In case (b) and (c), $z(r)$ was calculated by giving r_1 = 1.9 cm, r_2 = 7.5 cm, h_1 = 15 cm and h_2 = 7.5 cm, respectively, and as the density of LN_2, ρ_{LN_2} = 808 kg/m^3 was used [83]. In (d), the height of LN_2 surface is given as $z(r) = \frac{\omega_r^2 r^2}{2g} + h_1 - \frac{\omega_r^2 r_2^2}{4g}$ [95], where g is the gravity acceleration constant (9.8 m/s^2). The value of ω_r was assumed to be 300 rpm.

Table 4.9 summarizes the calculation results of rotating inertia in (a)–(d). Comparing the four results, the maximum possible change in the rotating inertia due to

Table 4.9: Rotating Inertia of the Rotor with LN_2

Cases	**Rotating Inertia**	**Increment due to LN_2**
Case (a)	0.111 kg·m^2	-
Case (b)	0.118 kg·m^2	6.86%
Case (c)	0.116 kg·m^2	4.33%
Case (d)	0.118 kg·m^2	6.06%

LN_2 was 6.86%, but, the expected change by LN_2 movement after filling LN_2 was $<2\%$. Therefore, it was expected that the mechanical properties change according to the movement of LN_2 in the chamber would not be critical.

4.2.3 Conceptual Design of Dynamo Test System with LN_2 Cooling

The overall configuration of the dynamo system was designed considering the design of the test motor using the LN_2 dunk cooling. Key considerations are as follows: 1) whether to configure the dynamo test system as a system with an axial axis or a system with a horizontal axis, and 2) how to configure the arrangement of additional system components for the experiment.

In general, commercial dynamo systems are constructed to have a horizontal axis, but in the case of a dynamo system for superconducting motors with a cooling system including LN_2, considering the easy application of the LN_2 cooling chamber, the axial type dynamo is sometimes considered as shown in figure 4.22 [96–98]. In this study as well, LN_2 dunk cooling is used, so an axial dynamo system was constructed, and the initial concept design was performed in a way that each component was placed inside the supporting frame as shown in figure 4.23.

Besides the designed superconducting motor and cooling chamber, as additional components need to be included in the dynamo system for experiments, it is necessary to arrange the slip-ring, bearing, shaft coupling, torque sensor, and load motor. In this

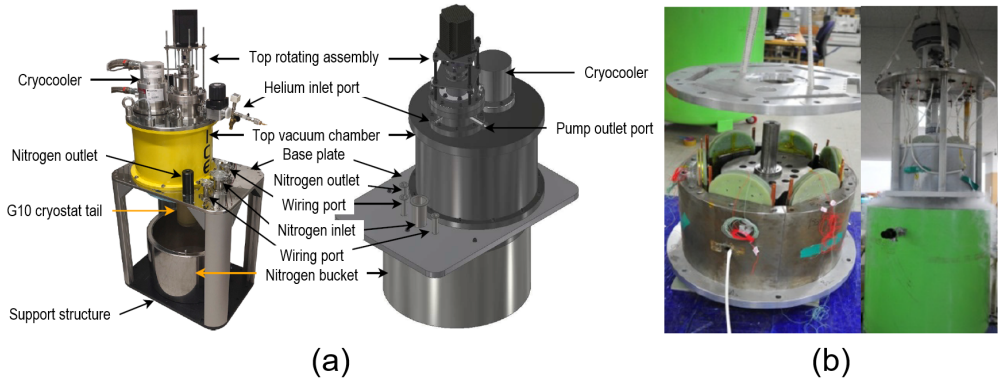

Figure 4.22: Axial dynamo system examples. (a) Experimental system with LN_2 cooling and cryocooler [96], (b) Experimental setting using LN_2 cryostat [97].

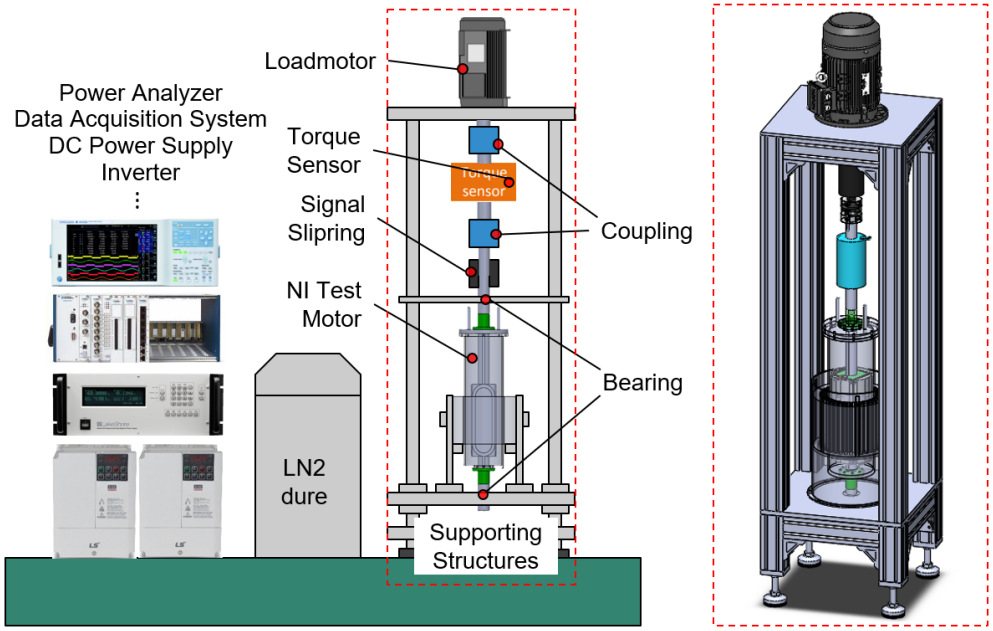

Figure 4.23: Concept design of axial dynamo test system.

system, these components are arranged as shown in figure 4.23 to avoid bearing friction caused by low temperature and to easily connect the power and signal lines.

Chapter 5

CONSTRUCTION OF TEST MACHINE AND EXPERIMENT SYSTEM

This chapter describes the construction of a test machine and experimental system for NI applicability investigation. Based on the results of the design and analysis in the previous chapter, NI HTS racetracks to be applied as field winding were first wound, and test machine assembly and test system construction were sequentially performed. The results of the performance inspection of the NI HTS racetrack coil and rotor assembly performed during the manufacturing process and the results of the heat intrusion estimation test of the LN_2 chamber were included.

5.1 Fabrication of NI HTS Racetrack Coils

5.1.1 NI HTS Single Pancake Racetrack Coil Winding

Superconductor coil winding methods can be divided into layer winding and pancake winding. In the case of conductors having circular shapes like NbTi and MgB_2 strands, layer winding has been commonly used. Meanwhile, in the case of a tape-shaped conductor like REBCO coated conductor, pancake winding is applied in general due to 1) easy modularization between coils, 2) high winding factor, and 3) prevention of local

mechanical damage in a conductor during the winding process.

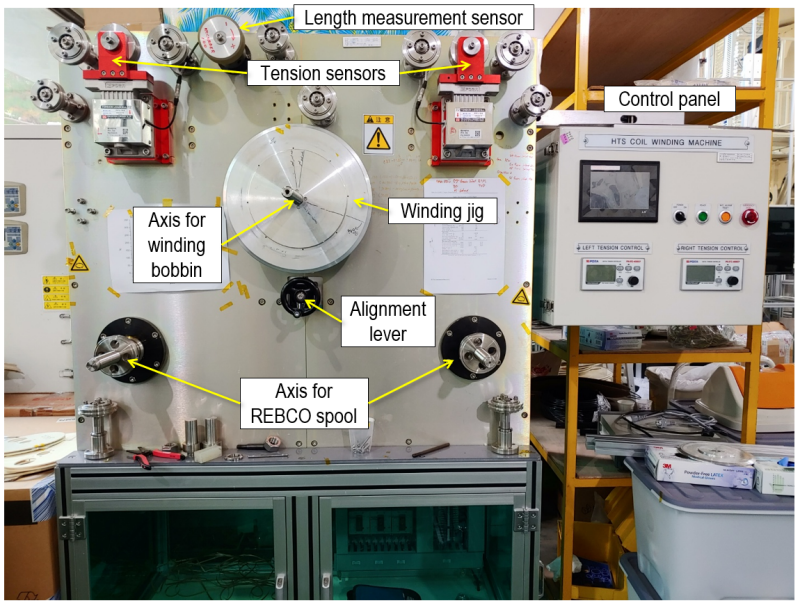

Figure 5.1: Winding machine for NI HTS racetrack coil winding.

There are few cases for layer wound no-insulation coils [42, 99], but the NI coil is typically wound based on the pancake winding method [35–41, 43, 44]. In the winding process, to manufacture it to have the performance as designed, precise alignment of each turn with the proper winding tension is required. For successful winding, depending on the shape of the coil to be wound, various winding machines have been manufactured and used for coil winding [16, 100, 101]. A configuration of the winding machine used in this study is shown in figure 5.1. The coil bobbin and the alignment jig are mounted on the center of the machine. REBCO coated conductor spool to be wound is fixed to the axis of the tension motors located on the bottom left and bottom right. Winding tension applied by the tension motor is controlled with tension sensors located on the top left and top right.

Four racetrack coils with the specification designed in section 4.1 were wound using the winding machine. Considering a potential delamination problem [89], coils

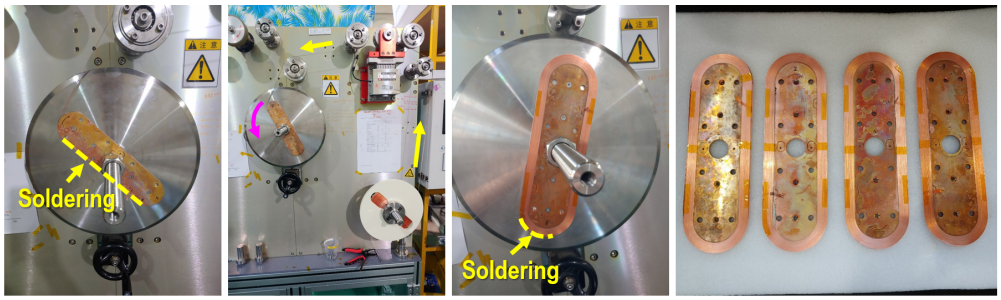

Figure 5.2: (a) Copper winding bobbin, (b) Winding process, (c) Fixation of the last turn, and (d) Four 80-turn REBCO racetrack coils.

were wound as dry-wound coils without impregnation. Figure 5.2 (a)–(c) shows the overall winding process. For winding, a SuNAM's REBCO coated conductor with 4.1 mm width and 140 um thickness was used, and the self-field I_c provided by the manufacturer was 200 A on average. With a copper racetrack coil bobbin, 80 turns of four coils are wound with the winding machine. At the beginning and the end of the winding, REBCO coated conductor is fixed by soldering (figure 5.2(a) and (c)). Considering electrical connection to adjacent pole through copper bobbin, superconductor layer of REBCO conductor was set to be faced the copper bobbin. During the winding, constant winding tension of 3 kgf is applied [51]. Figure 5.2 (d) shows fabricated four NI HTS racetrack coils.

5.1.2 Performance Inspection of Wound NI HTS Racetrack Coils

To inspect the performance of each wound NI HTS racetrack coil, the coils were tested individually at 77 K in an LN_2 bath. In the inspection process, as shown in figure 5.3, a test jig that can fix the straight part of the racetrack coils was fabricated and then charging-discharging tests were performed while fixing the straight part. This test jig is to prevent the characteristic change that might be induced from the movement of the straight part of the coil during charging, identified in section 4.2.1. In the experiment,

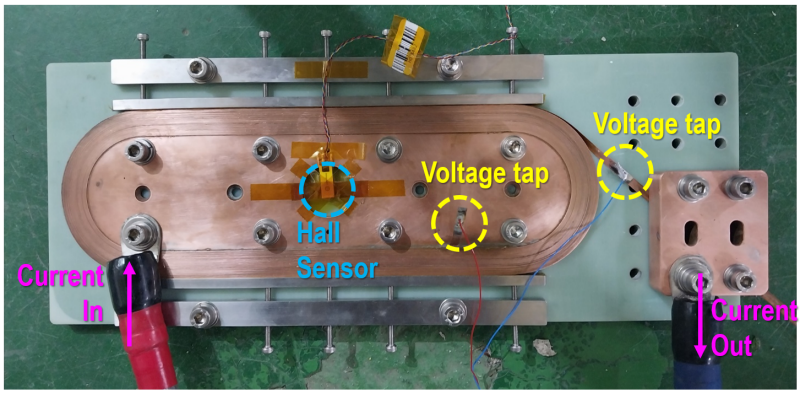

Figure 5.3: NI HTS racetrack coil attached to test jig for LN_2 test.

the power supply current, the terminal voltage of the coil, and the magnetic field at the coil center were measured. The power supply current was measured using a shunt resistance (WYSH-500), while the magnetic field a Hall sensor (Lakeshore HGCT-3020). As a power supply and a data acquisition system, Mercury iPS model of Oxford instruments and SCXI-1125 model of National instruments were used, respectively.

Figure 5.4 shows the charging-discharging test results of each racetrack coil. The black line with square markers represents the terminal voltage of the coil, the red line with circle markers is the power supply current, and the blue line with triangle markers is the magnetic field at the coil center. During the tests, the power supply current was ramped up to 66.2 A with 0.2 A/s. Test results were reversely calculated with the lumped parameter circuit model introduced in section 3.2, and coil inductance (L), charging time constant (τ), characteristic resistance (R_c), and field constant (K) were derived, respectively. The average value of contact resistivity (R_{ct}) was also obtained by using equation (3.11). Parameters of the tested racetrack coils were obtained as shown in table 5.1.

In the case of L and K, the difference between simulation and experiment was within 5%. However, in the case of R_{ct}, although the NI HTS racetrack coils were wound in the same way, different values of R_{ct} were experimentally derived between

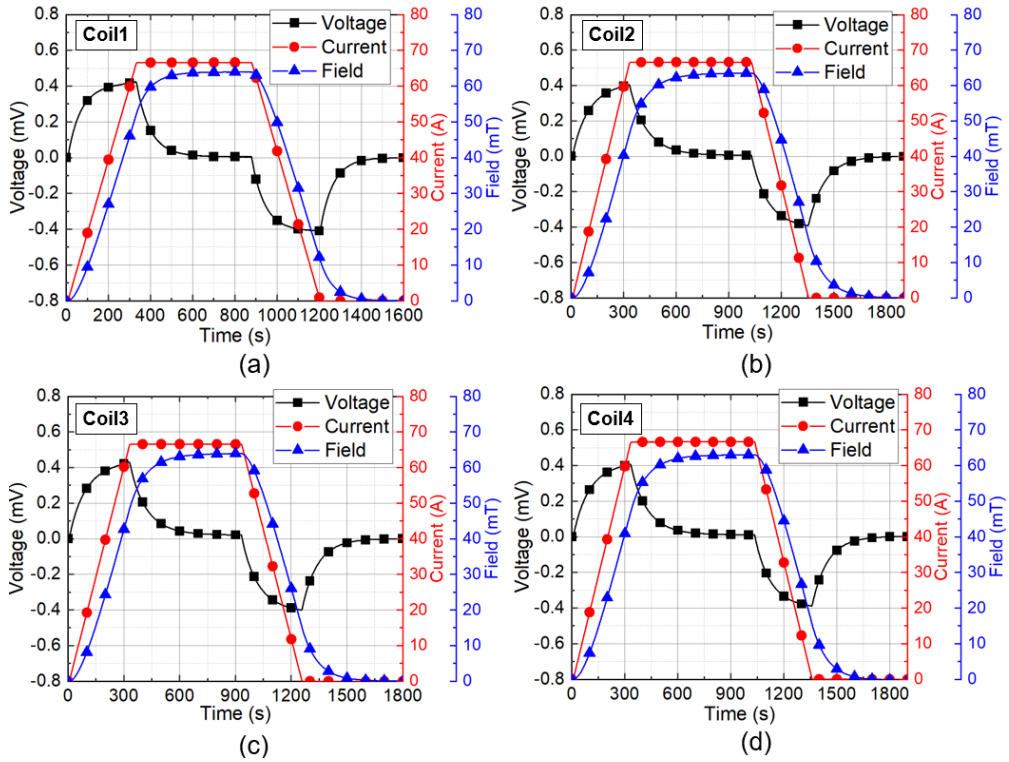

Figure 5.4: Charging-discharging test results at 77 K in LN_2 as performance inspection on (a) Coil 1–(d) Coil 4.

coils. This is a phenomenon often reported in magnets with multiple NI coils [79, 80]. In this study, in that the difference in NI response due to R_{ct} can also be compared experimentally, the fabrication process was carried out without rewinding.

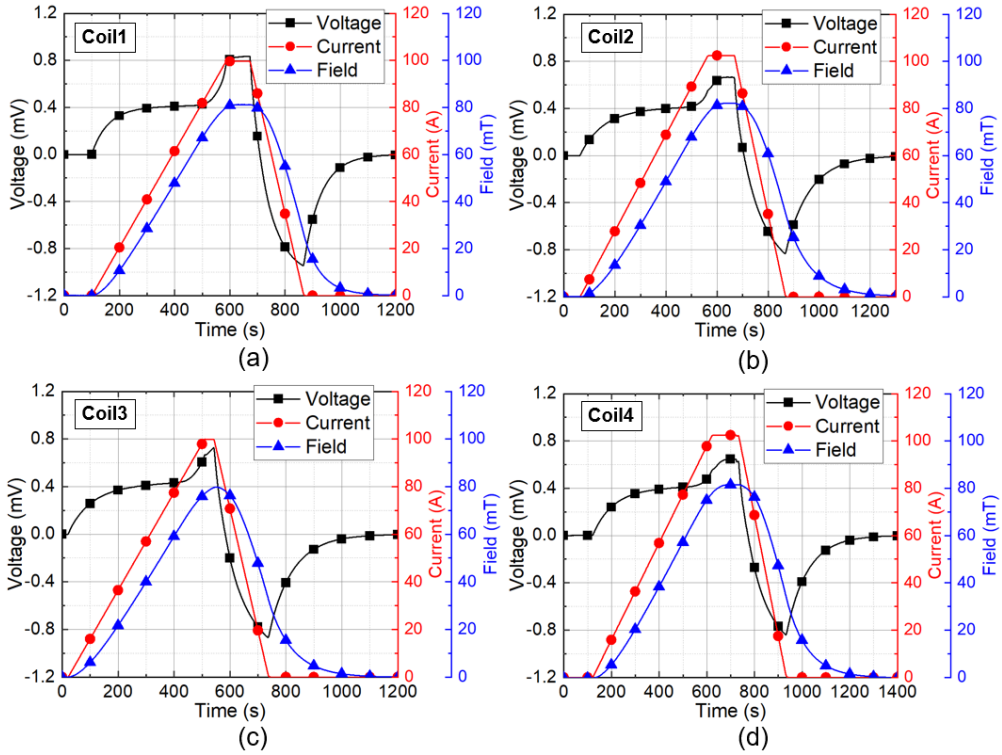

Figure 5.5: Over-current test results at 77 K in LN_2 as performance inspection on (a) Coil 1–(d) Coil 4.

Figure 5.5 shows the over-current test results of each racetrack coil. In this case, the power supply current was ramped up with a ramping rate of 0.2 A/s to >100 A, which is larger than the estimated critical current of 94.6 A. To estimate the coil's critical current (I_c), again, test results were reversely calculated with the lumped parameter circuit model with 1 μV/cm criterion and index value (n) of 20. Estimated I_c values of four coils through reverse calculation were in a range of 90.5–93.8 A, it shows up to a 5% difference from the simulation value. Considering the current margin in the

design of 30%, it was judged that it would be operated without any major problems at the target operating current.

Table 5.1: Coil Parameters from Individual LN_2 Test

Parameters	**Sim.**	**Coil1**	**Coil2**	**Coil3**	**Coil4**
Inductance, L [mH]	2.05	2.01	2.01	2.01	2.01
Characteristic resistance, R_c [$\mu\Omega$]	34.2	33.2	21.0	24.4	22.7
Contact resistivity, R_{ct} [$\mu\Omega$·cm^2]	10	∼9.5	∼6	∼7	∼6.5
Charging time constant, τ [sec]	59.9	60.6	95.9	82.2	88.6
Field constant at center, K [mT/A]	0.994	0.960	0.955	0.960	0.947
Critical current (1 μV/cm), I_c [A]	94.6	91.0	93.8	90.5	93.6

5.2 Construction of Test Machine with Wound NI HTS Racetrack Coils

The wound NI HTS racetrack coils were assembled with the other rotor components and a 4-pole rotor assembly was finally constructed. Figure 5.6 shows pictures of components fabricated for assembly and pictures of the completed rotor. The components except racetrack coils are largely composed of 1) a G10-FRP rotor body fixed to the rotating shaft, 2) aluminum support covers that mechanically fix and protect racetrack coils, and 3) copper connector blocks that are used as current lead and electrical connector between each coil. More details on each component are introduced in section 4.2.1.

During the assembly process, in the contact between the racetrack coil and the support structures, thermal grease was applied to the contact surface for better conduction heat transfer through support structures. In the case of electrical connections between each pole, the superconductor surface of the REBCO coated conductor faces

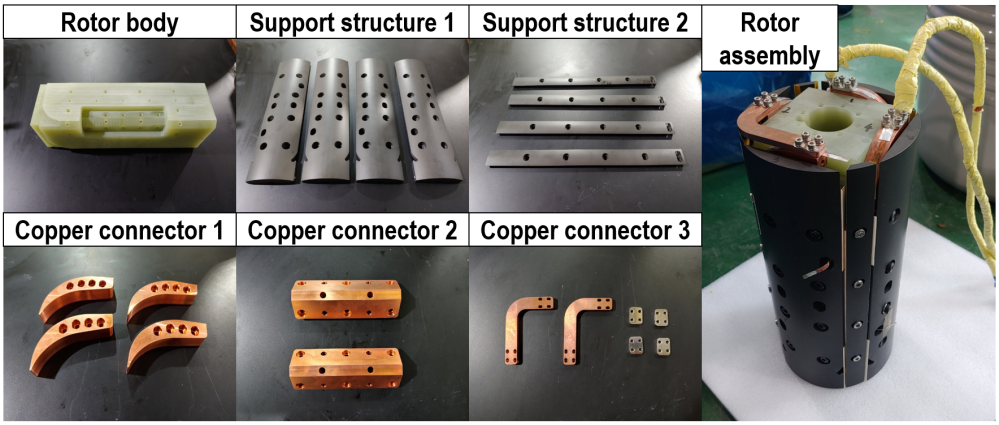

Figure 5.6: Pictures of the rotor components and assembled rotor.

the copper connector block to minimize electrical resistance between coils. Also, indium sheets were inserted in electrical connections for the same purpose. The inner diameter of the assembled rotor was 38 mm, the outer diameter was 140 mm, the axial length was 300 mm, and the total weight was 12.5 kg.

To confirm the performance of the assembled rotor and the electrical resistance at each connection between coils, the rotor assembly was tested again at 77 K in an LN_2 bath. Figure 5.7 shows the charging-discharging test result of the rotor assembly. The power supply current was ramped up to 60 A with 0.1 A/s. The terminal voltage of each coil and the voltage between coils were measured. The resistance values between each coil are 1.25 $\mu\Omega$, 6.28 $\mu\Omega$, and 1.92 $\mu\Omega$ (figure 5.7 (d)), which are much larger than the resistance value of each copper connector calculated through simulation (0.0975 $\mu\Omega$, 3.67 $\mu\Omega$, and 0.0975 $\mu\Omega$). This is thought to be because the contact resistance between electrical connections was more dominant than the resistance of copper connectors, and the average value of the contact resistance was calculated as 0.939 $\mu\Omega$. However, additional heat due to contact resistances at the rated current was 24.5 mW in the entire rotor, which was not critical compared to the heat intrusion estimated in the simulation (section 4.2.2).

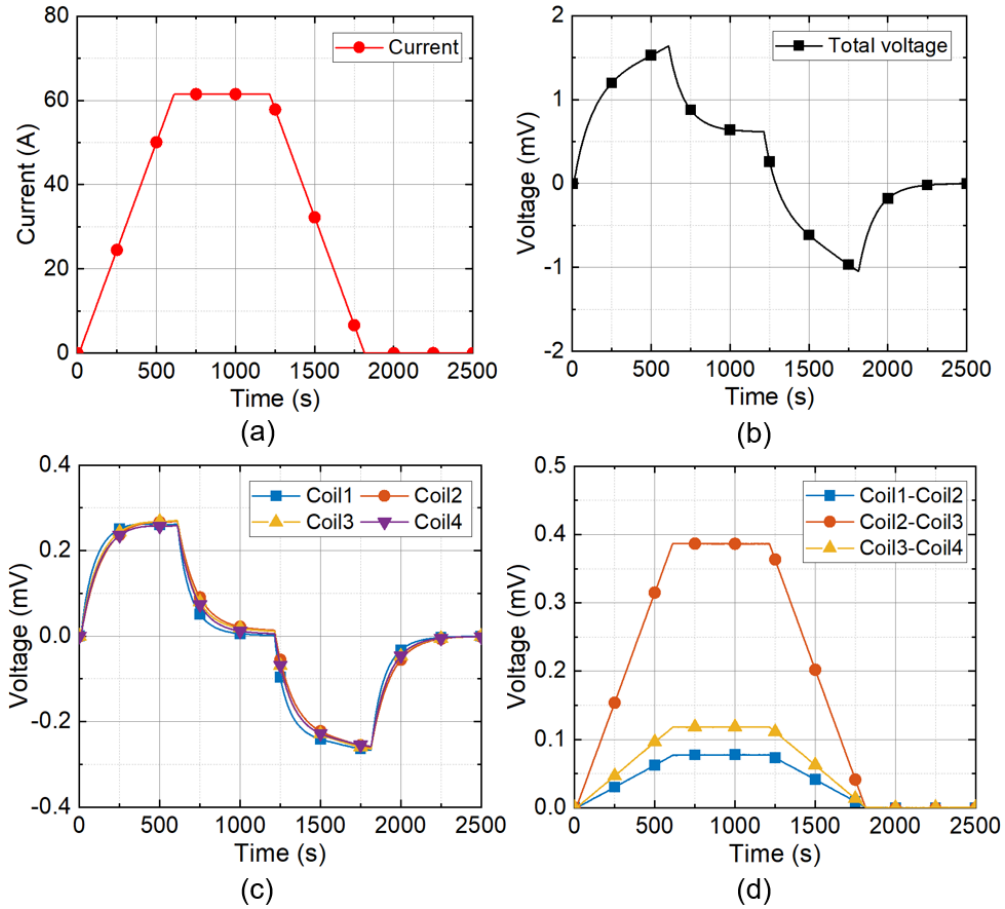

Figure 5.7: Charging test results of the rotor. (a) Power supply current, (b) Terminal voltage of the rotor, (c) Coil voltages, and (d) Voltage of connection between the coils.

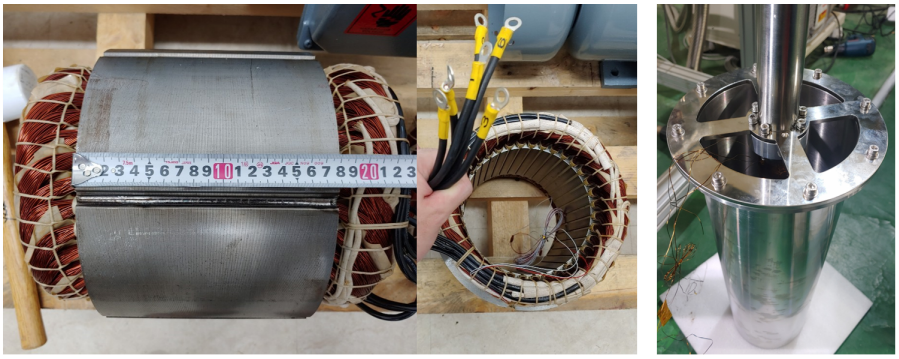

Figure 5.8: Picture of (a) a non-superconducting stator and (b) an LN_2 chamber.

After the charging test of the rotor assembly, the rotor was coupled to the manufactured LN_2 chamber (figure 5.8 (b)). To minimize heat intrusion to the LN_2 chamber, the external surface of the LN_2 chamber was enclosed by a 1 mm thick polyethylene thermal insulator as designed in section 4.2.2. In order to identify heat intrusion of the chamber through the experiment, LN_2 was fully filled in the chamber, and the time taken for LN_2 evaporation was measured using temperature sensors (Lakeshore DT-670) inside the chamber (figure 5.9). As shown in figure 5.9 (b), when the temperature sensor is located below the surface of filled LN_2, the temperature is maintained at 77 K, but when exposed above LN_2, it rises to $>$77 K. One temperature sensor was installed in the axis at 3 cm above from the upper surface of the rotor, and other two sensors were installed at the midpoint of the rotor. After filling the chamber with LN_2, the time taken to evaporate 12 cm of LN_2 was about 19.7 min, and the time taken to evaporate LN_2 to the midpoint of the rotor was about 33 min. Calculating the average heat intrusion through this, it was about 266 W on average, and it was estimated that about 25 min is taken before the upper surface of the rotor is exposed. This showed a difference of about 7 min from the simulation result in section 4.2.2. The error with the simulation is analyzed to be due to the conservative boundary condition in the simulation, which is that the external surface temperature is assumed to be 300 K in the

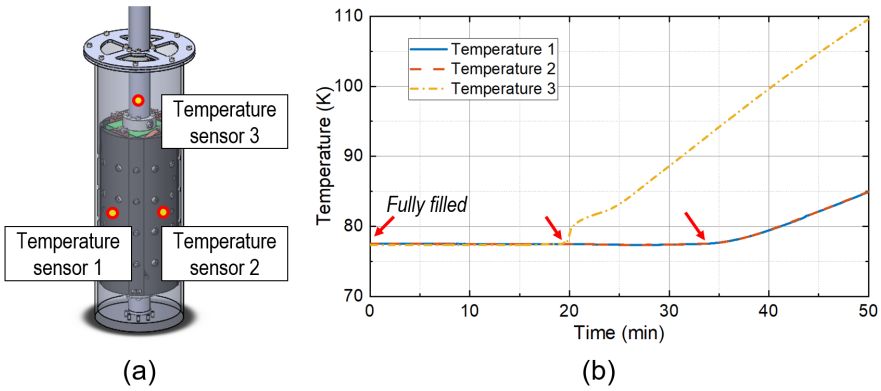

Figure 5.9: LN_2 surface level change measurement using temperature sensors. (a) Location of temperature sensors, (b) Temperatures during warm-up process.

simulation. However, in the actual experiment, the evaporated N_2 gas further cooled the surroundings of the chamber, so the temperature difference with the outside was relatively small. This cooling by N_2 gas was also identified in the experimental process performed in chapter 6.

5.3 Experiment System Construction

5.3.1 Construction of Axial Type Dynamo Test System

For the applicability experiment of the manufactured superconducting test machine, a customized dynamo test system was constructed. To use LN_2 dunk cooling, the overall dynamo system is constructed to have an axial axis. To configure the dynamo system, the following components were considered and arranged:

- **Slip-ring:** for current charging and signal measurement of the rotating NI HTS field winding, a slip-ring was placed just above the test motor and used.
- **Load motor:** for the back electromotive force measurement test and the torque measurement test of the test motor, a load motor capable of externally providing

the rotational speed and load was used.

- **Torque and speed sensor:** to measure the torque and rotating speed of the system, a torque and speed sensor was placed between the test motor and the load motor and used.

- **Encoder:** to control the starting and rotational speed of the test motor designed as a synchronous motor, an encoder was connected to the bottom of the test motor and used.

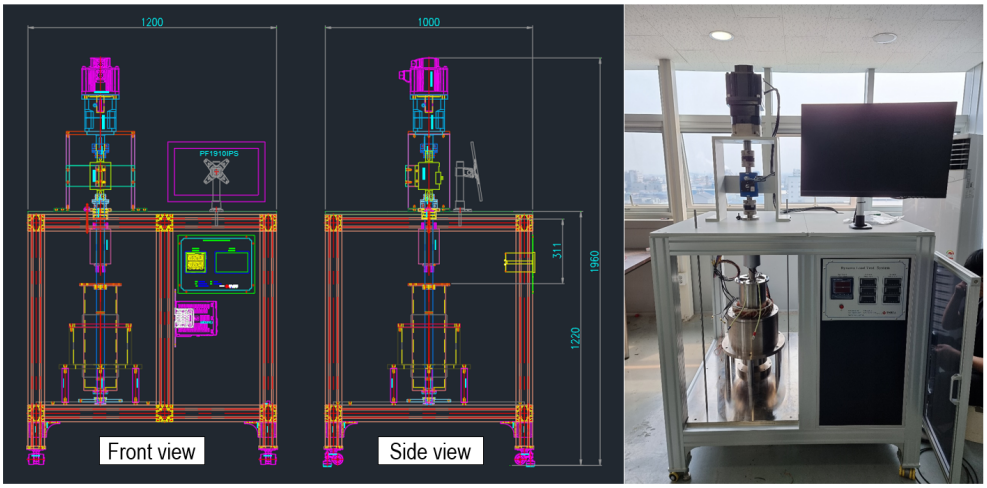

(a) (b)

Figure 5.10: Overview of dynamo test system. (a) 2D CAD drawing of the dynamo system for LN_2-cooled test motor, (b) A picture of assembled dynamo system.

The final 2D CAD design of the dynamo system is shown in figure 5.10 (a). Figure 5.10 (b) shows the actual dynamo test system finally constructed.

In this system, the distance between the bottom bearing and the top bearing was increased to 90.3 cm due to the length of the cooling chamber and the slip-ring. This long distance led to a rather large axis eccentricity of about 1 mm in the process of assembling the system, and the effect of eccentricity was confirmed in actual exper-

iments. Considering that the shaft diameter of 38 mm and the bearing tolerance is at the level of 30 μm [102], in terms of the absolute size of eccentricity, this is a level that cannot be accepted for actual motor construction and operation. However, in this study to investigate NI applicability, the size of the air-gap was set to 15 mm, and the relative eccentricity was 6.67%. Therefore, it was judged that the effect of the presence or absence of axis eccentricity on the characteristics of the entire motor would not be significant, so the tests were performed. In the actual test, in order to reduce the icing of the test motor surface and to reduce convection heat transfer, temporary walls were additionally built to minimize air circulation around the motor.

5.3.2 Power Supply, Motor Drive System, and Measurement Instruments

This section introduces the power supply, motor drive, and measurement instruments used in the actual experiment. For excitation of the superconductor field winding, Mercury iPS current supply from Oxford Instruments was used (figure 5.11 (a)). The rotating field winding was excited through a slip-ring, and a commercial product was purchased and used (COVIS CSH038).

Figure 5.11: Power supply and motor drive system for the test. (a) Current supply, (b) general-purpose inverter, (c) load motor, and (d) inverter for load motor.

Since the designed test motor is a synchronous motor, a drive system capable of starting of synchronous motor should be established for the characteristic test. As a

starting method of a synchronous motor, there are 1) starting using a low-speed frequency, 2) starting by an external prime mover, and 3) starting by a damper winding [9]. In this study, an inverter coupled with an encoder was used to facilitate motor start-up and speed control, and therefore the starting was performed by gradually increasing the frequency from low speed. A commercial general-purpose inverter (YASKAWA A1000) having synchronous motor operation mode was used for operation (figure 5.11 (b)), and a line-drive type encoder (Autonics E40H12-5000-6-L-5) was coupled with the inverter. The encoder was attached to the encoder shaft located at the bottom of the dynamo test system.

As a load motor, a commercial servo motor system (LS APM-FF30AMK1) was used (figure 5.11 (c) and (d)). The rated capacity of the servo motor is 3 kW at 3000 rpm, and since the test motor operated at a relatively low speed, a 1:6 geared speed reducer is used by coupling with the servo motor for a higher load (>10 Nm).

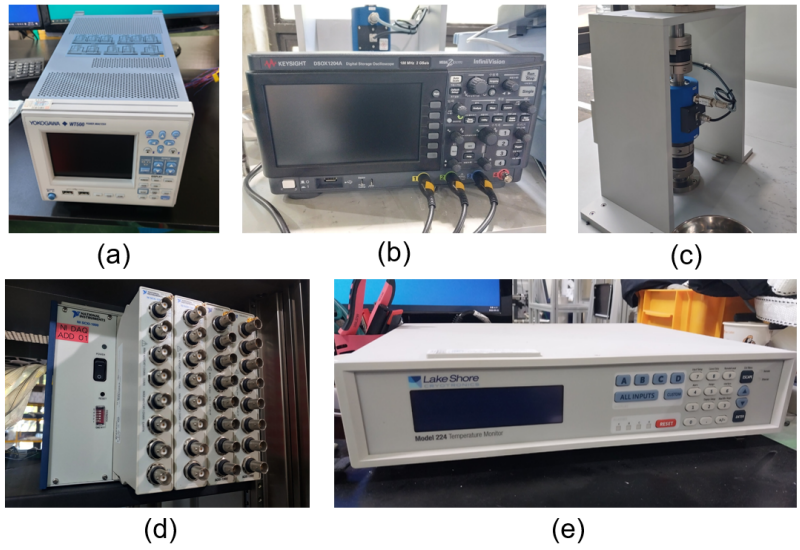

Figure 5.12: Instrumentation for the test: (a) power analyzer, (b) oscilloscope, (c) torque and speed sensor, (d) data acquisition system, and (e) temperature monitor.

Figure 5.12 shows measurement instruments in the test. For the 3-phase current and

voltage measurement of the test motor, a power analyzer (YOKOGAWA WT500) and oscilloscope (Keysight DSOX1204A) were used (figure 5.12 (a) and (b)). Figure 5.12 (c) shows the torque and speed meter (CAS-20KM) for the test. For NI HTS racetrack coils' operating current and voltage measurement, National Instruments' SCXI 1125 data acquisition system was used (figure 5.12 (d)). For measurement of temperatures in the chamber, a temperature monitor (Lakeshore 224) shown in figure 5.12 (e) was used with a silicon diode and platinum temperature sensors (Lakeshore DT-670 and PT-100).

Figure 5.13 shows a picture of the overall test system prepared for the test. During the experiment, each instrument was connected to a computer and the motor status was monitored in real-time.

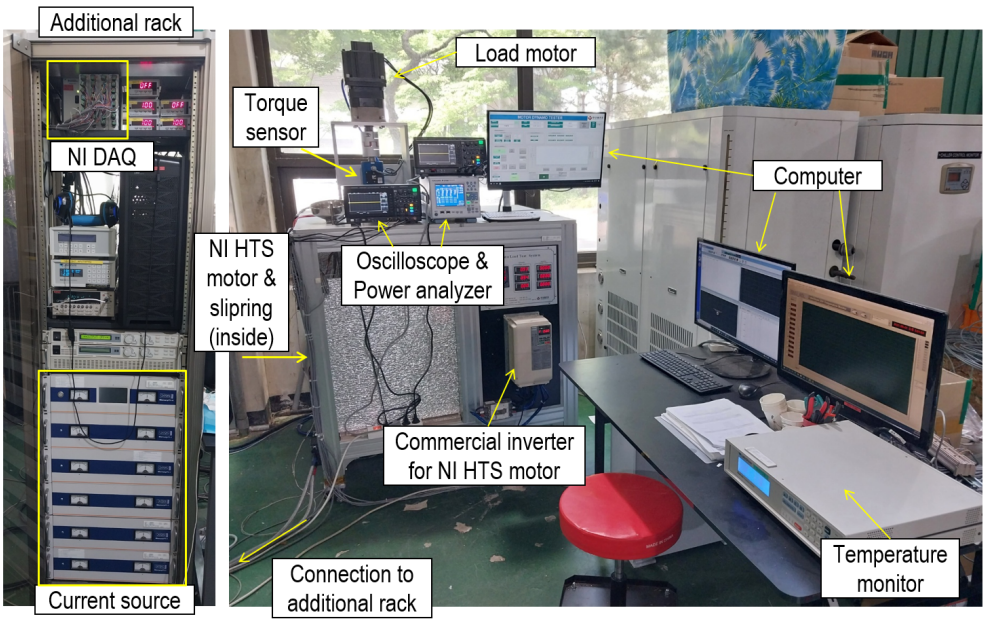

Figure 5.13: A picture of the overall test system.

Chapter 6

EXPERIMENTAL STUDY ON APPLICABILITY OF NI HTS FIELD WINDING TO SUPERCONDUCTING MOTOR

This chapter presents the experimental study on the applicability of the NI technique to the superconducting motor based on the constructed test machine and experiment system, and the major findings are summarized. By analyzing the equivalent circuit model of the NI HTS motor presented above, the NI behaviors expected in motor operation were derived, and experiments were prepared to confirm them. For the systematic analysis, 1) interaction with stator winding is investigated under the stationary situation, and then the test motor was tested 2) in steady-state situations and 3) in transient situations, respectively. First, d-axis current and q-axis current were applied to the stator winding under stationary conditions, respectively, and the response displayed on the NI HTS field winding was analyzed. In the case of steady-state operation, for systematic analysis of the response of the NI HTS field winding, test runs were conducted at various operating points including the target operating point determined in the design process. Is cases of transient operation, the responses of the motor under the acceleration situation and the situation in which external load was suddenly applied were analyzed. Numerical simulations were also performed on each experimental result with

the suggested analysis method, through this, the response characteristics of the NI HTS motor were analyzed, and practical issues identified in the tests when applying NI HTS field winding in actual operation were discussed.

6.1 Overview on Tests: Key Questions, Test Plans, and Test Procedure

6.1.1 Theoretical Expectations Based on Suggested Analysis Model

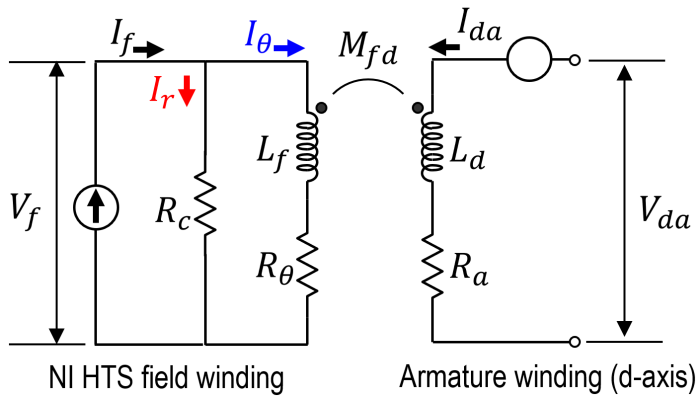

Figure 6.1: Another form of the equivalent circuit of NI HTS test motor in d-axis.

For understanding the concept of the response of NI HTS field winding under motor operation, here, the voltage characteristics were analyzed based on the proposed equivalent circuit first. Figure 6.1 shows another form of the equivalent circuit for the NI HTS motor (figure 3.7) on d-axis. For a better explanation, the previously suggested equivalent circuit is expressed with a mutual inductance instead of a T-equivalent circuit form. In figure 6.1, V_f, V_{da}, I_f, I_r, I_θ, and I_{da} mean voltage of field winding, voltage of armature winding in d-axis, power supply current of the field winding, leak current of NI HTS field winding, and azimuthal current of NI HTS field winding, respectively. L_f, L_d, and M_{fd} are inductance of field winding, inductance of armature winding in d-axis, and mutual inductance between field and armature winding. R_c, R_θ,

and R_a are characteristic resistance, resistance of superconductor, and resistance of armature winding, respectively. Based on the equivalent circuit, The voltage of the field winding (V_f) can be expressed as follows when the flux linkage of the field winding is given as $\lambda_f = L_f I_\theta + M_{fd} I_{da}$.

$$V_f = L_f \frac{d\lambda_f}{dt} + R_\theta I_\theta, \tag{6.1}$$

$$= L_f \frac{dI_\theta}{dt} + M_{fd} \frac{dI_{da}}{dt} + I_\theta \frac{dL_f}{dt} + I_{da} \frac{dM_{fd}}{dt} + R_\theta I_\theta, \tag{6.2}$$

$$V_f = R_c I_r, \tag{6.3}$$

$$I_f = I_\theta + I_r. \tag{6.4}$$

Equations (6.2)–(6.4) represent the expected voltage response from the NI HTS field winding. There are terms that make different voltage responses from the previous stationary stand-alone NI HTS magnet. In the NI HTS magnet, there is no mutual inductance term ($M_{fd} = 0$), and there is no change in inductance according to rotation ($dL_f/dt = 0$), therefore, equation (6.2) is simply arranged as $V_f = L_f \frac{dI_\theta}{dt} + R_\theta I_\theta$. However, in the case of a field winding in a motor, all of the above additional conditions need to be considered, so the equation is given as equation (6.2).

6.1.2 Test Plans and Overall Test Procedure

Test Plans

The circuit analysis shows that there are two main additional considerations in motor operation: 1) the interaction with the armature current ($M_{fd} \frac{dI_{da}}{dt}$), and 2) the change in inductance due to the rotary operation ($I_\theta \frac{dL_f}{dt}$, $I_{da} \frac{dM_{fd}}{dt}$). In order to investigate effectively, the following three tests were planned in this study.

- **Test 1 - stationary operation:** in the situation where the motor does not rotate, after charging the field winding, the response of the NI HTS field winding is measured by applying I_{da} and I_{qa} from the armature winding. This is a test to

confirm the effect of the $M_{fd}\frac{dI_{da}}{dt}$ term under the condition of no inductance variation.

- **Test 2 - steady-state operation:** after charging the field winding, the response of the motor and the NI HTS field winding is measured at a constant speed and a constant load. Through this test, the effect of the inductance variation is investigated under the condition that the armature current is zero or constant.

- **Test 3 - transient operation:** finally, as a test in which the conditions of test 1 and test 2 appear together, the response in transient operation is investigated. The purpose of this study was to confirm the response characteristics that appear in transient driving situations that are commonly seen in motors such as acceleration and load fluctuations.

On the other hand, in the case of NI, since equations (6.3) and (6.4) must be satisfied at the same time, it is clear that the result will be different from that of the insulated (INS) counterpart, which only needs to satisfy equation (6.2). Therefore, a simulation of the INS counterpart considering the experimental conditions was performed and the results were compared.

Overall Test Procedure

The overall experiment was performed in the following order: 1) cool-down, 2) field winding charging, 3) motor operation, 4) field winding discharging, and 5) warm-up. Figure 6.2 shows an example of the overall test procedure (the test performed on 01/27/2022) for the tests. In figure 6.2, (a) shows the temperature measurements at the rotor and the stator, (b) shows the power supply current for the NI HTS field winding, and (c) shows each voltage of the NI HTS racetrack coil during the test, respectively. First, a sufficient cool-down process of the superconducting rotor was performed for more than an hour by pouring LN_2 into the cryogenic chamber (figure 6.2 (a)). After that, the NI HTS field winding was excited to the operating current to be tested by the

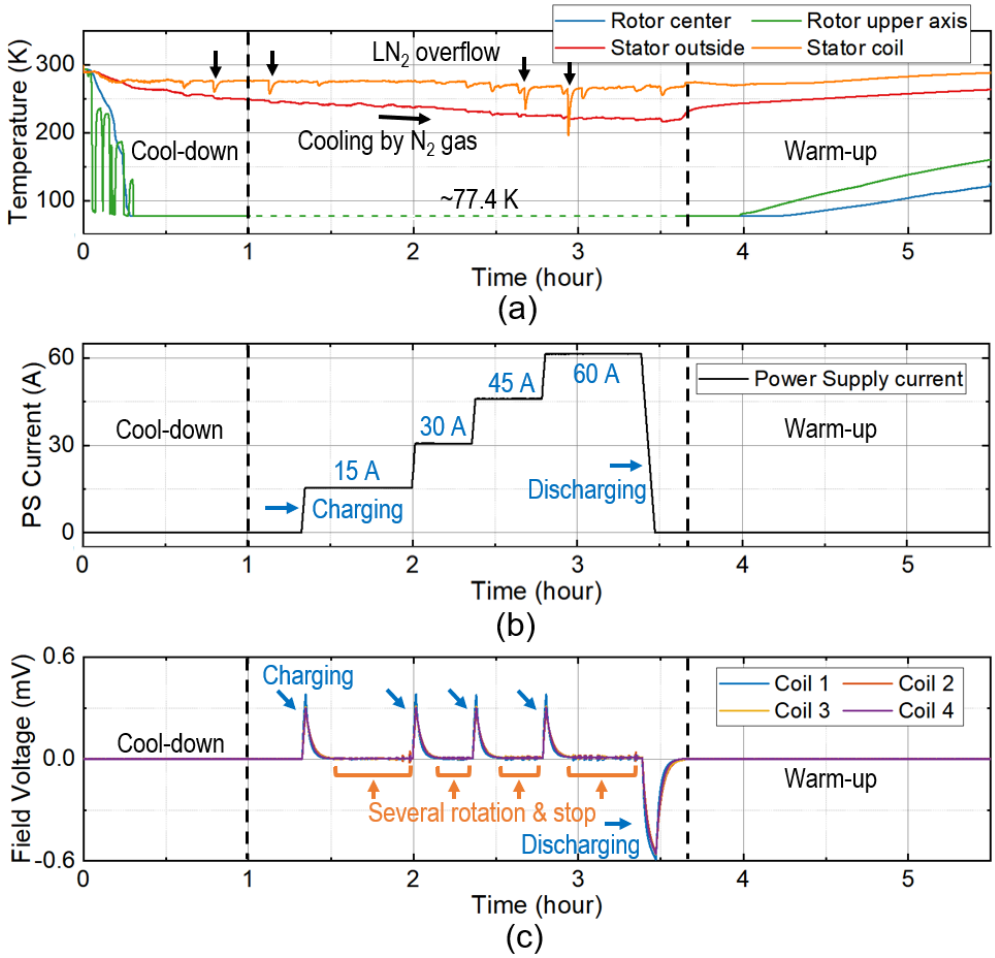

Figure 6.2: An example of the overall test procedure. (a) temperature measurements, (b) power supply current for the field winding, and (c) voltage of each field coil.

current source (figure 6.2 (b)). When their voltage is saturated, with the inverter and dynamo test system, several operation tests are performed under various conditions by changing field winding current (I_f), rotating speed (ω_r), and mechanical load (T_L) (figure 6.2 (c)). The motor is started by slowly increasing the rotating frequency using the inverter and the coupled encoder. During the test procedure, an LN_2 refill was performed intermediately to maintain the cryogenic temperature of the rotor. In the case of the stator, additional cooling was observed by N_2 gas evaporating from the rotor, and its temperature was maintained below 275 K during operation (figure 6.2 (a)). After all necessary tests were performed, NI HTS field winding was fully discharged and a system warm-up was performed. In the case of the warm-up process, it was carried out at room temperature for more than 2 days, so that no water vapor condensing remains inside the rotor.

6.2 Test 1: Interaction Between Stator Winding and NI HTS Field Winding

First, when the motor is stationary and the stator winding current is applied, the response of the motor through the interaction between the NI HTS field winding and the stator winding was investigated through experiments. After charging the rotor to the target operating current, the test was performed by locking the test motor using the load motor so that it does not move. After applying the stator current on d-axis and q-axis separately using a DC power supply, the NI HTS field winding and torque responses were observed, and the characteristics were analyzed.

6.2.1 Experiment Scenarios, Results, and Key Findings

Operation Scenarios

- **1) Response on I_{da} under stationary condition:** to analyze the response characteristics by the stator current, first, the response that appears when the stator

winding current is applied in d-axis is tested. During the test, the test motor was fixed using the position control of the load motor so that the rotor did not move. After charging the NI HTS field winding to 60 A, the voltage of the field winding and generated torque were measured when I_{da} of 24 A was applied using a DC power supply.

- **2) Response on I_{qa} under stationary condition:** next, the response characteristics that appear when I_{qa} is applied to the stator winding were checked. Similarly, after charging the NI HTS field winding to 60 A, the rotor was fixed so that it did not move, and then the voltage of the field winding and generated torque were measured when I_{qa} of 24 A was applied using a DC power supply.

Test Result Applying Armature Current in d-axis

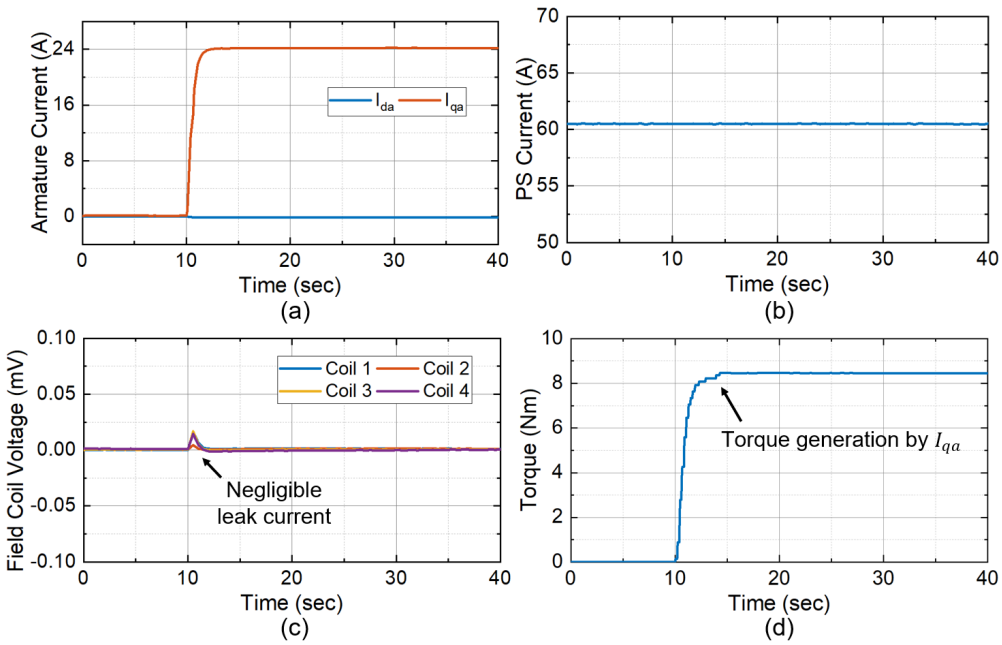

Figure 6.3: Test of NI HTS motor response on I_{da}. (a) Applied I_{da} and I_{qa}, (b) Power supply current for field winding, (c) Field coil voltages, and (d) Torque.

Figure 6.3 shows responses of the test machine when I_{da} is applied by 24 A and I_{qa} is maintained at 0 A (figure 6.3 (a)), when the current of NI HTS field winding is 60 A (figure 6.3 (b)). In the actual experiment, a voltage was applied to the three-phase stator winding using a DC power supply, then measured three-phase currents were converted to the dq-axis to check whether the d-axis and q-axis current were properly applied. Figure 6.3 (c) shows the voltage of coil 1–coil 4, and figure 6.3 (d) shows the measured torque by the torque sensor. The experimental results show a similar tendency to the simulation results presented in "Analysis on Interaction with Stator Winding" in section 4.1.3. As I_{da} was applied, the voltage was induced in the field winding, and it was found that it decreased gradually according to the rate of individual charging time constant values. This result shows that leak currents have occurred in the NI HTS field winding. Also, it was confirmed that the induced voltages were different depending on the contact resistivity of each coil. In the case of torque, no distinct value was measured, implying that the current was well applied in the d-axis direction.

Test Result Applying Armature Current in q-axis

Next, under the same condition, instead of I_{da}, I_{qa} was instantaneously applied by 24 A through the DC power supply (figure 4.6 (a)). A slight voltage spike was observed in the field coils, but compared to the I_{da} case, the magnitude was negligible, and the voltage saturation tendency was not observed. On the other hand, in the case of torque, it was possible to measure a torque proportional to the value of I_{qa} through the torque sensor without any problems such as leakage current.

Key Findings in Stationary Operation

The key findings in stationary operation are summarized as follows.

- **Key finding 1:** it was experimentally confirmed that the response of NI HTS field winding and torque differed according to the direction of the current flow-

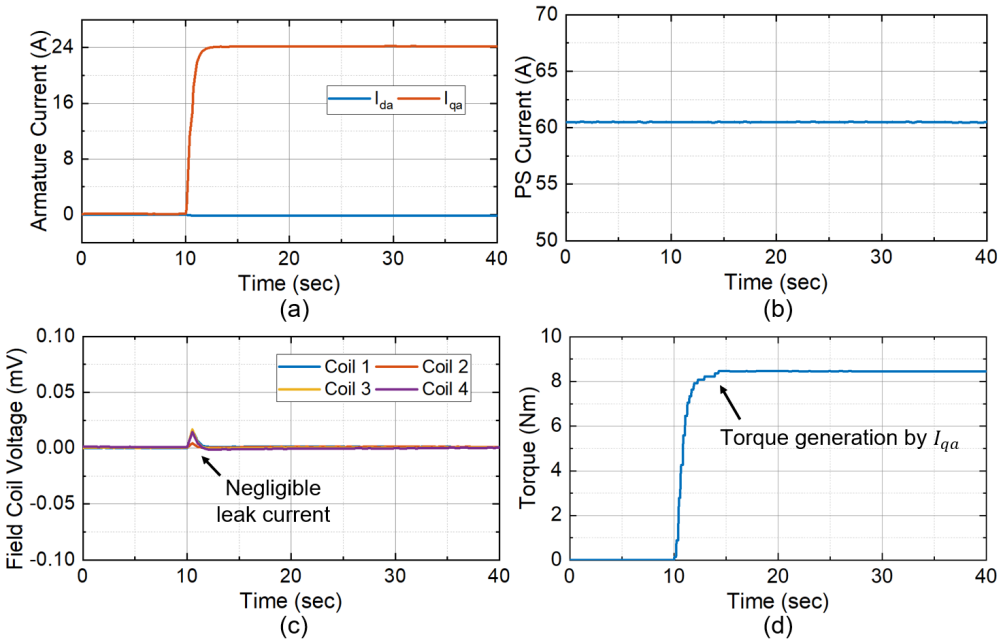

Figure 6.4: Test of NI HTS motor response on I_{qa}. (a) Applied I_{da} and I_{qa}, (b) Power supply current for field winding, (c) Field coil voltages, and (d) Torque.

ing through the stator. In the case of d-axis current, contributing to the rotor flux, its variation creates a leak current in the NI HTS field winding at the same time.

- **Key finding 2:** even if the q-axis current flows in the stator winding, the NI HTS field winding is almost unaffected, and it is confirmed that torque is generated like an insulated counterpart without leakage current.

6.2.2 Detailed Analysis on Response of NI HTS Field Winding

The responses observed through the test are the results consistent with the FEM simulation results expected in section 4.1.3 and can be explained through the circuit analysis suggested in this chapter. In the circuit equation of the previous NI HTS field winding, by canceling the component due to inductance variation, the following equations can be applied for this test is given.

$$V_f = L_f \frac{dI_\theta}{dt} + M_{fd} \frac{dI_{da}}{dt} + R_\theta I_\theta, \tag{6.5}$$

$$V_f = R_c I_r, \tag{6.6}$$

$$I_f = I_\theta + I_r. \tag{6.7}$$

Basically, it can be expected through the circuit equation that the response of NI HTS field winding is affected by a change of I_{da}, but not by I_{qa}, and such results have been shown in simulations and experiments. In addition, the result that I_{qa} contributing to torque generation does not affect the leak current suggests that torque control of a superconducting motor to which NI HTS field winding is applied is possible without problems.

Finally, considering the actual experimental conditions including the difference in contact resistivity (R_{ct}) for each coil, the same simulation performed in section 4.1.3 was performed again, and the results were compared with the experimental results. Figure 6.5 (a) and (b) show the simulated voltage of the NI HTS field winding and torque when I_{da} is applied, and (c) and (d) are the simulation results when I_{qa} is

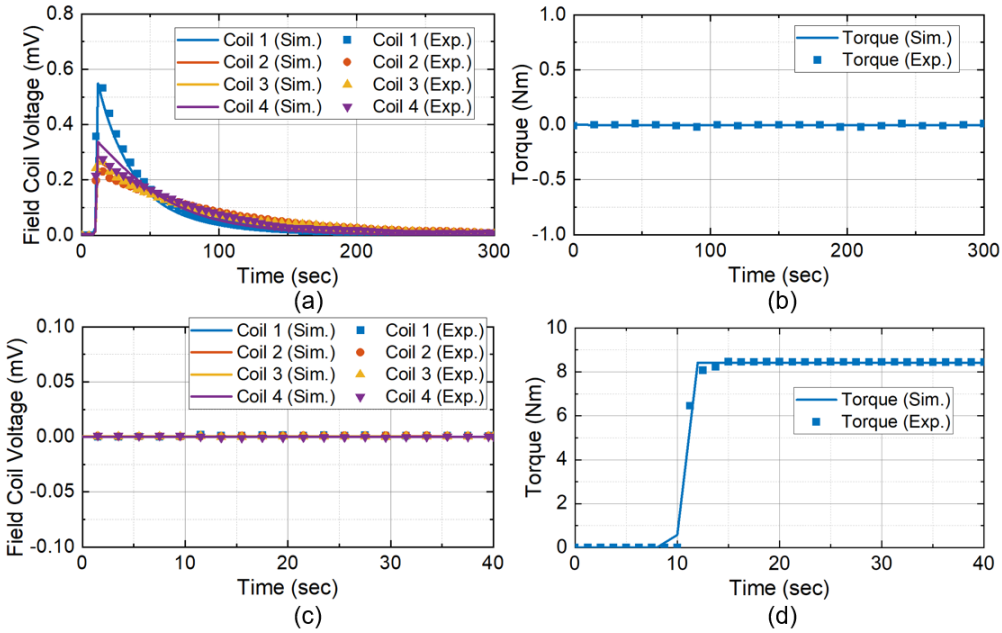

Figure 6.5: Comparison between simulation and experiment of stationary tests. (a) Field coil voltages induced by I_{da}, (b) Torque induced by I_{da}, (c) Field coil voltages induced by I_{qa}, (d) Torque induced by I_{qa}.

applied. Although the peak value of the voltages induced in the NI HTS field winding is slightly different, the difference in voltage magnitude according to the difference in R_{ct} in the test was well reproduced in the simulation. Also, it was found that the presence or absence of torque according to the presence or absence of I_{qa} was well interpreted.

In the case of the analysis of the difference between NI and INS, the obtained trend was exactly the same as the simulation performed in section 4.1.3, so it was not added to this section.

6.3 Test 2: Steady-state Operation Characteristics of NI HTS Test Machine

Next, the NI HTS test motor was operated under various steady-state operation conditions. Here, the "steady-state" is defined as a situation in which measurement signals of rotating speed (ω_r), torque (T_e), phase voltage of armature winding (V_a), line current of armature winding (I_a), and NI HTS coil's voltage (V_f) are saturated. Since I_a is saturated, as a result, the response characteristics according to the inductance variation can be observed. Including the operation test at the target operating point, experiments were conducted at various operating points to systematically analyze the characteristics.

6.3.1 Selected Experiment Results and Key Findings

Tested Operation Points for Steady-state Operation

- **1) Back EMF measurement tests:** as a systematic analysis of motor performance and NI behavior, the back EMF of the motor was measured at different operating points. Changing ω_r from 60 to 300 rpm, and I_f from 15 to 66.2 A, the back EMF and the voltage response of NI HTS racetrack coils were measured. Through the back EMF test, the response of the NI HTS field winding in

the absence of armature current (I_a) was investigated.

- **2) Additional load operation tests:** finally, by performing the test changing the external load, the influence from the constant I_a was examined. At the same speed (ω_r = 120 rpm) and the same field winding current (I_f = 60 A), the mechanical load was applied at 0(no-load), 2, 4, and 6 Nm.

- **3) Test at target operating point:** at the target operating point (I_f = 66.2 A, ω_r = 300 rpm, and T_e = 15.9 Nm), the performance of the motor with NI HTS field winding was investigated. This test was carried out for the purpose of checking whether it works well without serious problems due to NI behavior at the design point.

Steady-state Operation 1: Back EMF Measurement Tests

First, back EMF was measured at various operating points and the results were investigated. Figure 6.6 (a) shows the magnitude of the back EMF according to rotating speed (ω_r) and current of field winding (I_f). Back EMF is proportional to the change in flux linkage of the stator winding, so before the iron core of the stator is saturated, the back EMF increases in proportion to I_f and ω_r in principle. This trend was well observed in the experiment. Overall, experiment results showed about 8.90% higher value than the simulation results. The difference between the simulations and the experiments seems to come from the error of end-effect estimation in the simulation. Figure 6.6 (b) shows the back EMF waveform measured at the target current (I_f = 66.2 A) and rotating speed (ω_r = 300 rpm). The overall waveform shape of the experiment (solid lines) and simulation (dashed lines) was roughly consistent, but in the case of the actual experiment, the fundamental component was more dominant (figure 6.6 (c)), and accordingly the RMS value also appeared larger in the experiment. Total harmonic distortion (THD) was calculated to be 1.54% and 4.40% in the experiment and simulation, respectively. For the NI response, voltage ripples with a specific ten-

dency were observed. This will be discussed in a later section along with the voltage response in other steady-state operations.

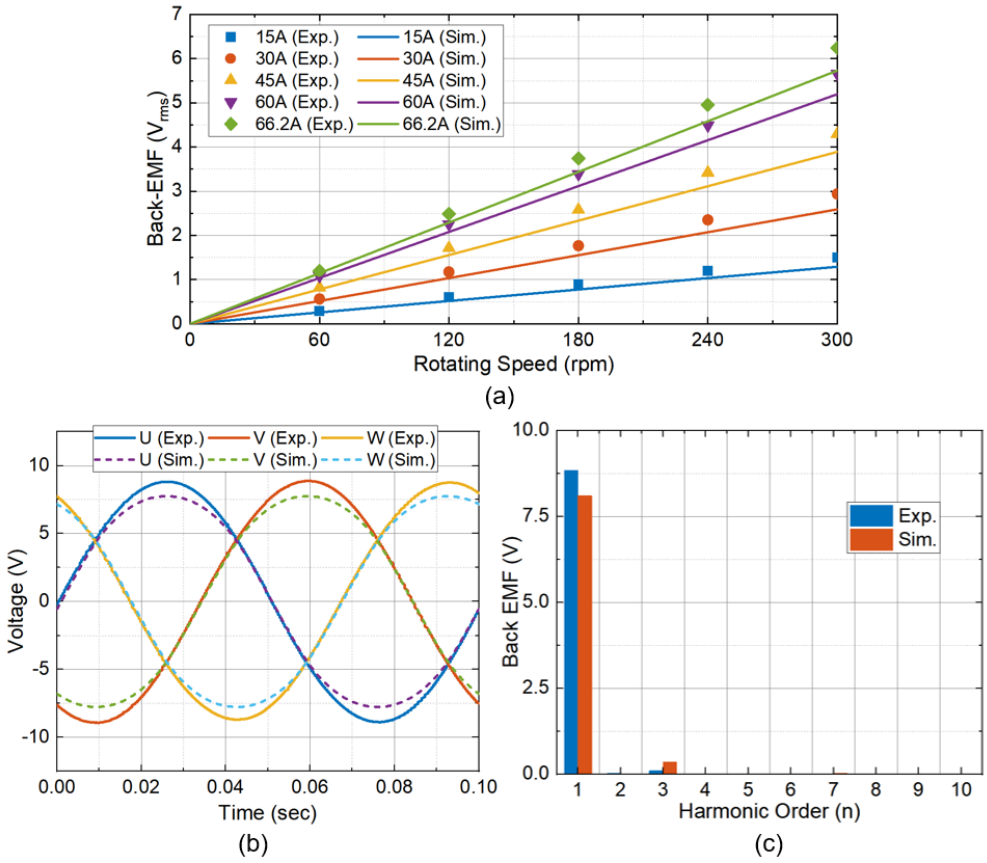

Figure 6.6: (a) Back EMF according to ω_r and I_f, (b) Back EMF when I_f = 66.2 A, ω_r = 300 rpm, and (c) Harmonic analysis result when I_f = 66.2 A, ω_r = 300 rpm.

Steady-state Operation 2: Load Operation Tests

The operation test was performed by changing the external load this time. Table. 6.1 shows comparisons of phase voltage (V_a) and line current (I_a) measured at selected operation points. When I_f = 60 A and ω_r = 120 rpm, the test motor was operated using the inverter with an external load of no-load, 2 Nm, 4 Nm, and 6 Nm. Even at

no-load operation, about 1.27 A_{rms} of line current was required. It implies that additional line current originated from mechanical friction or tuning error in a commercial inverter. The average magnitude of the friction coefficient was estimated to be about 0.0201 Nm/(rad/s). As the size of the load increased, the relative effect of the friction decreased, and the relative portion of the armature current was induced for the load torque increased, therefore the error between the experiment and the simulation gradually decreased (45.8% with 2 Nm, and 22.7% with 6 Nm). In operation at the actual target operating point, the error was 9.69%. In the case of phase voltage, the error between simulation and experiment was around 10%, and it should decrease as the error of line current decreases, but it was difficult to identify a clear trend in the results of this experiment. This is thought to be because the resistance of the stator coil changed due to cooling by N_2 gas. Unfortunately, the temperature of the stator coil for the experiments performed in table 6.1 was not measured, so the associated analysis is not included here. The NI response with a specific trend was observed in the load operation as in the back EMF test, and this will be discussed in together later section.

Table 6.1: Load Operation Results with I_f = 60 A at ω_r = 120 rpm

Parameters	**No-load**		**2 Nm**		**4 Nm**		**6 Nm**	
	Exp.	**Sim.**	**Exp.**	**Sim.**	**Exp.**	**Sim.**	**Exp.**	**Sim.**
Line current	1.27	0	6.46	3.50	9.70	7.18	14.1	10.9
Phase voltage	2.46	2.27	3.30	2.83	3.82	3.43	4.53	4.02

Steady-state Operation 3: Operation at the Target Operating Point

Figure 6.7 shows the experiment result at the target operation point (I_f = 66.2 A, ω_r = 300 rpm, and T_e = 15.9 Nm). First, the test motor accelerated to a target speed of 300 rpm, and then an external load was gradually applied to the target torque of 15.9 Nm using the load motor. Since the speed reducer was connected to the load motor

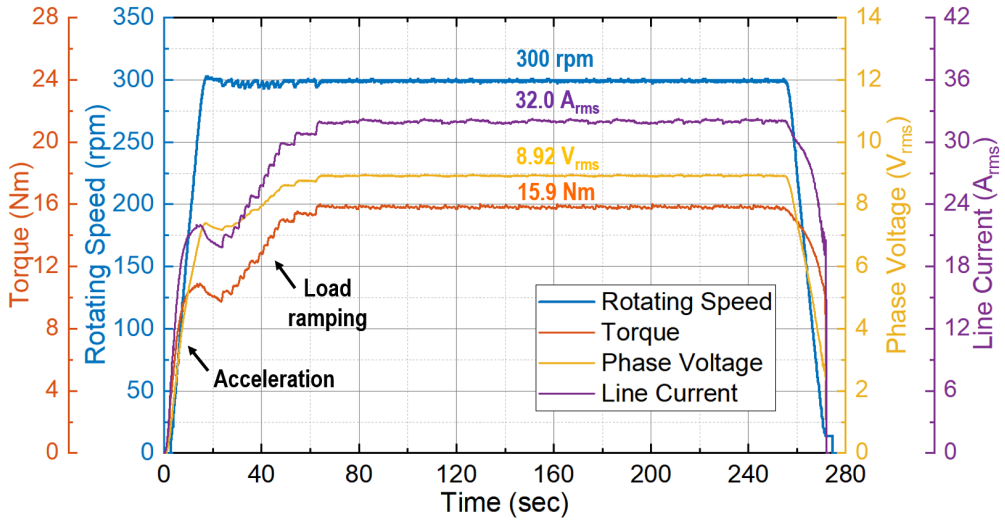

Figure 6.7: Experiment at the target operating point.

to make the required torque, the additional mechanical load was detected due to the friction in the speed reducer during acceleration. When mechanical values reach the target point (ω_r = 300 rpm and T_e = 15.9 Nm), the RMS values of the phase voltage and line current of the armature coil were measured through the power analyzer. As a result, an additional line current of 3.10 A_{rms} was identified compared to the rated line current (28.9 A_{rms}) in the simulation. This current difference seems to be induced by mechanical friction and not-optimized inverter tuning. In the case of the phase voltage, the measured value was 0.31 V_{rms} lower than the simulation despite the presence of an additional line current. It seems that one of the reasons for this difference was that the stator coil was cooled to a level of 260 K lower than room temperature by N_2 gas (phase resistance is changed from 0.121 Ω at 300 K to 0.0838 Ω at 260 K). Accordingly, the Joule loss was decreased, and the input power at the same output torque was rather decreased in the experiment. It needs to be noted that this is not a general situation that occurs in superconducting motors, and it is because of the special structure of the cooling system applied in this study. In the case of the torque ripple, it was difficult to accurately measure the tendency with the torque sensor used in the experiment. It

is because the peak-to-peak torque value was estimated at a small level of 0.183 Nm in the simulation, the fluctuation of the torque due to mechanical friction or vibration could be larger than that of the torque ripple. The tested motor was stopped after about 3 minutes of rotation at the target operating point. Critical problems by NI behavior in operation could not be identified.

Response of NI HTS Field Winding in Steady-state Operations

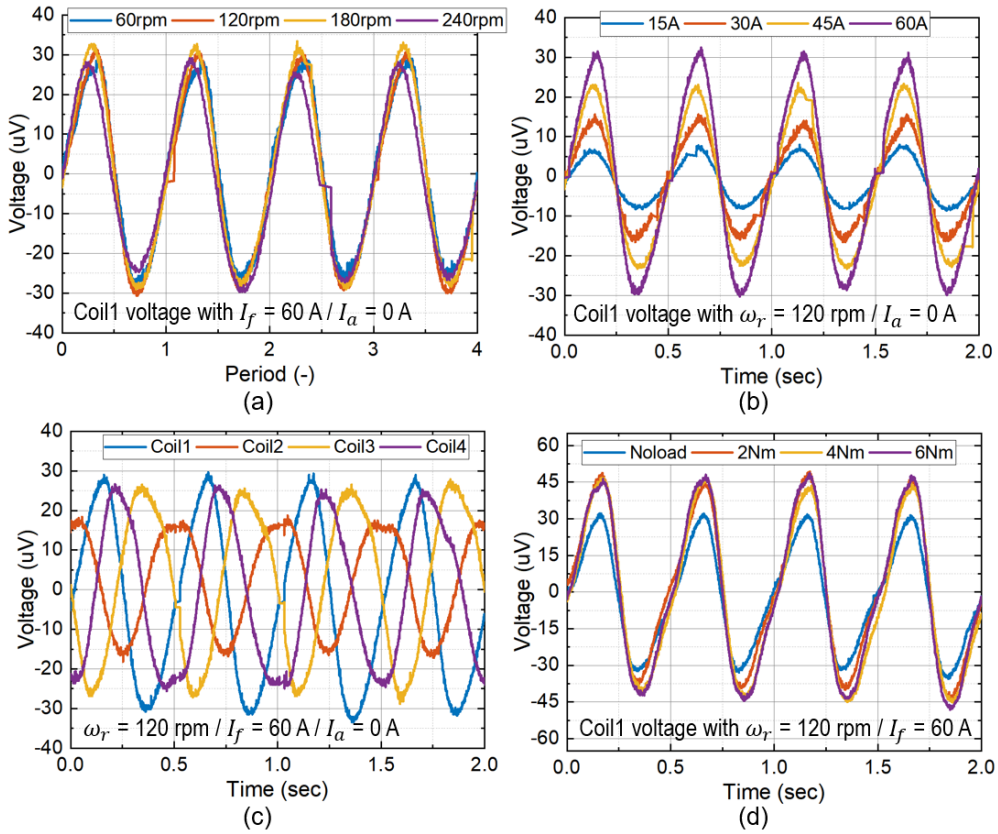

Figure 6.8: NI HTS field coil voltage in steady-state experiment. (a) Voltage according to ω_r, (b) Voltage according to I_f, (c) Voltage of each coil, and (d) Voltage according to the external load difference.

In the case of the steady-state response of the NI HTS field coil, periodic voltage

ripples of several tens of μV level appeared, which were not identified in simulation under ideal conditions (figure 4.9 in section 4.1.3). These corresponded to the current ripple of $\sim$1 A based on the azimuthal current (I_θ) of NI HTS field winding, and turn-to-turn loss of $\sim$240 μW. To analyze the characteristics of the periodic ripple response, voltage ripple data were collected and compared as shown in figure 6.8. In figure 6.8, the NI HTS field coil's responses shown in (a)–(c) are from the back EMF measurement tests, and (d) from the additional load tests. (a) shows the voltage response of coil 1 with different ω_r according to the period (x-axis) when I_f = 60 A, and (b) is the voltage response of coil 1 with different I_f when ω_r = 120 rpm. Through figure 6.8 (a) and (b), it can be seen that this voltage ripple occurs in the same period as the rotating speed ω_r. And the magnitude of the ripple is proportional to I_f, but there is no clear correlation with ω_r. (c) shows the voltage response of coil 1–coil 4 with different contact resistance when I_f = 60 A and ω_r = 120 rpm. This graph shows that these ripples appear in proportion to the size of the contact resistance. Finally, (d) shows the voltage response of coil 1 according to the size of the external load, that is, the size of the armature current (I_a) when I_f and ω_r are the same. Even when the external load was increased from zero to 6 Nm, the size of the ripple did not show a specific trend. It seems that the difference in ripple size occurred between the no-load test and 2-6 Nm tests, but it is presumed that there is a change of R_{ct} between these tests, which were conducted on different dates, due to repeated charging and repeated cooling [103]. This is further discussed in the later potential problem section (section 6.5.2).

Key Findings in Steady-state Operation

- **Key finding 1:** even with NI HTS field winding, the test machine did not show any critical problems in acceleration and torque generation. However, additional line current was induced by the friction of the test system and problems with inverter tuning (figure 6.7).

- **Key finding 2:** in the case of the response of NI HTS field winding, periodic ripples appeared. The period of the fundamental component of the ripple coincided with the mechanical rotational speed of the motor. However, the peak-to-peak value of the ripple does not increase in proportion to the rotational speed of the motor (figure 6.8 (a)).

- **Key finding 3:** as the excitation current of the NI HTS field winding increases, the peak-to-peak value of the ripple tends to increase proportionally (figure 6.8 (b)).

- **Key finding 4:** there was a difference in the peak-to-peak ripple value of each coil, and as R_{ct} of the coil increased, the ripple size also tended to increase (figure 6.8 (c)).

- **Key finding 5:** although the armature current increased, the change in the peak-to-peak value of ripple was found to be insignificant (figure 6.8 (d)).

6.3.2 Detailed Analysis on Ripple Response of NI HTS Field Winding

In this section, the causes and characteristics of the ripple response of the NI HTS field winding were analyzed, and the effect on the actual motor operation is discussed.

Analysis on Source of Voltage Ripple Considering Test Conditions

Looking at the experimental results, the ripple response was also shown in the back EMF measurement experiment in which the inverter did not operate (figure. 6.8 (a)–(c)). Considering the back EMF measurement test situation, the armature current is zero ($I_{da} = 0$), so equation (6.2) is simplified as follows.

$$V_f = L_f \frac{dI_\theta}{dt} + I_\theta \frac{dL_f}{dt} + R_\theta I_\theta. \tag{6.8}$$

Under ideal conditions, $R_\theta = 0$, so it is simply arranged as $V_f = L_f \frac{dI_\theta}{dt} + I_\theta \frac{dL_f}{dt}$. It implies $\frac{dL_f}{dt}$ can become the main source of identified ripple voltages. Also, the

frequency of V_f can be given the same as the frequency of L_f. In an NI HTS field winding, equations (6.3)–(6.4) are needed to be satisfied too, so equation (6.8) can be reorganized on V_f as follows.

$$\frac{dV_f}{dt} + \frac{1}{L_f}\left(\frac{dL_f}{dt} + R_c\right)V_f - \frac{R_c I_f}{L_f}\frac{dL_f}{dt} = 0. \tag{6.9}$$

On the other hand, in the case of the insulated field winding, V_f is simply given as equation (6.10) because $I_\theta = I_f$ and I_f is controlled to be constant by the power supply (current source).

$$V_f = I_f \frac{dL_f}{dt}. \tag{6.10}$$

Equation 6.9 has a completely different form from its insulated counterpart, thus it means that NI HTS field winding will show different behavior compared to its insulated counterpart. Because the voltage equation is given as a differential equation for V_f, it is difficult to simply determine how each parameter affects V_f. However, the frequency of V_f is determined according to the frequency of L_f as well, by performing harmonic component analysis by Fast Fourier transform (FFT) on V_f, potential sources that generate the voltage ripple like the actual experimental results can be traced.

In figure 6.9 (d), the blue column shows the FFT result of V_f with respect to the mechanical rotation frequency when I_f = 60 A and ω_r = 120 rpm. The fundamental component (28.3 μV), which coincides with the rotating speed, is most dominant overall, then 2^{nd} (4.59 μV), 3^{rd} (0.644 μV), 5^{th} (0.310 μV), and 6^{th} (0.280 μV) harmonic components were followed in order. THD was 26.6%. The constructed test motor has an air-cored rotor structure and a large air-gap, so the fluctuation of L_f is not large enough to cause such a ripple size in analysis, and the period also does not coincide with the rotation period (figure 4.9). Therefore, additional conditions occurring in the experiment that could cause such inductance fluctuations were considered.

There are various sources that can generate ripples in electric machines: magnetic sources (slot harmonics, core saturation, etc.), mechanical sources (static & dynamic eccentricity, bearing, balancing, etc.), aerodynamic sources (noise from a cool-

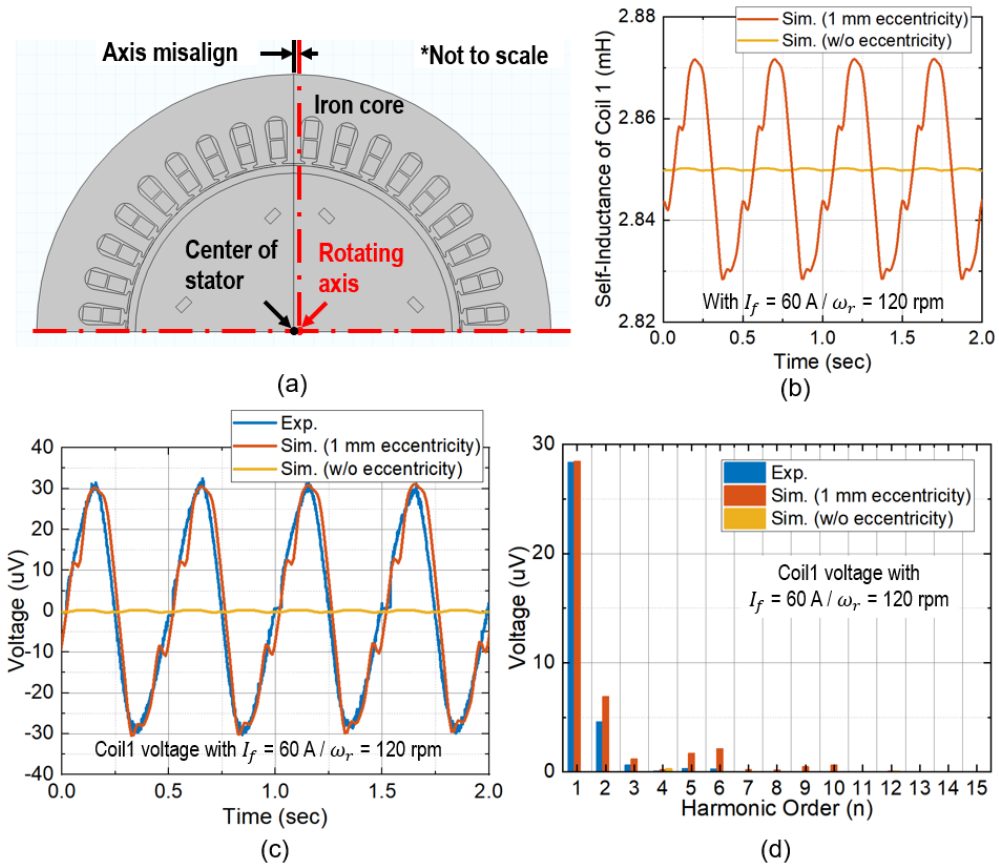

Figure 6.9: Simulation results considering potential ripple source. (a) Concept of static eccentricity, (b) Self-inductance variation with 1 mm of eccentricity, (c) Voltage ripples in experiment and simulations, and (d) FFT result of the coil voltage.

ing duct, etc.), and electronic sources (switching harmonics) [104–106]. In that the low-frequency components (fundamental and 2^{nd} order harmonic) mainly occurred in the test, the voltage response shown in this experiment is thought to be mainly induced by mechanical reasons [106]. Therefore, the change in L_f due to "static eccentricity" is considered to be the main cause in the simulation in that the fundamental component consistent with the rotating speed was dominant in the voltage ripple (figure 6.9 (a)). As explained in the previous construction process (section 5.3.1), this is thought to be due to a manufacturing error that occurred during the system assembly process as the spacing between the bearings supporting the test motor increased.

Figure 6.9 (b) shows the change in L_f in the conventional simulation without eccentricity and the simulation considering 1 mm of eccentricity. It can be confirmed that the change in L_f coincides with the rotating speed expected through the circuit model, and accordingly, it is possible to reproduce the overall shape of the voltage ripple shown in the experiment as shown in figure 6.9 (c). In figure 6.9 (d), simulation results and experimental results are compared through FFT. It was confirmed that the trend in which the fundamental component and the 2^{nd} component appeared dominant was consistent with the experiment, and the 3^{rd}, 5^{th}, and 6^{th} components also appeared as experiments.

As expected from equation (6.2), when I_{da} is taken into account, the behavior of the NI HTS field coil is predicted to be more complex. However, as can be seen in figure 6.8 (d), the effect of I_{da} in steady-state tests was rather insignificant. This is presumed to be due to the following reasons: 1) since it is steady-state, $\frac{dI_{da}}{dt} = 0$, and 2) I_{da} is basically controlled to be zero in ideal for maximum torque generation in the air-cored motor.

Comparison between Experiment and Simulation

Although this eccentricity originates from the mechanical error of the experimental system, it affects the electromagnetic parameter (figure 6.9 (b)), which indicates that

it affects the NI response. When eccentricity was considered as a ripple source, simulations with the suggested analysis model were performed to confirm whether the same trends as the key findings identified in figure 6.8 appeared. The magnitude of eccentricity was determined to be 1 mm, by finding the point that coincided with the peak voltage of V_f, and the relative eccentricity (= eccentricity displacement/magnetic air-gap) was 6.67% [107].

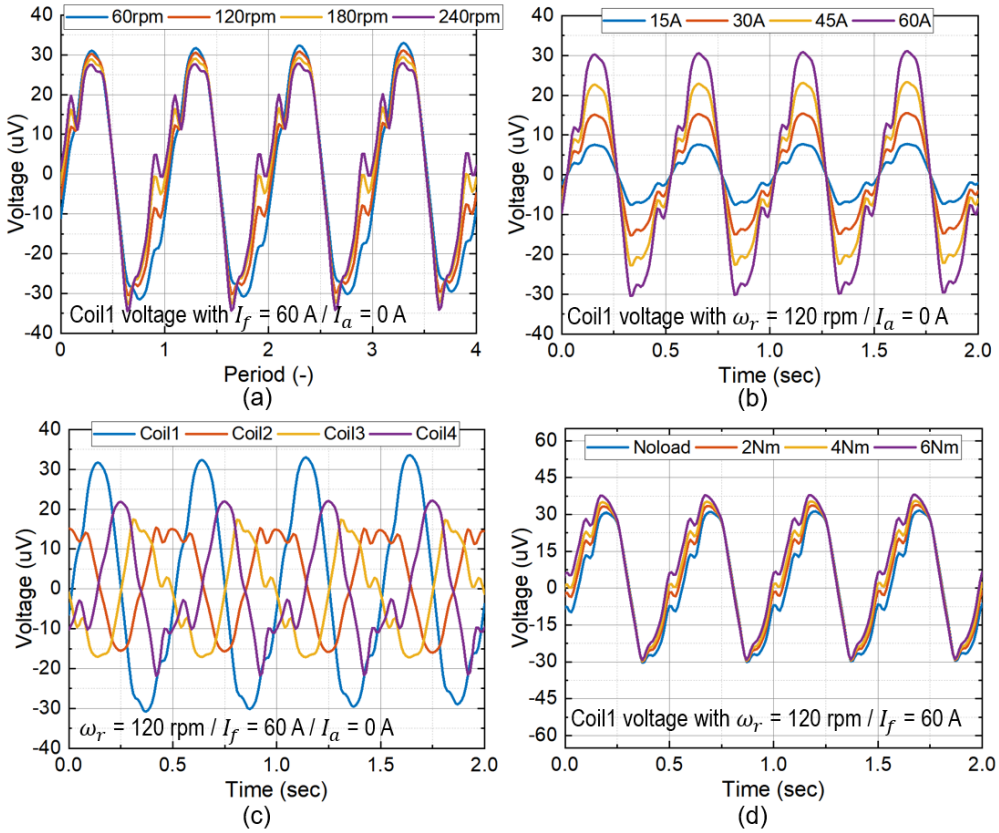

Figure 6.10: NI HTS field coil voltage in simulation considering eccentricity. (a) Voltage according to ω_r, (b) Voltage according to I_f, (c) Voltage of each coil, and (d) Voltage according to the external load difference.

Figure 6.10 shows the NI HTS field coil voltage in simulation considering eccentricity. As in figure 6.8, (a) shows V_f of coil 1 according to ω_r, (b) shows V_f of coil

1 according to I_f, (c) shows V_f for each coil, and (d) shows V_f of coil 1 according to external load difference. Simulations considering eccentricity could reproduce the experiment results overall. In (a), the periodic ripple frequency consistent with the mechanical rotation frequency and the trend of the ripple magnitude could be confirmed as in the experiment (*key finding 2*). In (b), it was confirmed that the peak-to-peak magnitude of the ripple increased as the excitation current increased (*key finding 3*). In (c), it was possible to confirm the difference in ripple magnitude according to the R_{ct} (*key finding 4*). Finally, in (d), there was a change in ripple according to the increase of armature current, but the difference was insignificant (*key finding 5*).

Comparison between NI and INS Considering Experiment Conditions

An additional simulation was conducted on what kind of response the insulated counterpart would show when there is an inductance variation source such as the eccentricity of the axis (figure 6.11). The first thing to note is that, in the case of NI, a ripple signal of several tens of μV appeared, but in the case of INS, a more noisy ripple signal of several tens of mV appeared. Also, in the case of NI, there was no increase in the ripple size according to the increase in the rotation speed, but in the case of the INS, the ripple size also increased as the rotation speed increased (figure 6.11 (a)). The tendency that ripple size is proportional to the field winding current was the same in INS (figure 6.11 (b)). In the case of NI HTS field winding, a signal proportional to the size of R_{ct} appeared, but in the case of INS, the difference could not be confirmed because insulation conditions were the same for all coils (figure 6.11 (c)). Finally, a similar tendency that the ripple response did not change significantly with increasing external load was observed also in INS (figure 6.11 (d)).

Discussion on Experiment and Simulation Results in Steady-state Operation

The experiment and analysis results indicate that ripple leak current may occur in the NI HTS field winding due to inductance variation. Inductance variations can be

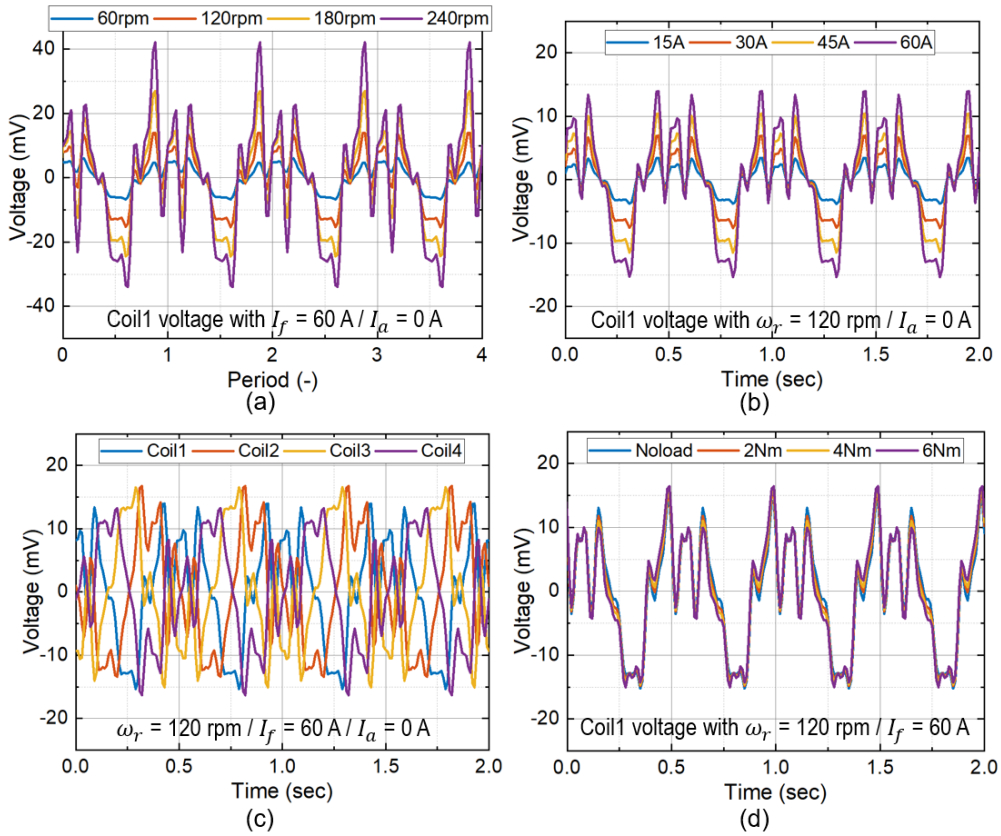

Figure 6.11: Insulated field coil voltage in simulation considering eccentricity. (a) Voltage according to ω_r, (b) Voltage according to I_f, (c) Voltage of each coil, and (d) Voltage according to the external load difference.

induced by practical reasons such as a manufacturing error or vibration during motor operation. In this study, this voltage ripple was explained to some extent when the static eccentricity was considered, but this can be a special situation for the test motor constructed in this study. It is necessary to collect various experimental data under different designs and experimental conditions. However, since inductance variation can appear in electric machines in various forms, this ripple phenomenon of the NI HTS field winding is expected to appear in any form.

6.4 Test 3: Transient Operation Characteristics of NI HTS Test Machine

Finally, in order to comprehensively analyze the features identified in the previous experiments, transient conditions were tested, and operation characteristics were observed and analyzed. In transient operation, it is expected that the turn-to-turn leak current of the NI HTS field winding is inevitably induced through the ideal simulation performed in section 4.1.3. In the simulation, the magnitude of leak current and its effect is rather insignificant, however, as in the above steady-state situation, additional effects from the test system can be observed, so an experimental investigation is required on how much of this leak current occurs and how much of the effect on the motor operation is in practice.

Basically, all operation situations except steady-state operation can be regarded as transient operations and various transient operations were tested, but in this study, the test results of the “sudden load operation,” which showed the clear NI behavior in transient operation conditions, and analyses on them are presented.

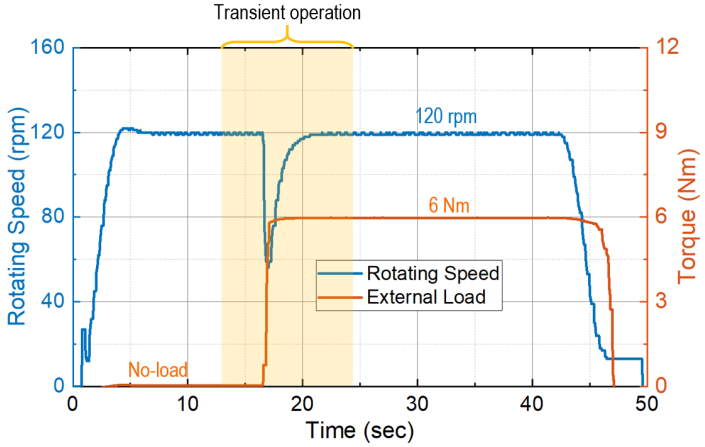

Figure 6.12: Tested transient operation scenario. External load is suddenly applied during no-load operation.

6.4.1 Experiment Scenarios, Results, and Key Findings

Operation Scenario for Transient Operation

Figure 6.12 shows the selected transient operation scenario in this study. In order to examine the transient characteristics, the situation when a sudden external load of 6 Nm was applied in the situation of driving at a constant speed (120 rpm) with no-load was tested (figure 6.12). It needs to be noted that for speed control of the test motor, a commercial inverter was used with the encoder (figure 5.11). The correction factor of motor position estimation through the encoder is manually tuned to prevent potential damage to the system from the inverter's auto-tuning process. PI feedback control is used for speed control of the motor, and as feedback gains of P and I, 10 and 1 sec were used respectively, which are recommended ranges in the inverter's manual.

Test Result of Selected Transient Operation

Figure 6.13 shows the sudden load operation test results. Figure 6.13 (a) shows the change of the external load, the rotating speed, and RMS values of V_a and I_a in the

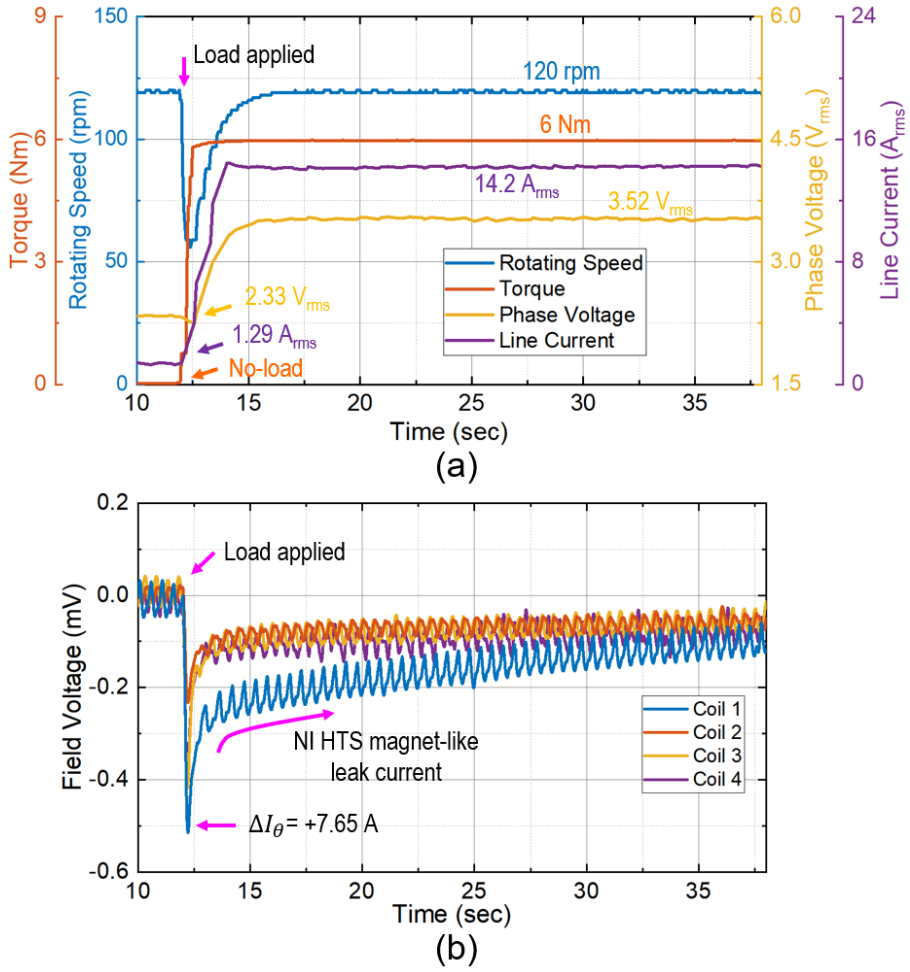

Figure 6.13: Sudden load experiment result. (a) Rotating speed, torque, phase voltage, and line current, (b) Voltage response of NI HTS field winding.

stator coil. As the external load of 6 Nm was applied, the rotational speed momentarily decreased to about 60 rpm, but soon recovered to 120 rpm as an additional I_a was injected. I_a increased to 14.2 A_{rms}, and it was found that the voltage increased to 3.52 V_{rms} due to the resistance in the stator coil.

Figure 6.13 (b) shows V_f profile in this transient situation. It was found that the two different types of response were combined, that is, the periodic ripple and the leak current were observed together during transient operation. The periodic ripple, which could be confirmed in steady-state operation, again appeared because the same manufacturing error exists in the system. The leak current seems to be occurred along with the rapid increment of the d-axis stator current ($\frac{dI_{da}}{dt}$), and it can be seen that V_f saturation occurs. The maximum difference in I_θ was estimated to be +7.65 A based on coil 1. It was found that the generated leak current gradually decreased according to the time constant of each NI HTS racetrack coil.

Key Findings in Transient Operation

The key findings in transient operation are summarized as follows.

- **Key finding 1:** the NI response combined with the leak current and periodic ripple confirmed in the previous stationary test and steady-state test, respectively, was observed.
- **Key finding 2:** the leak current seems to be caused by the occurrence of $\frac{dI_{da}}{dt}$ components according to the change of I_a during acceleration or load change.

6.4.2 Detailed Analysis on Transient Behavior of NI HTS Field Winding

In the transient experiment, it was confirmed that the voltage response and leak current of the NI HTS field winding were much larger compared to the ideal transient simulation performed in "Transient Operation Analysis" in section 4.1.3.

Additional Effect from Experimental Conditions

The main cause of this difference seems to be the presence or absence of a d-axis armature current (I_{da}) that affects the flux linkage of the NI HTS field winding identified in the stationary test. In the simulation, armature current was controlled to be $I_{da} = 0$, but in the actual experiment, I_{da} seemed to be induced by an error in inverter tuning. That is, the q-axis of the rotor did not exactly coincide with the rotating magnetic field generated by the stator coil (i.e., $I_a = \sqrt{I_{da}^2 + I_{qa}^2}$, $I_{da} \neq 0$). Figure 6.14 is a schematic to roughly explain this mechanism, and shows the possible situations on NI HTS field winding by the direction of the rotating magnetic field and the dq-axis of the rotor.

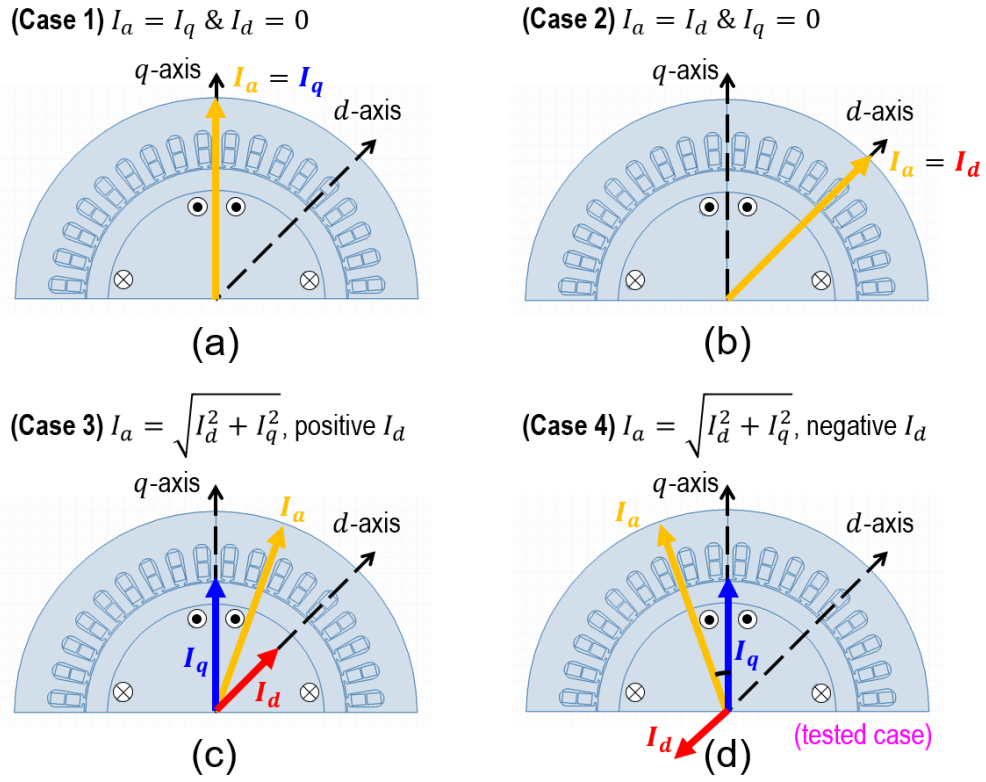

Figure 6.14: Four possible cases of stator current control in tests.

- **Case 1) $I_a = I_{qa}$ & $I_{da} = 0$:** in the case of the air-cored superconducting rotor constructed in this experiment, there is no saliency. In the case of a motor with no saliency, it is common to control armature current to be $I_{da} = 0$ and to generate only I_{qa} that contributes to torque generation for maximum torque output. This is the case in which the rotating magnetic field by the armature current coincides with the q-axis. As confirmed in the simulation of section 4.1.3, in this case, I_{da} is generated only momentarily in a transient situation, and $I_{da} = 0$ condition is satisfied soon by feedback control. Therefore, since I_{da} is rarely generated in this case, the response of the NI HTS field winding by $M_{fd}\frac{dI_{da}}{dt}$ term is relatively very small (figure 6.14 (a)).

- **Case 2) $I_a = I_{da}$ & $I_{qa} = 0$:** contrary to Case 1, it can be assumed that $I_{qa} = 0$ and only I_{da} exists. This is the case in which the direction of the magnetic field by the armature current coincides with the d-axis. In this case, since the armature current contributing to the torque generation is zero and only the armature current contributing to the flux generation in the direction of the rotor flux exists, no torque is generated. The NI HTS field winding responds to the magnetic field generated by the armature current ($M_{fd}\frac{dI_{da}}{dt}$) and a leak current generated, just like the conventional NI HTS magnet reacts to an external field. Of course, in this case, since torque generation is zero, it is a hypothetical case that rarely occurs in an actual motor control situation (figure 6.14 (b)).

- **Case 3) $I_a = \sqrt{I_{da}^2 + I_{qa}^2}$ & positive I_{da}:** a situation in which both I_{da} and I_{qa} exist can be considered. This is the case where the rotating magnetic field generated by I_a exists between the q-axis and d-axis of the rotor. In this case, a change in I_{da} occurs in a transient situation during the motor operation process, resulting in a leak current. In this case, since the direction of the magnetic field generated by I_{da} coincides with the direction of the magnetic field generated by the rotor, I_θ momentarily decreases as I_{da} increases, and I_θ instantaneously

increases as I_{da} decreases (figure 6.14 (c)).

- **Case 4) $I_a = \sqrt{I_{da}^2 + I_{qa}^2}$ & negative I_{da}:** as in Case 3, both I_{da} and I_{qa} exist, that is, the direction of the rotating magnetic field exists between the q-axis and the d-axis. In this case, since the direction of the magnetic field generated by I_{da} is opposite to the direction of the magnetic field generated by the rotor, when I_{da} increases, I_θ instantaneously increases, and when I_{da} decreases, I_θ also tends to instantaneously decrease. Voltage tendency that appeared in figure 6.13 is matched with this case (figure 6.14 (d)).

As can be seen from the response of the NI HTS field winding in figure 6.13, it can be seen that the experiment performed in this study corresponds to the situation of *case 4*, as the voltage of the NI HTS field winding is induced "opposite" to the line current value.

Comparison between Experiment Results and Simulation

Simulations were performed to see if the proposed simulation model can simulate the behavior of the motor observed in the actual transient experiment and the characteristics of the NI HTS field winding, and the results were compared with the experimental results. Considering the *case 4* situation above, it was assumed that the angle between the q-axis and rotating magnetic field was 36.9 degrees as an electric angle, and simulation was performed.

Basically, for the motor parameters used in the simulation, the same parameters as those presented in table 4.4 of section 4.1.3 were used except for the characteristic resistances of each coil. Speed and external load commands were given as shown in figure 6.12 in the simulation, and the feedback gain of speed control was set to be the same as the gain set in the actual inverter. In the analysis, voltage ripple according to L_f change according to rotation is not considered here, the comparison was made focusing on leak current behavior in transient operation. Details of the Simulink model

used for analysis are attached in appendix A.4.

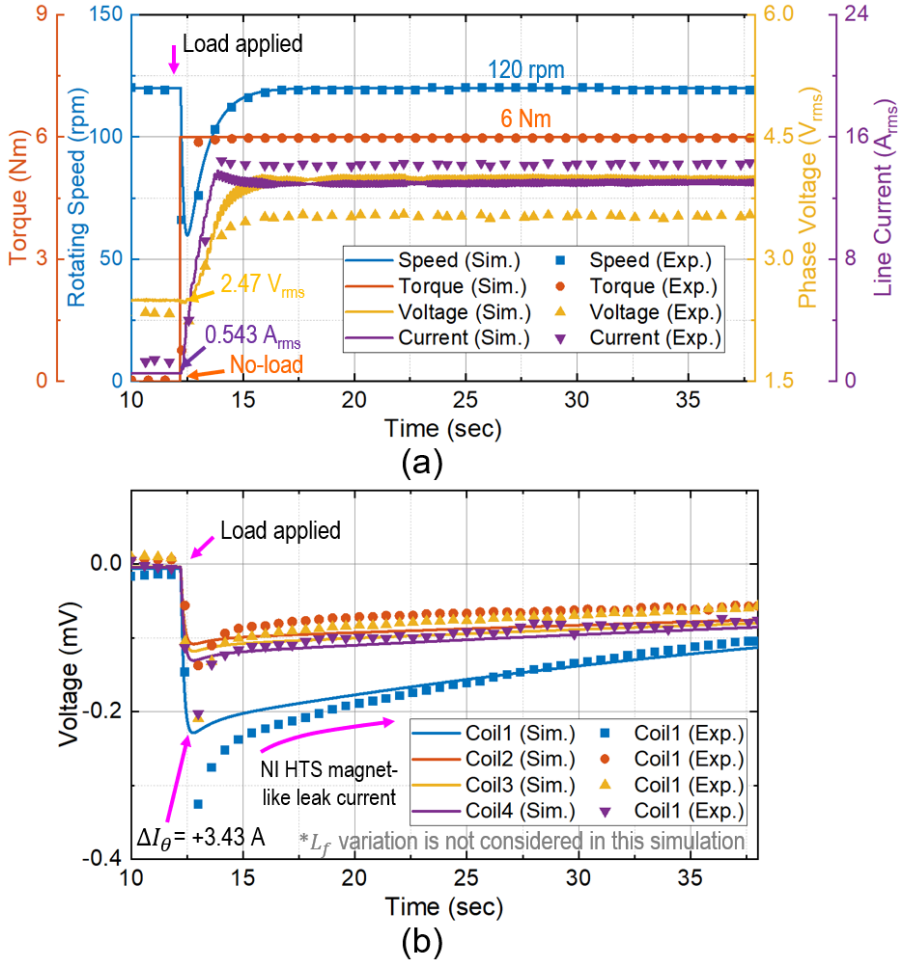

Figure 6.15: Sudden load simulation result. (a) Rotating speed, torque, phase voltage, and line current, (b) Voltage response of NI HTS field winding.

Figure 6.15 shows (a) speed, external load, phase voltage, and line current in sudden load simulation, while (b) voltage response of each NI HTS racetrack coil. In the case of speed, external load, voltage, and current, the simulation result shows good agreement with the experiment overall, and an error of up to 11.6% occurred in the voltage after the load was applied. In the simulation shown in (b), the ripple of the NI

HTS field winding was not considered, and the experiment results in (b) are moving averaged results to erase the effect of the ripples. The magnitude of the peak leak current showed a difference between simulation and experiment, but it was possible to simulate the saturation pattern after the leak current occurred.

Comparison between NI and INS Considering Experiment Conditions

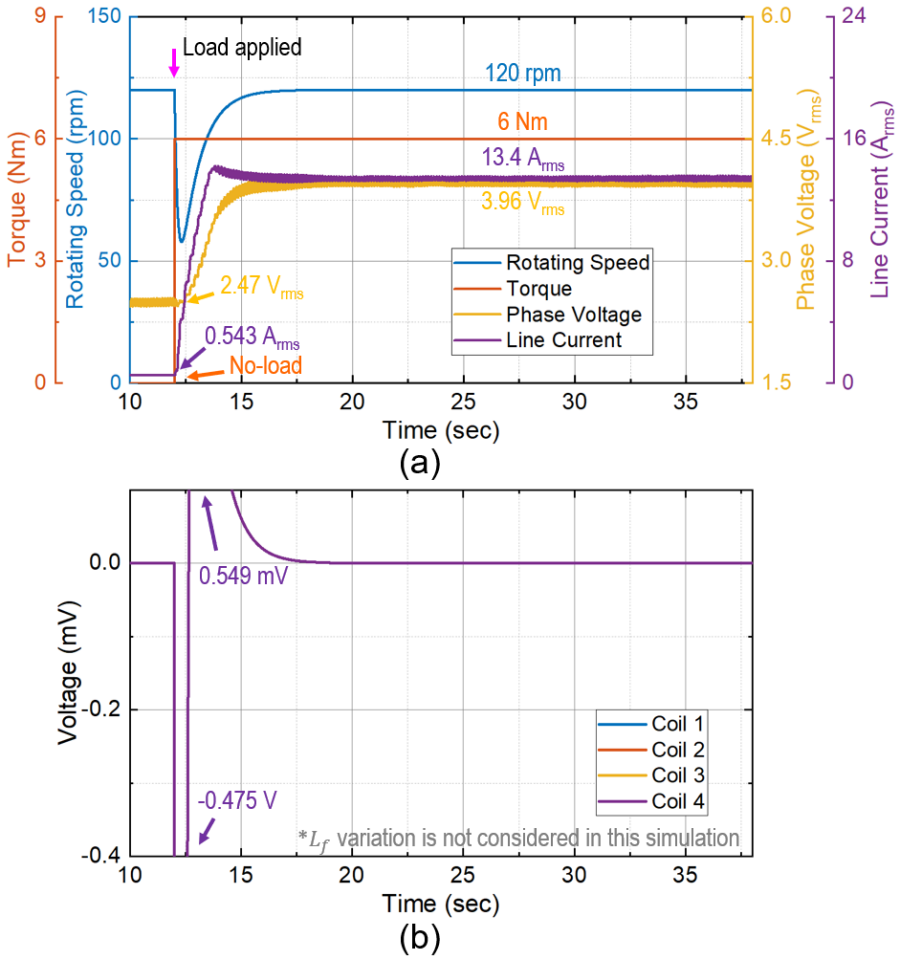

Figure 6.16: Sudden load simulation result of insulated counterpart. (a) Rotating speed, torque, phase voltage, and line current, (b) Voltage of insulated HTS field winding.

Finally, to compare the characteristics between NI and INS, a simulation with insulated field winding was performed for a sudden load test as shown in figure 6.16. In conclusion, there was little difference between NI and INS, except that the magnitude of the current flowing through the stator winding was slightly changed to produce the same required torque because the leak current occurred in the NI (figure 6.16 (a)). This shows that even if a leak current occurs, compensation by the stator winding current is achieved by current feedback control if the magnitude is not large. This tendency is also identified in the transient simulation in section 4.1.3. In the case of speed or torque response, it was confirmed that it was much more affected by the size of the gain in the control simulation rather than that the field winding is NI or INS. In the case of the voltage of the coil, as confirmed in the previous comparisons with the insulated counterpart, it was confirmed that a large voltage appeared and disappeared quickly compared to the NI.

6.5 Experiment Summary and Lessons Learned

6.5.1 Summary on Key Findings

Key Observation: Response of NI HTS Field Winding in Motor Operation

Through the experiments conducted in this study, it was confirmed that the NI HTS field winding shows two types of voltage responses during synchronous motor operation. These are due to the influence of inductance variation and current of armature coil, which was not considered in the existing NI HTS magnet. The leak current according to the change of I_{da} was confirmed in the stationary test, and the voltage ripple due to the inductance variation was confirmed in the steady-state test. In the transient operation, the two combined responses were confirmed. Figure 6.17 summarizes these two voltage responses and their characteristics.

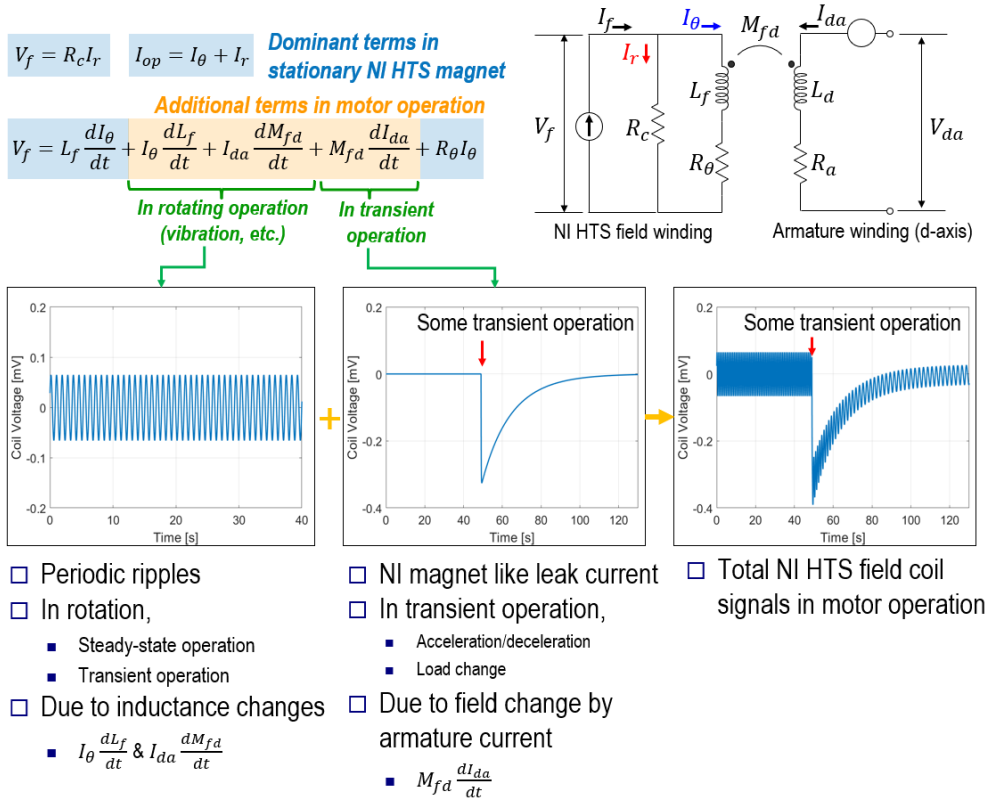

Figure 6.17: Summary on key observation of NI HTS field winding response.

6.5.2 Lessons Learned, Potential Challenges, and Required Improvements

Lesson Learned 1: Importance of Precise Construction and Inverter Tuning

In the experiment, it was confirmed that the effect caused by the manufacturing error (e.g., axis eccentricity) appears on the response of the NI HTS field winding as it is. Although this effect did not significantly affect the actual motor performance in this experiment, it could be a very important factor when manufacturing high-performance motors in the future, because mechanical errors can affect electromagnetic performance including NI HTS field winding.

So far, there is no previous study on motor control for NI HTS motors. In this study, a commercially available multi-purpose inverter was purchased and experiments were

conducted after performing simple tuning. In the analysis after tests, it was confirmed that this non-optimal tuning could affect the response of the NI HTS field winding. In future research, the response of the NI HTS field winding from the influence of this inverter should be considered from the design stage.

Lesson Learned 2: Difficulty of Signal Measurement of NI HTS Field Winding

The temperature and the voltage of the superconductor coil are commonly measured to monitor the current state of the superconductor coil. In the case of rotating NI HTS field winding, it is a low voltage signal of μV level and has the same frequency as the inductance variation. Therefore, as the operating speed increased, it was difficult to accurately measure the signal with the conventional superconductor magnet measuring instrument (e.g. NI DAQ). It is thought that any solutions for this measurement issue need to be considered in the case of high-speed driving tests in the future.

Lesson Learned 3: Effect of Cryogenic Temperature to Commercial Product

In this study, commercial products used in conventional non-superconducting motors were used to manufacture the superconducting motor test systems. When cooling the superconducting rotor using LN_2, the surrounding components are also cooled by evaporated N_2 gas, so temperatures lower than room temperature affected the operation of the commercial components. Most of the products operated without any major problems, but in the case of the bottom bearing and encoder, they were somewhat affected. In the case of the bearing, mechanical wear appeared quickly and friction was more severe than in the first operation, so it was replaced once. In the case of the encoder, there was a case of signal failure. Afterward, an additional heater was added to the corresponding parts and tested.

Potential Problem 1: NI HTS Coil Fabrication with Proper Contact Resistivity

As can be seen from the experimental results, the contact resistivity of the NI HTS coil affects all the so-called NI behaviors, such as the time required for charging and discharging the coil, and the size of the leak current during transient behavior. Therefore, determining appropriate contact resistivity in the design process and manufacturing the NI HTS coil as the design is considered to be one of the important challenges in the development of the NI HTS motor. Various factors such as winding tension and surface condition exist as factors that affect contact resistivity, and various studies are being conducted to control them. Winding techniques such as partial-insulation and metal-insulation [80, 108, 109], which belong to the so-called NI-class winding, and surface treatment and solder impregnation techniques have been also proposed [110–112]. It is known that the order of contact resistivity can be adjusted to some extent through these, however, no method has yet been proposed to fabricate the coil having a specific contact resistivity value. Therefore, it is thought that the study of coil fabrication techniques to control contact resistivity would be an important research topic in the future.

Potential Problem 2: Contact Resistivity Difference in Multi-pole Rotor

Since fine-tuning the contact resistivity of the NI HTS coil is quite difficult, there are cases where the contact resistivity is different even if the coil of the same specification is wound in the same way [79, 80]. This is a problem also seen in the wound racetrack coils in this study. In the case of previous NI HTS magnets, which are mainly operated in steady-state operation, this is not a critical problem except for the charging and discharging process. However, for motor applications where transient operation occurs frequently and balance between poles is important, this can be an important problem. This contact resistivity difference creates temporary unbalance between poles in a transient situation, creating a force acting in the radial direction, which may cause vibration. Accordingly, as in Problem 1 mentioned above, it is necessary to study a

coil fabrication technique with proper contact resistivity.

Potential Problem 3: Change of Contact Resistivity in Repeated Operation

The contact resistivity (R_{ct}) of NI HTS coils changed due to repeated cooling and charging-discharging over a long period of time. Table 6.2 summarizes the time constant (τ) and estimated contact resistivity through the coil voltage in the charging-discharging process on each test date. This change in R_{ct} directly affected the response of NI HTS field winding (figure 6.8 (d)). Changes in R_{ct} due to repeated experiments have been confirmed in previous papers [103, 113]. In the case of a motor with many transient operations, how to control this change in contact resistivity is expected to be an important challenge.

Required Improvement 1: Partial Element Equivalent Circuit for NI HTS Field Winding

In the case of the equivalent circuit model with NI HTS field winding proposed in this study, it is a model based on the lumped parameter equivalent circuit of the NI HTS coil. Since the proposed model assumes that the leakage current flows in the "radial" direction of the coil (figure 3.4), although basic analysis at the coil-level is possible, there is a limitation in that detailed current flow occurring in the coil cannot be analyzed. In the study of NI HTS solenoid magnets, improved analysis models such as the partial element equivalent circuit (PEEC) model and the turn-distributed model, had been already proposed and used for in-depth analysis of the NI properties in the coils [77, 78]. Therefore, in the case of NI HTS field winding, in order to understand the exact mechanism and increase the accuracy of the analysis, the development of these partial element analysis models is also needed in that more diverse factors must be considered in the NI HTS field winding compared to previous NI HTS magnets.

Table 6.2: Contact Resistivity Change Records of Each Coil

Test Date	Coil 1		Coil 2		Coil 3		Coil 4	
	τ	R_{ct}	τ	R_{ct}	τ	R_{ct}	τ	R_{ct}
01/14/2022	79.2	11.0	124	7.00	106	8.20	109	8.00
02/06/2022	67.0	13.0	116	7.50	103	8.50	96.8	9.00
02/10/2022	54.5	16.0	109	8.00	96.8	9.00	87.1	10.0
02/16/2022	51.3	17.0	96.8	9.00	85.4	10.2	77.8	11.2
02/18/2022	48.4	18.0	94.7	9.20	83.8	10.4	75.8	11.5
02/22/2022	47.1	18.5	92.7	9.40	82.2	10.6	74.5	11.7
03/22/2022	44.7	19.5	88.9	9.80	82.2	10.6	69.7	12.5
03/24/2022	43.6	20.0	87.1	10.0	79.2	11.0	69.7	12.6
03/28/2022	41.5	21.0	85.4	10.2	77.8	11.2	68.6	12.7
04/06/2022	41.5	21.0	85.4	10.2	77.8	11.2	67.6	12.9
04/11/2022	37.1	23.5	87.1	10.0	77.8	11.2	72.0	12.1
04/16/2022	37.1	23.5	79.2	11.0	72.6	12.0	65.5	13.3
04/21/2022	37.1	23.5	83.0	10.5	67.0	13.0	67.0	13.0

*The unit of τ is [sec], and the unit of R_{ct} is [$\mu\Omega$·cm^2].

Required Improvement 2: Other Considerations on Synchronous Machine with NI HTS Field Winding - Parameter Determination, Starting Method

As characteristic parameters of the synchronous machine, in addition to the synchronous reactance, there are various parameters such as transient reactance, sub-transient reactance, transient time constant, sub-transient time constant, and so on. These parameters can be determined through standard tests [114] or can be estimated through equations based on the equivalent circuit [115]. When NI HTS field winding is applied, there is a change in the equivalent circuit of the machine with insulated field winding, so the transient characteristic parameters may change, and the derivation formula may

also be different. Therefore, in order to use a synchronous machine with NI HTS field winding as a general synchronous machine, it is necessary to derive equations for determining these characteristic parameters. Also, in addition to the basic test to review the applicability of the NI HTS field winding performed in this study, experimental studies to determine other parameters of synchronous machines will be required.

Another issue with NI HTS field winding is how to take advantage of its NI behavior. As one of them, there is a consideration about whether the characteristics of the NI HTS coil can be utilized in the start-up of a synchronous machine like the damper coil in the conventional synchronous machine. In addition, it will be necessary to consider whether there is an optimal control method considering NI characteristics.

Chapter 7

CONCLUSION

This study presents an experimental and analytical study on the applicability of no-insulation (NI) high-temperature superconductor (HTS) field winding to a superconducting synchronous motor. NI HTS field winding has been considered to be a potential solution to improve the operation reliability and protection problem of HTS coils, which is one of the technical bottlenecks of HTS motors. However, actual demonstration and detailed analysis of the characteristic of synchronous motors with NI HTS coils have not been reported, also, how the nonlinear response of the NI HTS coil, so-called NI characteristics, affect the operating characteristics of the motor have not been discussed in detail so far. Therefore, in this study, the first analysis model of NI HTS motor considering NI behavior was proposed, and an experimental investigation on the applicability of NI HTS field winding to the superconducting motor was performed.

For the construction of a test machine with NI HTS field winding and an experimental system, electromagnetic, mechanical, and thermal characteristic analyses were performed first. In this study, the construction and test processes were simplified by using a stator of a commercial motor and a cooling system using liquid nitrogen (LN_2), and these aspects were taken into account in the design process. When designing the superconducting test machine, based on the previous analysis methods of the NI HTS coil, the first new analysis model for the NI HTS motor was suggested and used to

obtain machine performance. Based on the design results, four NI HTS racetrack coils were wound to fabricate an air-cored superconducting rotor, and combined with the prepared non-superconducting stator and LN_2 chamber to complete the test machine for the experiment. The completed test machine was coupled with the customized dynamo test system.

Operation characteristics of the test motor with NI HTS field winding were investigated in stationary, steady-state, and transient conditions, respectively. In stationary operation, the interaction between the stator and NI HTS field winding and its response were checked in the situation when the rotor was locked. As expected from the proposed equivalent circuit of the NI HTS motor, it was confirmed that a leak current occurred in the NI HTS field winding when the d-axis current was changed. On the other hand, the q-axis current did not affect the NI HTS field winding, and a proportional torque response was obtained. That is, the response characteristic to the q-axis current is the same as that of the insulated counterpart, but in the case of the response characteristic to the d-axis current, the leak current was identified in NI HTS field winding.

During steady-state operation, except for additional armature current injection due to mechanical friction and inverter tuning problems, it was possible to derive the same characteristics as designed in terms of electromotive force and torque. However, periodic voltage ripples of several tens of μV were observed in the NI HTS field winding, which could not be identified in the simulation under ideal conditions. It was analyzed that these ripples were caused by inductance variations due to manufacturing errors. The effect of these ripples on the steady-state performance of the motor was analyzed to be insignificant in this test machine, however, since motor characteristics may be affected depending on the design, additional review is necessary for various designs, especially for iron-cored motors. Compared to the insulated counterpart, these voltage ripples showed different tendencies, which can be analyzed through the proposed NI HTS motor analysis methods.

During operation in the transient situation, the leak current identified in stationary and the voltage ripples observed in steady-state operations were combined. In a transient operation like external load change, the leak current was instantaneously generated in the NI HTS field winding due to the influence of the magnetic field generated in the stator coil. In addition to the q-axis current contributing to torque generation, the d-axis current contributing to magnetic field generation was generated in transient situations, so a turn-to-turn leak current was instantaneously generated in the NI HTS field winding. Therefore, if the d-axis current was used during motor control, it is expected that the effect of the leak current during transient operation is clearly present. Compared to insulated counterparts in simulation, however, most of these leak current effects are compensated in the feedback control process of the armature current in terms of torque and speed.

In this study, with the primary goal of investigating the applicability of an NI HTS field winding to a synchronous motor, the cooling system was simplified using LN_2, and the commercially available products were used for stator and auxiliary components. Therefore, there was a limitation in which the operable point was limited by the performance of the cooling system and commercial products. Meanwhile, through this study, additional research and potential improvements could be derived for a superconducting motor with NI HTS field winding. In terms of construction, further research is needed in the future to control the contact resistance of NI HTS field coils to reduce potential unbalance. In terms of design and analysis, an improved analysis model (e.g. PEEC, turn-distributed model) to accurately analyze NI behavior is required. Also, testing and verification for deriving synchronous machine parameters in consideration of NI behavior are required.

Chapter A

APPENDICES

A.1 Bending Strain of REBCO Coated Conductor

This appendix section is about the bending strain of REBCO coated conductors. When REBCO coated conductor is bent for winding, due to the laminated structure, the strain is applied to the REBCO superconductor layer according to bending radius (r_b).

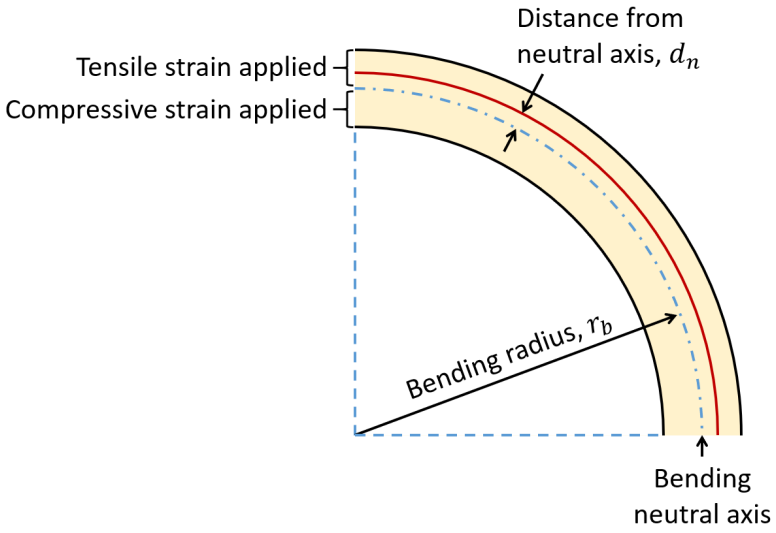

Figure A.1: A two dimensional schematic diagram for bending strain in a conductor.

As shown in figure A.1, the bending strain is zero in the bending neutral axis, but the compressive strain (ε_c) is applied inside the bending neutral axis and the tensile strain (ε_t) is applied outside. In the REBCO coated conductor, the REBCO superconductor layer is deposited on the substrate, so it usually deviates from the bending neutral axis. Bending strain can be obtained by the following analytic formula [116].

$$\varepsilon_c = \frac{\Delta L}{L} = \frac{\pi(2r_b - d_n) - 2\pi r_b}{\pi 2 r_b} = -\frac{d_n}{2r_b}, \tag{A.1}$$

$$\varepsilon_t = \frac{\Delta L}{L} = \frac{\pi(2r_b + d_n) - 2\pi r_b}{\pi 2 r_b} = \frac{d_n}{2r_b}, \tag{A.2}$$

where r_b is the bending radius and d_n is the distance of the REBCO layer from the neutral axis as shown in figure A.1. From the above equation (A.1) and (A.2), it can be seen that as the radius of the winding becomes smaller, the bending strain becomes larger. In the case of the SuNAM's REBCO coated conductor used in this study, the REBCO layer is deposited on the substrate with a thickness of 110 μm, and there are 15 μm of copper stabilizer layers on both sides of the conductor. Thus, d_n is calculated to be 55 μm. As a result, when r_b becomes smaller than 13.8 mm, bending strain can increase to 0.4%, which is the starting point of I_c degradation. In the case of the racetrack coil used in this study, the minimum r_b is 28 mm at the circular section, and the maximum bending strain was calculated to be 0.2%.

A.2 Derivation of Effective Mechanical Properties

Considering the laminated architecture of REBCO coated conductors with different materials, the conductor can be approximated to an equivalent material with effective mechanical properties in the analysis. This appendix section deals with the calculation of the effective mechanical properties including Young's modulus, Poisson's ratio and the Shear modulus of REBCO coated conductors.

Calculation of Effective Young's Modulus

These effective mechanical properties can be calculated from Hooke's law and their definitions [117]. Figure A.2 shows schematic models to calculate the effective Young's modulus of a laminated structure such as REBCO coated conductor. For the notation, r, h, and z of each axis of the figure, the notation used in the axis-symmetry condition of the conventional solenoid magnet, are used for the convenience of understanding. The r-axis corresponds to the c-axis of the REBCO coated conductor, and the plane formed by the h-axis and z-axis corresponds to the ab-plane. In the case of the r-axis direction shown in figure A.2 (a), it can be understood as a series connection of materials with lengths l_1, l_2, ..., l_m. On the other hand, in the case of the h-axis and z-axis shown in (b), it can be understood as a parallel connection of materials with areas of A_1, A_2, ..., A_m.

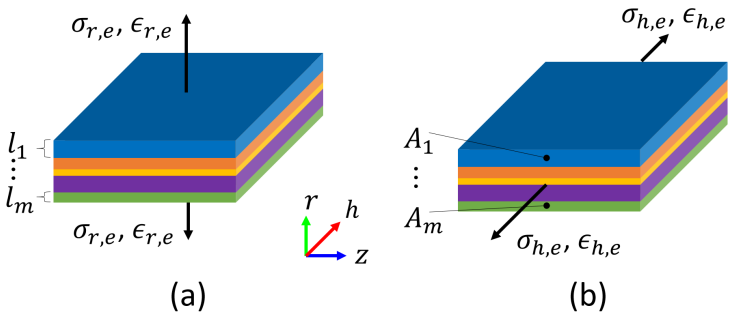

Figure A.2: Laminated conductor model for effective mechanical property calculation in the (a) r-axis direction and (b) h-axis direction.

On the r-axis (figure A.2 (a)), effective stress ($\sigma_{r,e}$), effective strain ($\varepsilon_{r,e}$), and effective Young's modulus ($E_{r,e}$) satisfy $\sigma_{r,e} = E_{r,e}\varepsilon_{r,e}$ by Hooke's law. At this time, since the total displacement of the r-axis must be equal to the sum of the displacements

of each material, it is given as equations (A.3) and (A.4).

$$\varepsilon_{r,e} \sum_{i}^{m} l_i = \sum_{i}^{m} \varepsilon_i l_i, \tag{A.3}$$

$$\frac{\sigma_{r,e}}{E_{r,e}} \sum_{i}^{m} l_i = \sum_{i}^{m} \frac{\sigma_i}{E_i} l_i. \tag{A.4}$$

Assuming that the given structure is a continuum, the forces applied to each material in the r-axis direction are the same. With the same cross-sectional area, the stress of each material equals the effective stress ($\sigma_{r,e} = \sigma_i$). Therefore, by erasing the stress terms, the effective Young's modulus in the r-axis direction is obtained as equation (A.5).

$$E_{r,e} = \frac{\sum_i^m l_i}{\sum_i^m (l_i / E_i)}. \tag{A.5}$$

In the case of the h-axis, in the situation of figure A.2 (b), the force applied to the cross-sectional area of each material equals the force applied to the total cross-sectional area, so it is given as equation (A.6).

$$\sigma_{h,e} \sum_{i}^{m} A_i = \sum_{i}^{m} \sigma_i A_i, \tag{A.6}$$

$$E_{h,e} \varepsilon_{h,e} \sum_{i}^{m} A_i = \sum_{i}^{m} E_i \varepsilon_i A_i. \tag{A.7}$$

Due to Hooke's law, equation (A.6) is converted to equation (A.7). Since the strain of each material is the same as the effective strain ($\epsilon_{h,e} = \epsilon_i$), by removing the strain term, it is finally given as equation (A.8).

$$E_{h,e} = \frac{\sum_i^m E_i A_i}{\sum_i^m A_i}. \tag{A.8}$$

Since Young's modulus of the z-axis is in the same situation as the h-axis, it can be derived using the same principle.

Calculation of Effective Poisson's Ratio

Figure A.3 shows schematic models to calculate the effective Poisson's ratio.

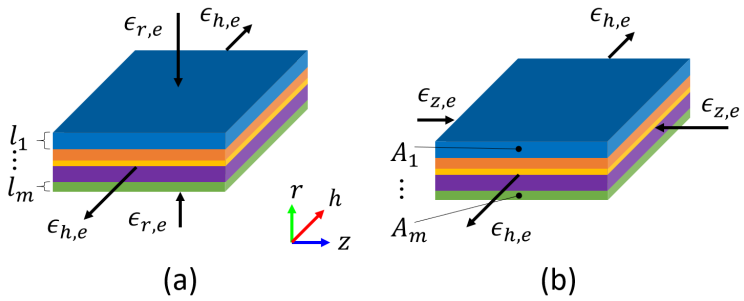

Figure A.3: Laminated conductor model for effective Poisson's ratio calculation in the (a) rh-plane and (b) hz-plane.

When stretching in the h-axis direction as shown in figure A.3(a), $\varepsilon_{h,e}$ and $\varepsilon_{r,e}$ satisfy the relationship of $\varepsilon_{r,e} = -\nu_{hr,e}\varepsilon_{h,e}$. At this time, since the total contraction of the r-axis must be equal to the sum of the contractions of each material, it is given as equations (A.9)–(A.11).

$$\varepsilon_{r,e}\sum_{i}^{m} l_i = \sum_{i}^{m} \varepsilon_i l_i, \tag{A.9}$$

$$\varepsilon_{r,e}\sum_{i}^{m} l_i = -\sum_{i}^{m} \nu\varepsilon_{h,e} l_i, \tag{A.10}$$

$$-\nu_{hr,e}\varepsilon_{h,e}\sum_{i}^{m} l_i = -\sum_{i}^{m} \nu\varepsilon_{h,e} l_i. \tag{A.11}$$

By erasing the strain terms, the effective Poisson's ratio is obtained as follows.

$$\nu_{hr,e} = \frac{\sum_i^m \nu_i l_i}{\sum_i^m l_i}. \tag{A.12}$$

Considering the relation of $\nu_{ij}/E_i = \nu_{ji}/E_j$, $\nu_{rh,e}$ can be obtained as follow.

$$\nu_{rh,e} = \frac{E_{r,e}}{E_{h,e}}\frac{\sum_i^m \nu_i l_i}{\sum_i^m l_i}. \tag{A.13}$$

For the calculation of $\nu_{rz,e}$ and $\nu_{zr,e}$, the same principle can be applied.

$\nu_{hz,e}$ and $\nu_{hz,e}$ can be calculated through the case shown in figure A.3 (b). Assuming that it is stretched in the h-axis direction, $\varepsilon_{h,e}$ and $\varepsilon_{z,e}$ hold the following

relationship.

$$\varepsilon_{z,e} = -\nu_{hz,e}\varepsilon_{h,e}. \tag{A.14}$$

Here, to guarantee the same $\varepsilon_{z,e}$ in the z-axis direction, internal stress is generated in each material, and the following is satisfied by internal force equilibrium.

$$\frac{\sum_i^m A_i \sigma_i^{int}}{\sum_i^m A_i} = 0. \tag{A.15}$$

Accordingly, the following conditions are satisfied in each component according to the principle of superposition.

$$\varepsilon_{z,e} = -\nu_i \varepsilon_{h,e} + \frac{\sigma_i^{int}}{E_i}. \tag{A.16}$$

Combining the above formulas (A.14)–(A.16), the following relation is derived.

$$\nu_{hz,e} = \frac{\sum_i^m A_i \nu_i E_i}{\sum_i^m A_i E_i}. \tag{A.17}$$

Considering the relation of $\nu_{ij}/E_i = \nu_{ji}/E_j$, $E_i = E_j$ in this case, so $\nu_{hz,e} = \nu_{zh,e}$ is given.

Calculation of Effective Shear Modulus

Figure A.4 shows schematic models to calculate the effective Shear modulus.

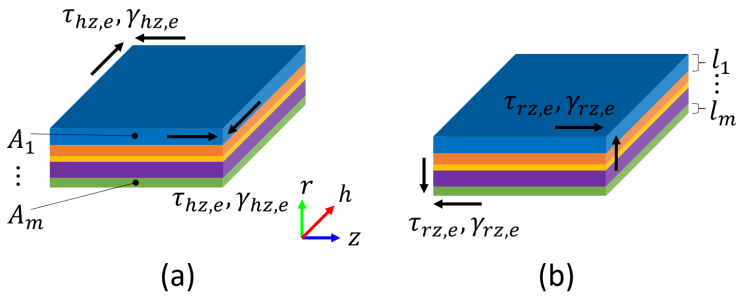

Figure A.4: Laminated conductor model for effective shear modulus calculation in the (a) hz-plane and (b) rz-plane.

As shown in figure A.4 (a), when shear deformation occurs in the hz-plane, $\tau_{hz,e} = G_{hz}\gamma_{hz,e}$ is satisfied. Since the shear strain given to each component is the same and the force equilibrium must be satisfied, the following equations are given.

$$\tau_{hz,i} = G_i\gamma_{hz,e}, \tag{A.18}$$

$$\tau_{hz,e}\sum_{i}^{m} A_i = \sum_{i}^{m} A_i\tau_{hz,i}. \tag{A.19}$$

If the given formulas are arranged for G_{hz}, the final equation is given as follows.

$$G_{hz,e} = \frac{\sum_i^m G_i A_i}{\sum_i^m A_i}. \tag{A.20}$$

In the case of figure A.4 (b) with shear deformation in the rz-plane, $\tau_{rz,e} = G_{rz}\gamma_{rz,e}$ by Hooke's law in shear is satisfied. Considering that the total shear deformation is the sum of the shear deformations of each component, the following is satisfied.

$$\gamma_{rz,e}\sum_{i}^{m} l_i = \sum_{i}^{m} \gamma_{rz,i} l_i. \tag{A.21}$$

Assuming that each component receives the same shear stress, $\gamma_{rz,i} = \tau_{rz,e}/G_i$ is satisfied. If the given formulas are arranged for G_{rz}, the final equation is given as follows.

$$G_{rz} = \frac{\sum_i^m l_i}{\sum_i^m (l_i/G_i)}. \tag{A.22}$$

Since shear deformation in the rh-plane is the same as in the case of shear deformation in the rz-plane, G_{rh} can be derived in the same way.

A.3 Stability and Protection Properties of NI HTS Coil

This appendix section describes the calculations of the stability and protection properties of the racetrack coil designed for the experiment, which were not described in the main text. The concept of stability and protection of the superconducting coil is briefly introduced and related calculations are performed.

Stability: Current, Temperature, and Energy Margin

In a superconductor coil, the stored energy in the coil can easily be converted into heat initiated by external disturbances, raising the coil temperature to above its critical value (T_c). Therefore, for stable operation of the superconductor coil, it is necessary to evaluate how much margin the superconductor coil secures and whether the margin is sufficient for the coil to maintain stable operation in the presence of external disturbance. As concepts used as a stability margin of a superconductor coil, there are energy margin (Δe), temperature margin (ΔT), and current margin (ΔI) [83]. Figure A.5 is a schematic describing these concepts of stability margin.

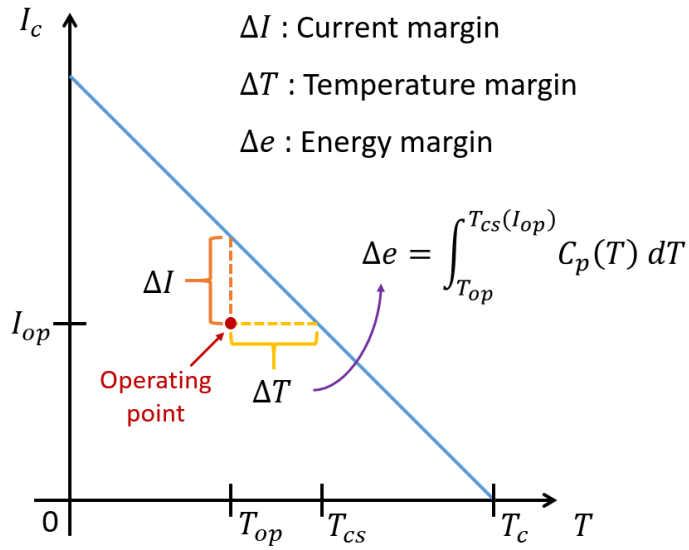

Figure A.5: Concept of stability margins: current margin (ΔI), temperature margin (ΔT), and energy margin (Δe).

In figure A.5, the blue line schematically represents the critical current (I_c) according to temperature (T), then the operating point of the superconductor coil must exist inside this blue line to maintain superconductivity. When the operating point (T_{op}, I_{op}) is given as the red point shown in the figure, the current difference between the oper-

ating point and the blue line in T_{op} is the current margin (ΔI), and the temperature difference between the operating point and the blue line in I_{op} is defined as the temperature margin (ΔT). Lastly, the energy margin (Δe) is given as the integral of the heat capacity ($C_p(T)$) of the superconductor coil as much as the temperature margin, and it means the energy density required to increase the temperature up to the critical point.

When calculating Δe, since the heat capacity of material changes depending on the temperature at cryogenic temperatures, this temperature-dependent heat capacity ($C_p(T)$) must be considered. Figure A.6 shows the heat capacity of materials typically used at cryogenic temperatures in the range of 4–300 K [118]. Because the heat capacity of the material is reduced significantly in cryogenic temperature. It can be expected that the value of Δe can be much reduced at lower T_{op}.

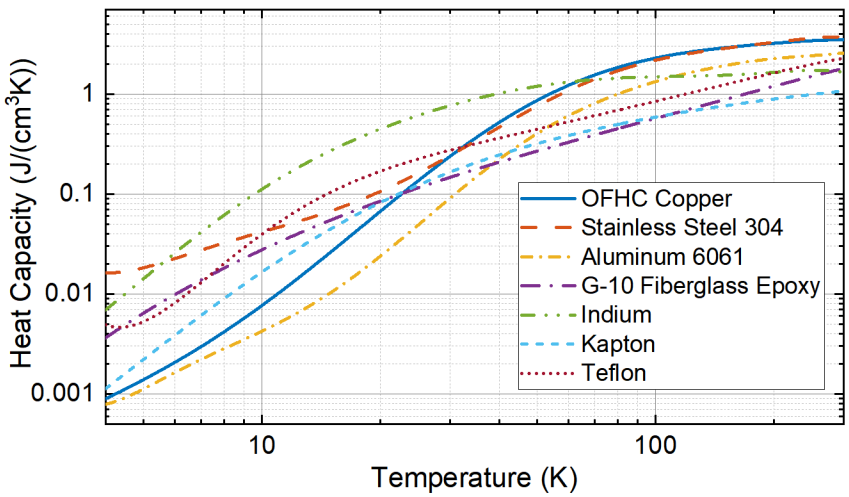

Figure A.6: Heat capacity of materials in cryogenic temperature.

Using the stability concept described above, the stability of the REBCO racetrack coil for each selected temperature was calculated, and the results are summarized in table A.1. Considering the ratio of copper and stainless steel in the REBCO coated conductor (3:11) in this study, the equivalent heat capacity of the REBCO coated con-

ductor was derived, and Δe is calculated. The operating point was determined to keep the same ratio of the current margin as 30%, that is, to satisfy $I_{op} = 0.7 I_c$. In the table, it can be seen that in the case of T_{op}= 20 K, although ΔI and ΔT are larger compared to other temperatures, Δe is calculated to be the lowest due to the relatively low heat capacity at low T.

Table A.1: Stability Margin of Designed Racetrack Coil at Each Temperature

T_{op} [K]	I_{op} [A]	ΔT [K]	ΔI [A]	Δe [J/cm^3]
20	344	21.3	147	5.74
40	224	15.3	96	10.8
60	132	9.35	57	11.8
77.4	66.2	4.08	28.4	7.00

Protection: Temperature Rise Estimation in Quench

When the heat dissipation in the superconductor coil exceeds the stability margin, quench happens. Right after the quench occurs, electrical resistance abruptly surges, and massive heat is generated within a very short time, which may cause permanent damage to the coil. Therefore, protecting the superconductor coil from permanent damage becomes an important issue. In order to determine the appropriate protection method for the coil, it is necessary to estimate the degree of temperature rise and the time taken for the temperature rise in a post-quench situation.

One conventional approach to estimating these values is to use Z-function [83]. Z-function is a concept proposed to estimate the time it takes for the temperature to rise in the superconductor wire in constant current operation after the quench. Assuming that quench and temperature rise occurs very rapidly, an adiabatic condition is assumed in the Z-function analysis, and it is also assumed that the current is diverted to the stabilizer layer rather than the superconductor layer due to the presence of resistance

in the superconductor.

$$Z(T_f, T_i) = \int_{T_i}^{T_f} \frac{C_{st}(T)}{\rho_{st}(T)}\, dT, \tag{A.23}$$

$$t_{ah} = \frac{A_{\bar{st}} + A_{st}}{A_{st}} \frac{Z(T_f, T_i)}{J_{st}^2}. \tag{A.24}$$

The Z-function is defined as in equation (A.23), and the time (t_{ah}) taken to rise from the initial temperature (T_i) to the final temperature (T_f) can be calculated using $Z(T_f, T_i)$ as shown in equation (A.24). Here, $C_{st}(T)$ and $\rho_{st}(T)$ are the heat capacity and electric resistivity of the stabilizer according to the temperature. A_{st} and $A_{\bar{st}}$ mean cross-sectional area of stabilizer and cross-sectional area of conductor except stabilizer. J_{st} is the current density in the stabilizer layer when all currents flow to the stabilizer layer. A detailed derivation of the Z-function can be found in [83].

Based on the specification of SuNAM's REBCO coated conductor used in this study, t_{ah} to reach $T_f = 300$ K is calculated to be 0.0227 seconds at $T_i = 20$ K and 0.345 seconds at $T_i = 77$ K. The temperature-dependent $\rho_{st}(T)$ used in the calculation is shown in figure A.7 [119], and residual-resistance ratio (RRR) was assumed to be 100. Calculation results imply that the given time for the protection of the coil protection is quite short, and in the case of HTS having a much slower normal zone propagation velocity than LTS [83], local hot-spot and permanent damage can easily occur in the quench.

However, in the case of the NI HTS coil, the current not only diverts to the stabilizer but also the current by-passes through the contact between turns. Therefore, the assumption of current in the Z-function analysis is too conservative to evaluate an NI HTS coil. In order to analyze the post-quench behavior of the NI HTS coil, a lot of analysis based on the equivalent circuit model is in progress [77, 120, 121]. In these studies, heat occurs not only at the local stabilizer layer but throughout the contact with the adjacent turns, so the heat concentration at a local point is prevented. Also, "fast" quench propagation occurs to magnetically coupled adjacent coils in an electromagnetic way, enabling the coil protection from local hot-spot [122]. Therefore, in

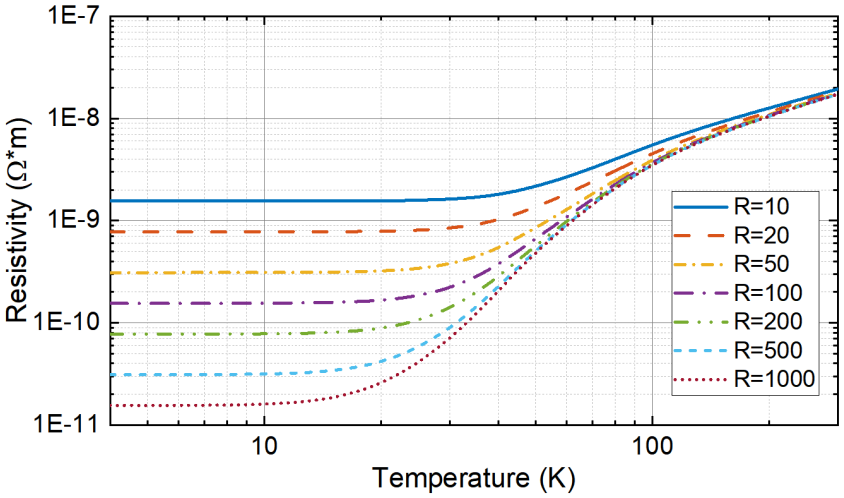

Figure A.7: Resistivity of copper in cryogenic temperature.

consideration of these characteristics, it is assumed that the temperature rise of the NI HTS coil occurs throughout the coil after the quench, and the following equation is used to evaluate the temperature rise of the NI HTS coil [123].

$$\frac{1}{2}LI_{op}^2 = \int_{T_i}^{T_f} V_m C_{cd}(T)\, dT. \tag{A.25}$$

Equation (A.25) assumes a situation in which all stored magnetic energy ($= LI_{op}^2/2$) is converted into heat under the adiabatic condition to increase the temperature of the entire coil. Here, V_m is the volume of the coil, and $C_{cd}(T)$ is the heat capacity of the magnet according to the temperature. Based on equation (A.25), the racetrack coil's temperature rise is calculated again, then T_f can be calculated to be 38.9 K in 20 K operation and 77.5 K in 77 K operation, which are safe temperatures far from permanent damage.

A.4 Detailed Simulink Modeling for Transient Simulation

In this appendix section, details of the MATLAB Simulink model used for the equivalent circuit simulation are attached.

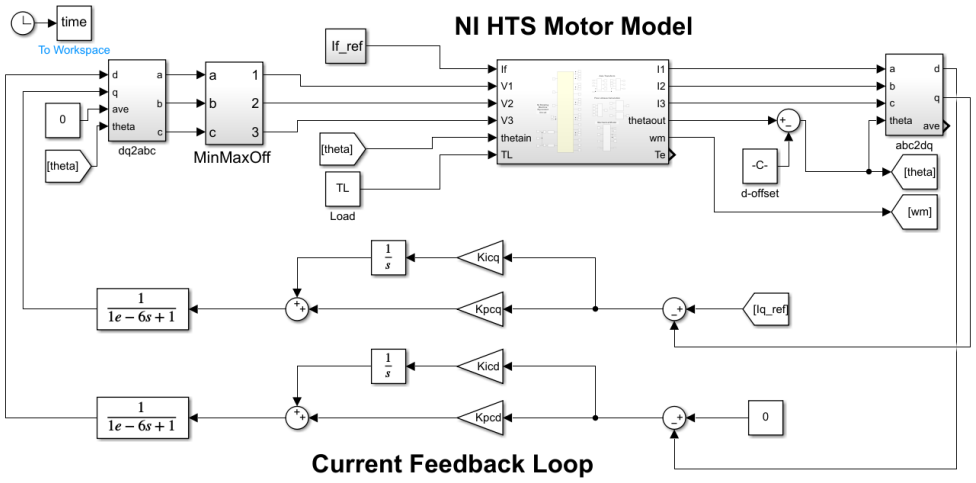

Figure A.8: Simulink simulation module - current feedback control loop.

Figure A.8 shows the current feedback control loop in the Simulink simulation module. Basically, it was controlled to satisfy $I_{da} = 0$ considering the air-cored structure of the test motor, but the control method was adjusted according to the experimental conditions. The current control was performed through PI control.

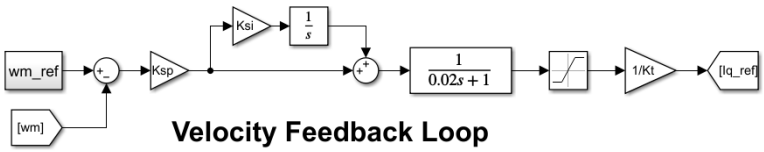

Figure A.9: Simulink simulation module - speed feedback control loop.

Figure A.9 shows the speed feedback control loop in the simulation. It was controlled to satisfy the target speed through PI control. Feedback gain was set by referring to the recommended setting range of the commercial inverter actually used in the experiment.

An overview of the NI HTS motor model used in the simulation is shown in figure

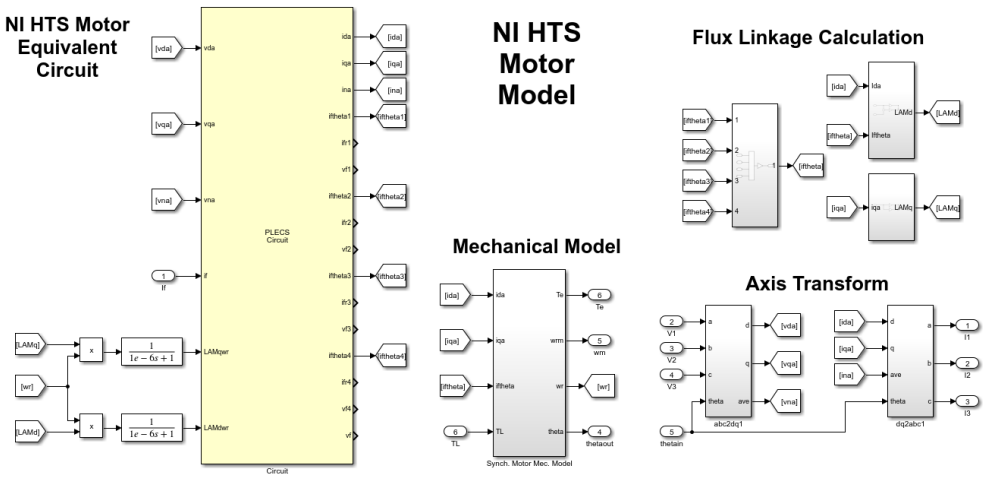

Figure A.10: Simulink simulation module - an overview of NI HTS motor model.

A.10. It consists of the proposed equivalent circuit model, mechanical model, axis transform module, and flux linkage calculation module.

Figure A.11 shows the implemented equivalent circuit model of the NI HTS motor in the Simulink simulation module. The three circuits in the figure represent equivalent circuits in the d-axis, q-axis, and n-axis, respectively, and four NI HTS field coils are mutually coupled on the d-axis. Based on the proposed analysis model, the characteristics of the NI HTS field winding were shown by connecting parallel resistors. For circuit simulation, the PLECS circuit simulation tool was used by coupling it to the Simulink module.

A mechanical model used for motor simulation is shown in figure A.12. The rotation speed and location of the rotating angle of the motor were calculated with the generated torque, external load, rotating inertia, and friction coefficient of the motor.

Figure A.13 shows how the flux linkage is calculated in the simulation. The flux linkage was calculated using the currents and inductance in the NI HTS motor.

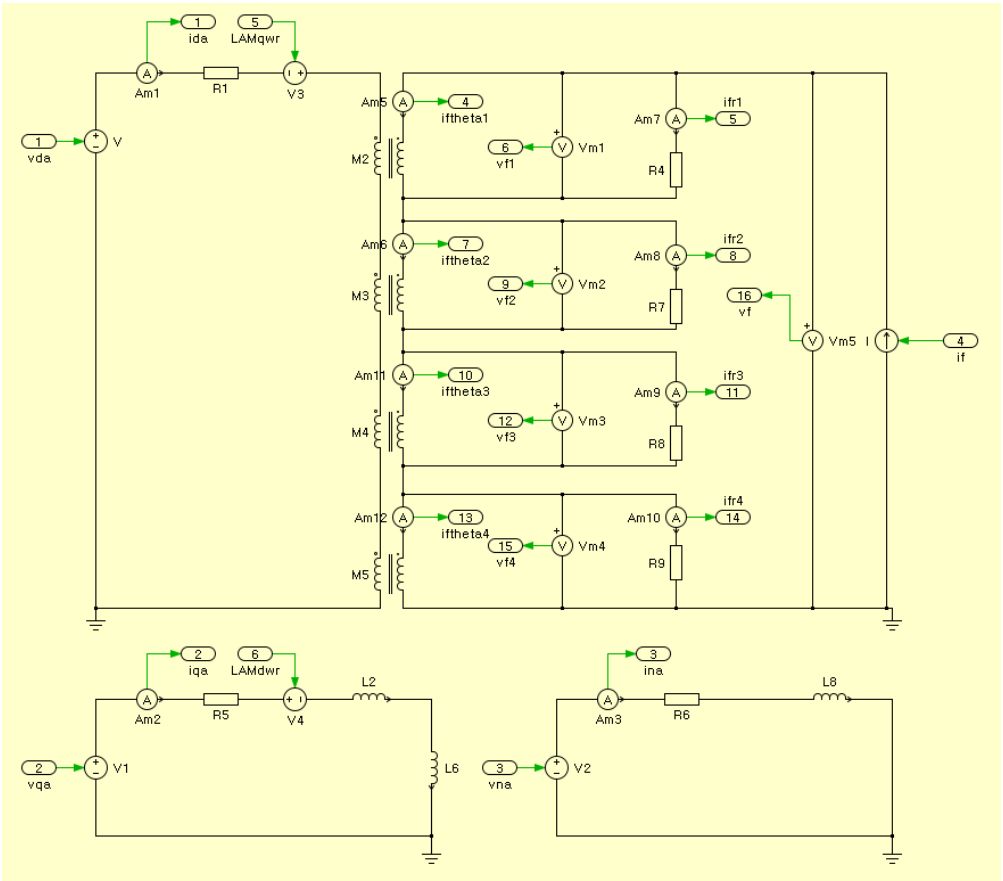

Figure A.11: Simulink simulation module - equivalent circuit model of NI HTS motor.

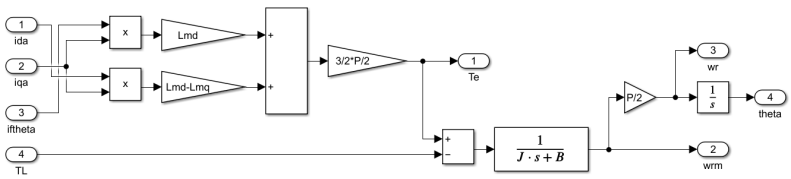

Figure A.12: Simulink simulation module - a mechanical model of NI HTS motor.

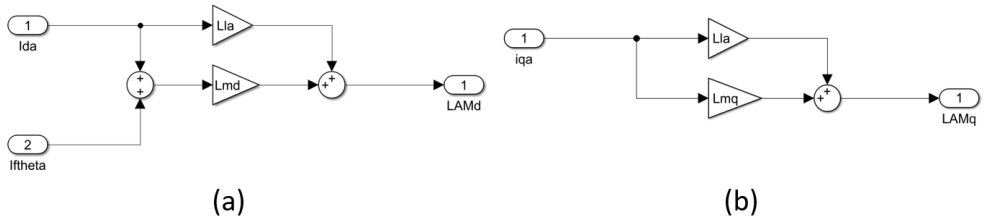

Figure A.13: Simulink simulation module - flux linkage calculation.

Bibliography

[1] International Energy Agency (IEA), "Net Zero by 2050, A Roadmap for the Global Energy Sector," 2021. [Online]. Available: https://www.iea.org/reports/net-zero-by-2050.

[2] U. Bong, C. Im, J. Yoon, S. An, S.-W. Jung, K. J. Han, and S. Hahn, "Investigation on Key Parameters of NI HTS Field Coils for High Power Density Synchronous Motors," *IEEE Trans. Appl. Supercond.*, vol. 31, no. 5, pp. 1–5, 2021.

[3] Wikipedia, "Superconducting electric machine," 2022. [Online]. Available: https://en.wikipedia.org/wiki/superconducting_electric_machine.

[4] K. S. Haran, S. Kalsi, T. Arndt, H. Karmaker, R. Badcock, B. Buckley, T. Haugan, M. Izumi, D. Loder, J. W. Bray, P. Masson, and E. W. Stautner, "High power density superconducting rotating machines—development status and technology roadmap," *Supercond. Sci. Technol.*, vol. 30, no. 12, p. 123002, 2017.

[5] D. Dezhin, I. Dezhina, and R. Ilyasov, "Small-scale prototype of a fully HTS-2G six-phase induction electrical machine," *J. Phys. Conf. Ser. (JPCS)*, vol. 1559, no. 1, p. 012146, 2020.

[6] B. Liu, R. Badcock, H. Shu, and J. Fang, "A superconducting induction motor with a high temperature superconducting armature: Electromagnetic theory, design and analysis," *Energies*, vol. 11, no. 4, p. 792, 2018.

[7] T. Balachandran, D. Lee, N. Salk, and K. Haran, "A fully superconducting air-core machine for aircraft propulsion," *IOP Conf. Ser. Mater. Sci. Eng.*, vol. 756, no. 1, p. 012030, 2020.

[8] J. R. Melcher and H. H. Woodson, *Electromechanical dynamics*. John Wiley & Sons, 1968.

[9] S. J. Chapman, *Electric machinery fundamentals*. McGraw-Hill, 2004.

[10] Y. Terao, A. Seta, H. Ohsaki, H. Oyori, and N. Morioka, "Lightweight design of fully superconducting motors for electrical aircraft propulsion systems," *IEEE Trans. Appl. Supercond.*, vol. 29, no. 5, pp. 1–5, 2019.

[11] C. D. Manolopoulos, M. F. Iacchetti, A. C. Smith, K. Berger, M. Husband, and P. Miller, "Stator design and performance of superconducting motors for aerospace electric propulsion systems," *IEEE Trans. Appl. Supercond.*, vol. 28, no. 4, pp. 1–5, 2018.

[12] B. Gamble, G. Snitchler, and T. MacDonald, "Full power test of a 36.5 MW HTS propulsion motor," *IEEE Trans. Appl. Supercond.*, vol. 21, no. 3, pp. 1083–1088, 2010.

[13] R. Radebaugh, "Cryocoolers for aircraft superconducting generators and motors," *AIP Conf. Proc.*, vol. 1434, no. 1, pp. 171–182, 2012.

[14] T. Coombs, "Superconducting flux pumps," *J. Appl. Phys.*, vol. 125, no. 23, p. 230902, 2019.

[15] J. H. Kim, Y. S. Chae, H. L. Quach, Y. S. Yoon, H. Jeon, S. Han, T. K. Ko, J. Lee, H.-W. Kim, Y.-S. Jo, H. J. Park, and H. M. Kim, "Fabrication and performance testing of a 1-kW-class high-temperature superconducting generator with a high-temperature superconducting contactless field exciter," *Supercond. Sci. Technol.*, vol. 33, no. 9, p. 095003, 2020.

[16] Y. Gao, W. Wang, X. Wang, H. Ye, Y. Zhang, Y. Zeng, Z. Huang, Q. Zhou, X. Liu, Y. Zhu, and Y. Lei, "Design, fabrication, and testing of a YBCO racetrack coil for an HTS synchronous motor with HTS flux pump," *IEEE Trans. Appl. Supercond.*, vol. 30, no. 4, pp. 1–5, 2020.

[17] H. Moon, Y.-C. Kim, H.-J. Park, I.-K. Yu, and M. Park, "An introduction to the design and fabrication progress of a megawatt class 2G HTS motor for the ship propulsion application," *Supercond. Sci. Technol.*, vol. 29, no. 3, p. 034009, 2016.

[18] U. Bong, S. An, J. Voccio, J. Kim, J. T. Lee, J. Lee, K. J. Han, H. Lee, and S. Hahn, "A Design Study on 40 MW Synchronous Motor With No-Insulation HTS Field Winding," *IEEE Trans. Appl. Supercond.*, vol. 29, no. 5, pp. 1–6, 2019.

[19] M. Bauer, "Development, test, installation, and commissioning of the 3 MW superconducting EcoSwing wind power generator," *International Conference on Magnet Technology 26*, Vancouver, Canada, Sep. 22–27, 2019.

[20] W. Nick, J. Grundmann, and J. Frauenhofer, "Test results from Siemens low-speed, high-torque HTS machine and description of further steps towards commercialisation of HTS machines," *Physica C*, vol. 482, pp. 105–110, 2012.

[21] T. Yanamoto, M. Izumi, M. Yokoyama, and K. Umemoto, "Electric propulsion motor development for commercial ships in Japan," *Proc. IEEE*, vol. 103, no. 12, pp. 2333–2343, 2015.

[22] T. Keim, T. Laskaris, J. Fealey, and P. Rios, "Design and manufacture of a 20 MVA superconducting generator," *IEEE Trans. Power Appar. Syst.*, vol. PAS-104, no. 6, pp. 1474–1483, 1985.

[23] R. Marshall, "3000 horsepower superconductive field acyclic motor," *IEEE Trans. Magn.*, vol. 19, no. 3, pp. 876–879, 1983.

[24] S. S. Kalsi, “Development status of superconducting rotating machines,” *2002 IEEE Power Engineering Society Winter Meeting*, NewYork, USA, Jan. 27–31, 2002.

[25] G. Snitchler, B. Gamble, and S. S. Kalsi, “The performance of a 5 MW high temperature superconductor ship propulsion motor,” *IEEE Trans. Appl. Supercond.*, vol. 15, no. 2, pp. 2206–2209, 2005.

[26] W. Nick, G. Nerowski, H.-W. Neumüller, M. Frank, P. Van Hasselt, J. Frauenhofer, and F. Steinmeyer, “380 kW synchronous machine with HTS rotor windings—-development at Siemens and first test results,” *Physica C*, vol. 372–376, pp. 1506–1512, 2002.

[27] Y. Kwon, M. Sohn, S. Baik, E. Lee, J. Kim, T. Moon, H. Park, Y. Kim, and K. Ryu, “Development of a 100 hp synchronous motor with HTS field coils,” *IEEE Trans. Appl. Supercond.*, vol. 15, no. 2, pp. 2194–2197, 2005.

[28] Y. Kwon, H. Kim, S. Baik, E. Lee, J. Lee, Y. Kim, S. Lee, J. Hong, Y. Jo, and K. Ryu, “Performance test of a 1 MW class HTS synchronous motor for industrial application,” *Physica C*, vol. 468, no. 15-20, pp. 2081–2086, 2008.

[29] R. H. Jansen, J. Scheidler, T. Tallerico, P. Kascak, A. Woodworth, A. D. Smith, R. Dyson, W. Sixel, J. Thompson, E. Stalcup, Y. D. Jesus-Arce, and D. Avanesian, “High efficiency megawatt motor risk reduction activities,” in *Proc. AIAA/IEEE Elect. Aircr. Technol. Symp. (EATS)*, 2020, pp. 1–12.

[30] R. Sugouchi, M. Komiya, S. Miura, M. Iwakuma, K. Yoshida, T. Sasayama, T. Yoshida, K. Yamamoto, Y. Sasamori, H. Honda, Y. Hase, M. Shuto, M. Konno, and T. Izumi, “Conceptual design and electromagnetic analysis of 2 MW fully superconducting synchronous motors with superconducting magnetic shields for turbo-electric propulsion system,” *IEEE Trans. Appl. Supercond.*, vol. 30, no. 4, pp. 1–5, 2020.

[31] Raytheon Technologies Research Center, "Superconducting Motor and Cryo-Cooled Inverter Engine: SOARING," 2021. [Online]. Available: https://www.arpa-e.energy.gov/technologies/projects/superconducting-motor-and-cryo-cooled-inverter-engine-soaring-pe000399.

[32] A. Perez, R. Van Der Woude, and R. Dekker, "Rotor cooling concept for the ASuMED superconductive motor," *IOP Conf. Series: Mater. Sci. Eng.*, vol. 502, no. 1, p. 012139, 2019.

[33] D. Dezhin, R. Ilyasov, S. Kozub, K. Kovalev, and L. Verzhbitsky, "Synchronous motor with HTS-2G wires," *J. Phys. Conf. Ser.*, vol. 507, no. 3, p. 032011, 2014.

[34] D. Dezhin, K. Kovalev, L. Verzhbitskiy, S. Kozub, and V. Firsov, "Design and testing of 200 kW synchronous motor with 2G HTS field coils," *IOP Conf. Ser. Earth Environ. Sci.*, vol. 87, no. 3, p. 032007, 2017.

[35] S. Hahn, D. K. Park, J. Bascuñán, and Y. Iwasa, "HTS pancake coils without turn-to-turn insulation," *IEEE Trans. Appl. Supercond.*, vol. 21, no. 3, pp. 1592–1595, 2011.

[36] S. Hahn, K. Radcliff, K. Kim, S. Kim, X. Hu, K. Kim, D. V. Abraimov, and J. Jaroszynski, "'Defect-irrelevant'behavior of a no-insulation pancake coil wound with REBCO tapes containing multiple defects," *Supercond. Sci. Technol.*, vol. 29, no. 10, p. 105017, 2016.

[37] Y. Choi, D. Yang, Y. Kim, S. Kim, J. Song, and H. Lee, "A study of the electromagnetic characteristics of no-insulation GdBCO racetrack coils under an external magnetic ripple field," *Supercond. Sci. Technol.*, vol. 29, no. 4, p. 045010, 2016.

[38] X. Wang, S. Hahn, Y. Kim, J. Bascuñán, J. Voccio, H. Lee, and Y. Iwasa, "Turn-to-turn contact characteristics for an equivalent circuit model of no-insulation ReBCO pancake coil," *Supercond. Sci. Technol.*, vol. 26, no. 3, p. 035012, 2013.

[39] J. Bascuñán, S. Hahn, Y. Kim, J. Song, and Y. Iwasa, "90-mm/18.8-T all-HTS insert magnet for 1.3 GHz LTS/HTS NMR application: Magnet design and double-pancake coil fabrication," *IEEE Trans. Appl. Supercond.*, vol. 24, no. 3, pp. 1–4, 2013.

[40] S. Hahn, K. Kim, K. Kim, X. Hu, T. Painter, I. Dixon, S. Kim, K. R. Bhattarai, S. Noguchi, J. Jaroszynski, and D. C. Larbalestier, "45.5-tesla direct-current magnetic field generated with a high-temperature superconducting magnet," *Nature*, vol. 570, no. 7762, pp. 496–499, 2019.

[41] S. Yoon, J. Kim, K. Cheon, H. Lee, S. Hahn, and S.-H. Moon, "26 T 35 mm all-$GdBa_2Cu_3O_{7-x}$ multi-width no-insulation superconducting magnet," *Supercond. Sci. Technol.*, vol. 29, no. 4, p. 04LT04, 2016.

[42] Y. Suetomi, T. Yoshida, S. Takahashi, T. Takao, G. Nishijima, H. Kitaguchi, Y. Miyoshi, M. Hamada, K. Saito, R. Piao, Y. Takeda, H. Maeda, and Y. Yanagisawa, "Quench and self-protecting behaviour of an intra-layer no-insulation (LNI) REBCO coil at 31.4 T," *Supercond. Sci. Technol.*, vol. 34, no. 6, p. 064003, 2021.

[43] P. Fazilleau, X. Chaud, F. Debray, T. Lécrevisse, and J.-B. Song, "38 mm diameter cold bore metal-as-insulation HTS insert reached 32.5 T in a background magnetic field generated by resistive magnet," *Cryogenics*, vol. 106, p. 103053, 2020.

[44] J. Liu, Q. Wang, L. Qin, B. Zhou, K. Wang, Y. Wang, L. Wang, Z. Zhang, Y. Dai, H. Liu, X. Hu, H. Wang, C. Cui, D. Wang, H. Wang, W. Sun, and L. Xiong, "World record 32.35 tesla direct-current magnetic field generated with an all-superconducting magnet," *Supercond. Sci. Technol.*, vol. 33, no. 3, p. 03LT01, 2020.

[45] D. Whyte, "Small, modular and economically attractive fusion enabled by high temperature superconductors," *Phil. Trans. R. Soc. A*, vol. 377, no. 2141, p. 20180354, 2019.

[46] E. Felcini, L. Bottura, J. Van Nugteren, G. De Rijk, G. Kirby, and B. Dutoit, "Magnetic design of a superconducting toroidal gantry for hadron therapy," *IEEE Trans. Appl. Supercond.*, vol. 30, no. 4, pp. 1–5, 2020.

[47] H. C. Jo, D. G. Kim, S. Choi, H. M. Jang, K. Sim, and S. Kim, "Prototype HTS quadrupole magnet for the in-flight fragment separator of RISP," *IEEE Trans. Appl. Supercond.*, vol. 28, no. 6, pp. 1–6, 2018.

[48] D. Park, J. Bascuñán, Y. Li, W. Lee, Y. Choi, and Y. Iwasa, "Design overview of the MIT 1.3-GHz LTS/HTS NMR magnet with a new REBCO insert," *IEEE Trans. Appl. Supercond.*, vol. 31, no. 5, pp. 1–6, 2021.

[49] T. T. Tallerico, J. J. Scheidler, D. Lee, and K. Haran, "Electromagnetic redesign of nasa's high efficiency megawatt motor," in *Proc. AIAA/IEEE Elect. Aircr. Technol. Symp. (EATS)*, 2020, pp. 1–15.

[50] J. Choi, T. Kim, C.-K. Lee, D.-S. Jeon, G.-W. Park, S. Cho, M. Park, I.-K. Yu, and M. Iwakuma, "Commercial design and operating characteristics of a 300 kW superconducting induction heater (SIH) based on HTS magnets," *IEEE Trans. Appl. Supercond.*, vol. 29, no. 5, pp. 1–5, 2019.

[51] J. Kim, Y. Kim, S. Yoon, K. Shin, J. Lee, J. S. Jung, J. T. Lee, J.-G. Kim, D. Kim, J. Yoo, H. Lee, S.-H. Moon, and S. Hahn, "Design, construction, and operation of an 18 T 70 mm no-insulation (RE)$Ba_2Cu_3O_{7-x}$ magnet for an axion haloscope experiment," *Rev. Sci. Instrum.*, vol. 91, no. 2, p. 023314, 2020.

[52] Y.-G. Kim, S. Hahn, K. L. Kim, O. J. Kwon, and H. Lee, "Investigation of HTS racetrack coil without turn-to-turn insulation for superconducting rotating ma-

chines," *IEEE Trans. Appl. Supercond.*, vol. 22, no. 3, pp. 5 200 604–5 200 604, 2011.

[53] J.-B. Song, S. Hahn, Y. Kim, D. Miyagi, J. Voccio, J. Bascuñán, H. Lee, and Y. Iwasa, "Dynamic response of no-insulation and partial-insulation coils for HTS wind power generator," *IEEE Trans. Appl. Supercond.*, vol. 25, no. 3, pp. 1–5, 2014.

[54] K. Kim, B.-S. Go, M. Park, and I.-K. Yu, "Design and performance analysis of a NI-type HTS field magnet for superconducting rotating machines," *IEEE Trans. Appl. Supercond.*, vol. 25, no. 3, pp. 1–4, 2015.

[55] F. Dong, Z. Huang, D. Qiu, L. Hao, W. Wu, and Z. Jin, "Design and analysis of a small-scale linear propulsion system for Maglev applications (2)–The HTS no-insulation magnets," *IEEE Trans. Appl. Supercond.*, vol. 29, no. 2, pp. 1–5, 2019.

[56] A. C. Rose-Innes and E. Rhoderick, *Introduction to superconductivity*. American Association of Physics Teachers, 1970.

[57] J. Van Nugteren, "High temperature superconductor accelerator magnets," Ph.D. dissertation, Univ. Twente, Enschede, 2016.

[58] Wikipedia, "BCS theory," 2022. [Online]. Available: https://en.wikipedia.org/wiki/BCS_theory.

[59] National High Magnetic Field Laboratory, "Low-Temperature Superconductors," 2014. [Online]. Available: https://nationalmaglab.org/magnet-development/applied-superconductivity-center/research-areas/low-temperature-superconductivity.

[60] US Geological Survey, "Helium Statistics and Information," 2022. [Online]. Available: https://www.usgs.gov/centers/national-minerals-information-center/helium-statistics-and-information.

[61] Wikipedia, "High-temperature superconductivity," 2022. [Online]. Available: https://en.wikipedia.org/wiki/High-temperature_superconductivity.

[62] SuNAM, "SuNAM's 2G HTS Wire Architecture," 2022. [Online]. Available: http://www.i-sunam.com/wp/sunam1-2/.

[63] M. Tinkham, *Introduction to superconductivity*. Courier Corporation, 2004.

[64] Wimbush, S and Strickland, N, "Critical current characterisation of SuNAM SAN04200 2G HTS superconducting wire," 2017. [Online]. Available: https://doi.org/10.6084/m9.figshare.5182354.v1.

[65] C. Barth, G. Mondonico, and C. Senatore, "Electro-mechanical properties of REBCO coated conductors from various industrial manufacturers at 77 K, self-field and 4.2 K, 19 T," *Supercond. Sci. Technol.*, vol. 28, no. 4, p. 045011, 2015.

[66] J. J. Scheidler and T. F. Tallerico, "Design, Fabrication, and Critical Current Testing of No-Insulation Superconducting Rotor Coils for NASA's 1.4 MW High-Efficiency Megawatt Motor," in *Proc. AIAA/IEEE Elect. Aircr. Technol. Symp. (EATS)*, 2018, pp. 1–9.

[67] U. Bong, S. An, J. Park, and S. Hahn, "Numerical studies on mechanical behavior of dry-wound HTS racetrack coil," *IEEE Trans. Appl. Supercond.*, vol. 30, no. 4, pp. 1–5, 2020.

[68] K. Ishida, T. Itaya, A. Tanaka, N. Takehira, and T. Miki, "Self-inductance of a racetrack coil," *IEEE Trans. Appl. Supercond.*, vol. 22, no. 4, pp. 4 905 509–4 905 509, 2012.

[69] Z. Zhao, K. Liu, C. Wang, W. Zhang, J. Li, L. Han, X. Song, and G. Ma, "The establishment of an analytical model for coreless HTS linear synchronous motor with a generalized racetrack coil as the secondary," *IEEE Trans. Appl. Supercond.*, vol. 29, no. 5, pp. 1–5, 2019.

[70] D. K. Cheng, *Field and wave electromagnetics*. Pearson Education India, 1989.

[71] P. W. Anderson and Y. Kim, "Hard superconductivity: theory of the motion of Abrikosov flux lines," *Rev. Mod. Phys.*, vol. 36, no. 1, p. 39, 1964.

[72] D. Hilton, A. Gavrilin, and U. Trociewitz, "Practical fit functions for transport critical current versus field magnitude and angle data from (RE)BCO coated conductors at fixed low temperatures and in high magnetic fields," *Supercond. Sci. Technol.*, vol. 28, no. 7, p. 074002, 2015.

[73] MathWorks, "Curve Fitting Toolbox User's Guide," 2020. [Online]. Available: https://mathworks.com/help/pdf_doc/curvefit/index.html.

[74] M. N. Wilson, *Superconducting magnets*. Clarendon Press Oxford, 1983.

[75] J. B. Song and S. Hahn, "'Leak Current'correction for critical current measurement of no-insulation HTS coil," *Progr. Supercond. Cryogenics*, vol. 19, no. 2, pp. 48–52, 2017.

[76] K. R. Bhattarai, K. Kim, K. Kim, K. Radcliff, X. Hu, C. Im, T. Painter, I. Dixon, D. Larbalestier, S. Lee, and S. Hahn, "Understanding quench in no-insulation (NI) REBCO magnets through experiments and simulations," *Supercond. Sci. Technol.*, vol. 33, no. 3, p. 035002, 2020.

[77] W. D. Markiewicz, J. J. Jaroszynski, D. V. Abraimov, R. E. Joyner, and A. Khan, "Quench analysis of pancake wound REBCO coils with low resistance between turns," *Supercond. Sci. Technol.*, vol. 29, no. 2, p. 025001, 2015.

[78] T. Wang, S. Noguchi, X. Wang, I. Arakawa, K. Minami, K. Monma, A. Ishiyama, S. Hahn, and Y. Iwasa, "Analyses of transient behaviors of no-insulation REBCO pancake coils during sudden discharging and overcurrent," *IEEE Trans. Appl. Supercond.*, vol. 25, no. 3, pp. 1–9, 2015.

[79] K. Bouloukakis, M. Hunter, N. Long, R. Dykstra, and B. Parkinson, "Discharge behaviour and modelling of a 1.5 T REBCO magnet with quench tolerant coils impregnated with conductive epoxy," *IEEE Trans. Appl. Supercond.*, vol. 31, no. 5, pp. 1–5, 2021.

[80] T. Lécrevisse, X. Chaud, P. Fazilleau, C. Genot, and J.-B. Song, "Metal-as-Insulation HTS coils," *Supercond. Sci. Technol.*, vol. 35, no. 7, p. 074004, 2022.

[81] M. Bonura, C. Barth, A. Joudrier, J. F. Troitino, A. Fete, and C. Senatore, "Systematic study of the contact resistance between REBCO tapes: Pressure dependence in the case of no-insulation, metal co-winding and metal-insulation," *IEEE Trans. Appl. Supercond.*, vol. 29, no. 5, pp. 1–5, 2019.

[82] U. Bong, J. Kim, K. Choi, J. Bang, J. T. Lee, S. An, C. Im, J. Park, S. H. Park, H. Koo, W. Kang, E. Kim, and S. Hahn, "Design, Construction, and Operation of 1 T 230 mm (RE)$Ba_2Cu_3O_{7-x}$ Magnet with Defect-Irrelevant Winding," *Applied Superconductivity Conference 2020*, Virtual Conference, Oct. 24–Nov. 7, 2020.

[83] Y. Iwasa, *Case studies in superconducting magnets: design and operational issues*. Springer Science & Business Media, 2009.

[84] J. Ma, J. Geng, W. K. Chan, J. Schwartz, and T. Coombs, "A temperature-dependent multilayer model for direct current carrying HTS coated-conductors under perpendicular AC magnetic fields," *Supercond. Sci. Technol.*, vol. 33, no. 4, p. 045007, 2020.

[85] K. Tsuchiya, A. Kikuchi, A. Terashima, K. Norimoto, M. Uchida, M. Tawada, M. Masuzawa, N. Ohuchi, X. Wang, T. Takao, and S. Fujita, "Critical current measurement of commercial REBCO conductors at 4.2 K," *Cryogenics*, vol. 85, pp. 1–7, 2017.

[86] M. Breschi, E. Berrospe-Juarez, P. Dolgosheev, A. González-Parada, P. L. Ribani, and F. Trillaud, "Impact of Twisting on Critical Current and n-value of BSCCO and (Re)BCO Tapes for DC Power Cables," *IEEE Trans. Appl. Supercond.*, vol. 27, no. 4, pp. 1–4, 2017.

[87] S.-K. Sul, *Control of electric machine drive systems*. John Wiley & Sons, 2011.

[88] J. Yoon, U. Bong, J. T. Lee, S.-W. Jung, and S. Hahn, "Investigation on Time-Varying Behavior of NI HTS Field Coil for Synchronous Motors Considering Armature Reaction and Slotting Effect," *IEEE Trans. Appl. Supercond.*, vol. 32, no. 6, p. 5201505, 2022.

[89] H. Miyazaki, S. Iwai, T. Tosaka, K. Tasaki, and Y. Ishii, "Delamination strengths of different types of REBCO-coated conductors and method for reducing radial thermal stresses of impregnated REBCO pancake coils," *IEEE Trans. Appl. Supercond.*, vol. 25, no. 3, pp. 1–5, 2015.

[90] MiSUMi, "Appropriate tightening axial force and tightening torque of bolts," 2022. [Online]. Available: https://kr.misumi-ec.com/tech-info/categories/technical_data/td01/a0198.html#notes.

[91] COMSOL, *Structural Mechanics Module User's Guide ver. 5.4*.

[92] Y. Wang, H. Song, W. Yuan, Z. Jin, and Z. Hong, "Ramping turn-to-turn loss and magnetization loss of a No-Insulation (RE)$Ba_2Cu_3O_x$ high temperature superconductor pancake coil," *J. Appl. Phys.*, vol. 121, no. 11, p. 113903, 2017.

[93] B. Shen, F. Grilli, and T. Coombs, "Overview of H-formulation: A versatile tool for modeling electromagnetics in high-temperature superconductor applications," *IEEE Access*, vol. 8, pp. 100 403–100 414, 2020.

[94] Y. Yan, T. Qu, and F. Grilli, "Numerical modeling of AC loss in HTS coated conductors and Roebel cable using TA formulation and comparison with H formulation," *IEEE Access*, vol. 9, pp. 49 649–49 659, 2021.

[95] B. R. Munson, T. H. Okiishi, W. W. Huebsch, and A. P. Rothmayer, *Fluid mechanics*. Wiley Singapore, 2013.

[96] L. Tomkow, I. Harca, K. Machaj, A. Smara, T. Reis, and B. Glowacki, "Experimental system for testing a superconducting motor at temperatures close to 15 K," *Cryogenics*, vol. 112, p. 103206, 2020.

[97] J. Lee, S. Park, Y. Kim, S. Lee, H. Joo, W. Kim, K. Choi, and S. Hahn, "Test results of a 5 kW fully superconducting homopolar motor," *Progr. Supercond. Cryogenics*, vol. 15, no. 1, pp. 35–39, 2013.

[98] B. B. Choi, K. Hunker, J. W. Hartwig, and G. Brown, "Static Measurements on HTS Coils of Fully Superconducting AC Electric Machines for Aircraft Electric Propulsion System," in *53rd AIAA/SAE/ASEE Jt. Propuls. Conf.*, 2017, p. 4956.

[99] A. Musso, G. Angeli, M. Ascade, M. Bocchi, P. L. Ribani, V. Rossi, A. Valzasina, and M. Breschi, "Electro-thermal behavior of layer-wound BSCCO coils with and without insulation," *IEEE Trans. Appl. Supercond.*, vol. 32, no. 6, p. 4604905, 2022.

[100] Tokamak Energy, "HTS progress announcement - 20 T magnet," 2021. [Online]. Available: https://www.youtube.com/watch?v=43Tl39CYhNM.

[101] V. M. Bathula, U. Choudhury, and V. Rao, "Development and testing of a 1 G based high temperature superconducting (HTS) double pancake coil for HTS synchronous machines," *Physica C*, vol. 562, pp. 36–41, 2019.

[102] *KS System of Limits and Fits*, KS B 0401:2014, 2019.

[103] J. Lu, R. Goddard, K. Han, and S. Hahn, "Contact resistance between two RE-BCO tapes under load and load cycles," *Supercond. Sci. Technol.*, vol. 30, no. 4, p. 045005, 2017.

[104] S. Lakshmikanth, "Noise and vibration reduction in PMSM-A review," *Int. J. Electr. Comput. Eng. Syst.*, vol. 2, no. 3, p. 405, 2012.

[105] P. Vijayraghavan and R. Krishnan, "Noise in electric machines: A review," *IEEE Trans. Ind. Appl.*, vol. 35, no. 5, pp. 1007–1013, 1999.

[106] N. Remus, M. S. Toulabi, S. Mukundan, H. Dhulipati, W. Li, C. Novak, and N. C. Kar, "Electromagnetic noise and vibration in PMSM and their sources: an overview," in *IEEE Can. Conf. Electr. Comput. Eng. (CCECE)*, 2020, pp. 1–4.

[107] J.-C. Park, S.-H. Park, J.-H. Kim, S.-G. Lee, G.-H. Lee, and M.-S. Lim, "Diagnosis and robust design optimization of SPMSM considering back EMF and cogging torque due to static eccentricity," *Energies*, vol. 14, no. 10, p. 2900, 2021.

[108] M.-H. Sohn, K. Sim, B. Eom, H.-S. Ha, H.-Y. Kim, and K. Seong, "Controllability of the contact resistance of 2G HTS coil with metal insulation," *IEEE Trans. Appl. Supercond.*, vol. 28, no. 3, pp. 1–5, 2018.

[109] Y. Choi, S. Hahn, J. Song, D. Yang, and H. Lee, "Partial insulation of GdBCO single pancake coils for protection-free HTS power applications," *Supercond. Sci. Technol.*, vol. 24, no. 12, p. 125013, 2011.

[110] J. Mun, C. Lee, K. Sim, C. Lee, M. Park, and S. Kim, "Electrical characteristics of soldered metal insulation REBCO coil," *IEEE Trans. Appl. Supercond.*, vol. 30, no. 4, pp. 1–4, 2020.

[111] J. Ma, J. Geng, and T. Coombs, "Flux pumping for non-insulated and metal-insulated HTS coils," *Supercond. Sci. Technol.*, vol. 31, no. 1, p. 015018, 2017.

[112] J. Lu, Y. Xin, E. Lochner, K. Radcliff, and J. Levitan, "Contact resistivity due to oxide layers between two REBCO tapes," *Supercond. Sci. Technol.*, vol. 33, no. 4, p. 045001, 2020.

[113] J.-B. Song, X. Chaud, F. Debray, S. Krämer, P. Fazilleau, and T. Lécrevisse, "Metal-as-Insulation HTS Insert for Very-High-Field Magnet: A Test Report After Repair," *IEEE Trans. Appl. Supercond.*, vol. 32, no. 6, pp. 1–6, 2022.

[114] *IEEE Guide for Test Procedures for Synchronous Machines Including Acceptance and Performance Testing and Parameter Determination for Dynamic Analysis*, IEEE Standard 115–2019, 2019.

[115] S. S. Kalsi, *Applications of high temperature superconductors to electric power equipment*. John Wiley & Sons, 2011.

[116] M. Takayasu, "Width-bending characteristic of REBCO HTS tape and flat-tape Rutherford-type cabling," *Supercond. Sci. Technol.*, vol. 34, no. 12, p. 125020, 2021.

[117] J. Xia, H. Bai, H. Yong, H. W. Weijers, T. A. Painter, and M. D. Bird, "Stress and strain analysis of a REBCO high field coil based on the distribution of shielding current," *Supercond. Sci. Technol.*, vol. 32, no. 9, p. 095005, 2019.

[118] National Institute of Standards and Technology (NIST), "Properties of solid materials from cryogenic- to room-temperatures," 2022. [Online]. Available: https://trc.nist.gov/cryogenics/materials/materialproperties.htm.

[119] R. J. Deissler, T. Baig, C. Poole, A. Amin, D. Doll, M. Tomsic, and M. Martens, "A Computational Study to Find an Optimal RRR Value for a 1.5-T Persistent-Mode Conduction-Cooled MgB_2 MRI Magnet From a Quench Protection Point of View," *IEEE Trans. Appl. Supercond.*, vol. 27, no. 4, pp. 1–6, 2017.

[120] M. Cho, S. Noguchi, J. Bang, J. Kim, U. Bong, J. T. Lee, S. B. An, K. R. Bhattarai, K. Kim, K. Kim, C. Im, K. J. Han, and S. Hahn, "Combined circuit model to simulate post-quench behaviors of no-insulation HTS coil," *IEEE Trans. Appl. Supercond.*, vol. 29, no. 5, pp. 1–5, 2019.

[121] C. Im, S. An, J. Bang, J. Kim, K. R. Bhattarai, K. L. Kim, K. Kim, and S. Hahn, "An inverse calculation study on post-quench behavior of a no-insulation REBCO insert," *IEEE Trans. Appl. Supercond.*, vol. 30, no. 4, pp. 1–5, 2020.

[122] J.-B. Song, S. Hahn, T. Lécrevisse, J. Voccio, J. Bascuñán, and Y. Iwasa, "Over-current quench test and self-protecting behavior of a 7 T/78 mm multi-width no-insulation REBCO magnet at 4.2 K," *Supercond. Sci. Technol.*, vol. 28, no. 11, p. 114001, 2015.

[123] K. R. Bhattarai, K. Kim, S. Kim, S. Lee, and S. Hahn, "Quench analysis of a multiwidth no-insulation 7-T 78-mm REBCO magnet," *IEEE Trans. Appl. Supercond.*, vol. 27, no. 4, pp. 1–5, 2017.

초 록

최근 지구온난화가 가속화됨에 따라 세계 각국에서는 탄소중립을 달성하기 위하여 온실가스 배출을 줄이기 위한 기술 연구를 활발하게 수행하고 있다. 온실가스 저감을 위한 노력은 전력시스템, 수송, 제조 산업, 생활 건물 등 사회 전 분야에서 이뤄지고 있다. 이중 특히 대형 화물 트럭, 선박 및 항공기를 포함하는 수송 분야에서는 온실가스 배출을 획기적으로 절감하기 위하여 기존 화석연료 기반 추진 시스템을 대체할 수 있는 수소 혹은 전기 에너지 기반의 새로운 고성능 추진 시스템의 개발이 요구되고 있다. 대체 연료에 기반한 추진 시스템 개발 시 중요하게 여겨지는 부분 중 하나는 경량화 및 소형화를 위한 추진 시스템의 출력 및 에너지 밀도의 향상이다. 고온초전도 모터를 기반으로 하는 전기추진 시스템은 고온초전도 코일의 높은 통전 전류를 기반으로 기존 상전도 기반 시스템을 뛰어넘는 높은 출력밀도를 달성할 수 있을 것으로 예상된다. 이에 따라 전기추진 항공기 등 차세대 수송 시스템에 적용하기 위한 고온초전도 전기추진 시스템 개발 프로젝트가 미국, 일본, 유럽을 포함한 선진국들을 중심으로 착수되어 진행되고 있다.

기존 고온초전도 모터의 기술적 난제 중 하나로써 고온초전도 계자 권선의 운전 안정성과 보호의 어려움이 지속적으로 논의되어 왔다. 이를 개선하기 위하여 무절연 고온초전도 권선 기술을 적용한 무절연 고온초전도 모터 개념이 제안되었다. 무절연 고온초전도 권선 기술은 초전도 턴간의 절연을 제거함으로써 고온초전도 코일의 운전 신뢰성을 크게 향상 시킨 기술로써, 퀜치 사고 시 코일의 보호에 매우 효과적임이 실험적으로 여러 차례 검증된 바 있다. 하지만, 턴간의 절연 제거로 인하여 무절연 고온초전도 계자 권선의 누설 전류가 발생에 따라 일반적인 절연된 계자 권선과 다소 다른 운전 특성을 보일 수 있으며, 이러한 무절연 특성에서 비롯된 운전 특성으로

인하여 무절연 계자 권선이 실제 모터에 적용 가능한 기술인지에 대한 논의가 필요하다. 이를 위해서, 무절연 계자 권선을 모터에 적용할 시 운전 특성을 해석하기 위한 모델의 수립과 실험을 통한 특성 분석 연구가 요구된다.

본 연구에서는, 무절연 고온초전도 계자 권선의 초전도 모터에의 적용 가능성에 대하여 논의하였다. 이를 위하여 기존에 제시된 절연 초전도 코일과 무절연 초전도 코일의 해석 기법들을 바탕으로, 무절연 특성이 반영된 무절연 고온초전도 모터의 해석 모델을 최초로 제시하고 이를 바탕으로한 해석을 수행하였다. 또한, 실제 실험을 통한 특성 분석을 위하여 무절연 계자 권선을 적용한 특성 시험 장치의 설계 및 제작을 수행하였다. 액체질소 기반 냉각 시스템과 초전도 모터 시험을 위한 다이나모 실험 장치를 구축하였으며, 설계 시 고려되어야 하는 주요 전기적, 구조적, 열적 특성을 분석하여 이를 설계에 반영하였다. 구축한 시험장치를 이용하여 무절연 계자 권선이 적용된 시험용 모터를 다양한 조건에서 운전을 수행하였고, 이 때 나타나는 무절연 고온초전도 계자 권선의 응답 특성을 최초로 관측하고 정리하였다. 무절연 고온초전도 계자 권선에서 나타나는 응답 특성의 원인을 시험 시스템의 조건을 고려하여 제안한 해석모델을 통해 분석하였고, 이러한 무절연 고온초전도 계자 권선의 응답이 모터의 운전 특성에 어떠한 영향을 미칠 수 있는지 논의하였다. 마지막으로, 실제 모터에 무절연 고온초전도 계자권선을 적용하기 위한 개선점들과 추가적인 연구의 필요성에 대하여 정리하였다.

주요어: 고온초전도, 무절연 권선법, 운전특성, 전기추진, 초전도 모터
학번: 2017-27856